Grant Agreement No: 101096307

Full Title: THz Industrial Mesh Networks in Smart Sensing and Propagation Environments

Start date: 01/01/2023

End date: 31/12/2025

Duration: 36 Months

Deliverable D4.1

Intermediate report on PHY layer enhancements for THz links supporting sensing and communication functionalities

Document Type	Deliverable
Title	D4.1 - Intermediate report on PHY layer enhancements for THz links supporting sensing and communication functionalities
Contractual due date	31/12/2023
Actual submission date	30/12/2023
Nature	Report
Dissemination Level	PUB
Lead Beneficiary	HWDU
Responsible Author	Tommaso Zugno (HWDU)
Contributions from	Luca Antonelli, Luca Sanguinetti, Antonio D'Amico, Tommaso Bacchielli, Andrea Giorgetti, Mattia Fabiani, Davide Dardari, Danila Ferretti (CNIT), Lutfi Samara, Walid Ghanem, Tommaso Zugno, Mario Castañeda (HWDU), Simon Haussmann, Dominik Wrana (US-TUTT), Steffen Pahlke (TUBS)

6GSNS

Revision history

Version	Issue Date	Changes	Contributor(s)
v0.1	02/11/2023	Initial Version	Luca Antonelli, Luca Sanguinetti, Antonio D'Amico, Tommaso Bacchielli, Andrea Giorgetti (CNIT), Lutfi Samara, Walid Ghanem, Tommaso Zugno (HWDU), Simon Haussmann, Dominik Wrana (USTUTT)
v0.2	23/11/2023	Revision	Luca Antonelli, Luca Sanguinetti, Antonio D'Amico, Tommaso Bacchielli, Andrea Giorgetti, Mattia Fabiani (CNIT), Lutfi Samara, Walid Ghanem, Tommaso Zugno, Mario Castañeda (HWDU), Simon Haussmann, Dominik Wrana (USTUTT), Steffen Pahlke (TUBS)
v0.3	07/12/2023	Revision	Luca Antonelli, Luca Sanguinetti, Antonio D'Amico, Tommaso Bacchielli, Andrea Giorgetti, Mattia Fabiani (CNIT), Lutfi Samara, Walid Ghanem, Tommaso Zugno, Mario Castañeda (HWDU), Simon Haussmann, Dominik Wrana (USTUTT), Steffen Pahlke (TUBS)
v0.4	12/12/2023	Add introduction and conclusion. Candidate deliverable version.	Tommaso Zugno (HWDU)
v0.5	18/12/2023	Review comments, fixed formatting issues.	Per Hjalmar Lehne (TNOR), Dominik Wrana (USTUTT), Danila Ferretti (CNIT)
v0.6	20/12/2023	Addressed review comments. Final version.	Tommaso Zugno (HWDU), Luca Antonelli, Mattia Fabiani (CNIT)
v1.0	30/12/2023	Approved.	Danila Ferretti, Luca Sanguinetti (CNIT)

Disclaimer

their officers, employees or agents shall be responsible or liable in negligence or otherwise howsoever in respect of any inaccuracy or omission herein. Without derogating from the generality of the foregoing neither the TIMES Consortium nor any of its members, their officers, employees or agents shall be liable for any direct or indirect or consequential loss or damage caused by or arising from any information, advice, inaccuracy, or omission herein.

Copyright Message

Table of Contents

List of Abbreviations

3GPP 3rd Generation Partnership Project

ADC Analog-to-digital Converter

ADR Aggregate Data Rate

AM-AM Amplitude-to-Amplitude

AM-PM Amplitude-to-Phase

AoA Angle of Arrival

AoD Angle of Departure

AWGN Additive White Gaussian Noise

BBU Base Band Unit

BER Bit Error Rate

BS Base Station

CC Component Carrier

CCB Component Carrier Bandwidth

CDF Cumulative Distribution Function

CCDR Component Carrier Data Rate

CFR Channel Frequency Response

CFO Carrier Frequency Offset

CIR Channel Impulse Response

CMOS Complementary Metal-Oxide Semiconductor

CP Cyclic Prefix

CSI Channel State Information

CDF Cumulative Distribution Function

DFT Discrete Fourier Transform

DAC Digital-to-analog Converter

DC Direct Current

DRO Dielectric Resonator Oscillator

ELAA Electrically Large Aperture Array

EVM Error Vector Magnitude

FDD Frequency Division Duplex

FFT Fast Fourier Transform

FOV Field of View

ICI Inter-carrier Interference

IF Intermediate Frequency

IFFT Inverse-Fast Fourier Transform

ISAC Integrated Sensing and Communication

ISI Inter-Symbol Interference

i.i.d. independent and identically distributed

KPI Key Performance Indicators

LO Local Oscillator

LoS Line of Sight

LNA Low Noise Amplifier

MIMO Multiple-Input-Multiple-Output

MMSE Minimum Mean Square Error

mmWave millimeter-Wave

MR Maximum Ratio

NSE No Synchronization Error

OFDM Orthogonal Frequency Division Multiplexing

PLL Phase Locked Loop

PN Phase Noise

PAPR Peak-to-Average Power Ratio

PA Power Amplifier

PDF Probability Density Function

PHY physical

PoC Proof-of-Concept

PS Phase Shifter

QAM Quadrature Amplitude Modulation

RCS Radar Cross Section

RF Radio Frequency

RIS Reconfigurable Intelligent Surface

RMSE Root-Mean-Square Error

RX Receiver

SE Spectral Efficiency

SNR Signal-to-Noise-Ratio

SINR Signal-to-Interference-plus-Noise Ratio

SNR Signal-to-Noise-Ratio

SSPA Solid State Power Amplifier

TDD Time Division Duplex

TSE Time Synchronization Error

TTD True Time Delay

THz Terahertz

TX Transmitter

UE User Equipment

WP Work Package

Executive Summary

The TIMES project aims at building a smart radio ecosystem operating in complex environments and offering similar performance as wired networks. The project will adopt Terahertz (THz) communications as the main technological driver to turn this vision into reality. In particular, it will exploit the large amount of radio resources available in THz bands and the sensing-friendly characteristics of THz signals to enable extremely-high data rates (in the order of terabits per second) , ultra-low latency, accurate sensing capabilities, and high reliability. However, the design of such a system opens up several challenges. For example, the harsh and uncommon propagation conditions experienced at such high frequencies call for a paradigm shift in the design of the physical (PHY) layer. The integration of sensing and communication functionalities within the same wireless interface calls for revisiting traditional solutions taking into account the requirements in both domains. Also, proper mitigation schemes are essential to overcome the pronounced impairments faced by THz transceivers.

In this regard, the TIMES project is working towards the definition of THz-based air interface with communication and sensing capabilities. This deliverable summarizes the results that have been achieved in the first phase of the project. In particular, it presents intermediate findings on physical layer procedures for enabling highly efficient and reliable THz links supporting sensing and communication functionalities, and discusses estimation mechanisms to predict the evolution of THz channels. It is deemed appropriate to note that the results reported in this document are preliminary, as the related activities are still ongoing. Final results will be presented in a subsequent report, providing more detailed design guidelines for realizing a THz-based air interface and a thorough analysis of sensing and communication functionalities in the scenarios targeted by the project.

1 Introduction

The long-term vision of the TIMES project is to build a THz-based smart radio ecosystem working in complex scenarios with a large number of heterogeneous devices capable of offering similar performance as wired networks in terms of data rate (up to Tbps), ultra-low-latency, sensing, and reliability, thus beyond the capability of current wireless networks. To achieve this goal, the project will exploit the ultra-wide bandwidth and sensing-friendly characteristics of THz communications, deploy intelligent mesh networks in smart propagation environments, and enable high-definition Integrated Sensing and Communication (ISAC). This opens up significant technological challenges that must be overcome to turn this ambitious vision into reality.

On the one hand, operating at THz frequencies offers the opportunity to exploit a vast amount of unused radio resources and achieve extremely high data rates. On the other hand, the harsh and uncommon propagation conditions experienced at such high frequencies require a paradigm shift in the design of the wireless interface. As we go up in frequency, near-field propagation phenomena becomes predominant in the entire communication range and can be leveraged to substantially improve the spatial multiplexing gain. This feature makes THz communication systems inherently different compared to the previous generations, thus calling for a novel PHY layer design.

In addition, the integration of sensing and communication functionalities within the same wireless system requires to revisit traditional solutions taking into account the requirements in both domains. The design of a waveform able to operate at THz frequencies and deliver high communication and sensing performance at the same time is a crucial aspect that is still unsolved. In presence of mobility, smart tracking algorithms are necessary to properly follow moving targets over time given the high directionality that characterizes THz links.

Finally, undesired effects arising from imperfection in the Radio Frequency (RF) components can have a negative impact on both communication and sensing performance. Their effect is particularly pronounced when targeting THz bands, therefore their characterization and mitigation is of paramount important to ensure seamless operations.

Within the context of this project, Work Package (WP) 4 is working on the design of a THz-based air interface with communication and sensing capabilities. As part of this WP, a first task is developing PHY layer enhancements that are necessary to cope with the untypical propagation properties of THz signals in complex environments and, at the same time, exploit the large amount of radio resources that are available in this portion of the spectrum. Moreover, it is assessing that impact of the pronounced hardware impairments that arise when operating at such high frequencies and devising efficient mitigation schemes. A second task focusing on the design of an air interface able to support ISAC functionalities. In this regard, new waveforms able to deliver high communication and sensing performance are being studied. Also, novel algorithms able to track sensing targets that are moving over time are being developed.

This deliverable summarizes the results that have been achieved since the beginning of this WP, i.e., between April and December 2023. In particular, it presents intermediate findings on PHY layer procedures for enabling highly efficient and reliable THz links supporting sensing and communication functionalities, and discusses estimation mechanisms to predict the evolution of THz channels. It is deemed appropriate to point out that the results reported in this document are preliminary as the aforementioned activities are still ongoing. The final outcomes will be presented in a subsequent report and will provide more detailed design guidelines for the realization of a THz-based air interface and a thorough analysis of ISAC functionalities in the scenarios targeted by the project.

1.1 Scope

This deliverable presents intermediate findings on physical layer procedures for enabling highly efficient and reliable THz links supporting sensing and communication functionalities, and discusses estimation mechanisms to predict the evolution of THz channels.

1.2 Audience

This report is intended for public use.

1.3 Structure

The rest of the document is structured as follows:

- Section 2 explores the potential and challenges of Line of Sight (LoS) Multiple-Input-Multiple-Output (MIMO) techniques applied to THz communication systems. It shows that the adoption of antenna arrays plays a pivotal role to enable high beamforming and multiplexing gains, and demonstrates how near-field propagation phenomena can be leveraged increase the spatial diversity by adopting proper processing techniques at the physical layer. Moreover, it studies the impact of the adopted beamforming architecture on the achievable communication performance and investigates problem of acquiring timely and accurate channel state information when operating with highly-dynamic channels and large bandwidths.
- Section 3 lays the foundation for an efficient THz air interface capable of ISAC. It studies novel designs for the PHY layer waveform able to achieve high communication performance and accurate sensing capabilities, while complying with the constraints in the RF components. Furthermore, it presents a novel approach that exploits THz ISAC functionalities for the tracking of moving targets.
- Section 4 analyzes the limitations of THz wireless transceivers caused by imperfections in the RF components. It identifies the potential impairments and quantifies their effect by means of measurements on preliminary RF hardware components. Moreover, it evaluates the impact of these impairments on the system performance and propose suitable mitigation techniques.
- Section 5 presents the conclusions.

2 Terahertz Line-of-Sight MIMO Communications

In the traditional design of a Base Station (BS), antenna panels connected to a Base Band Unit (BBU) were used to manage the digital signal processing. These panels, characterized by their tall and narrow design, contained multiple vertically stacked radiating elements. By emitting identical signals from these elements, constructive superposition was used to produce a radiation pattern that was vertically narrow and horizontally wide, covering a specified floor area, as shown in Fig. 1a.

In modern BSs, linear antenna arrays have been replaced with planar structures. The latter allows for a higher beamforming gain, resulting in narrower radiation beams in both horizontal and vertical domains. The BBU, now equipped with significantly enhanced computational capabilities, individually controls the signal transmitted by each antenna element. This allows the physical shape of the generated beam to be varied in both time and frequency. Fig. 1b illustrates this updated setup, showing how each beam is narrow enough to target a specific user. When these arrays are deployed in propagation environments with multiple widely spaced paths, each radiated signal loses its directional beam shape and is instead fine-tuned to coherently superimpose on a small region around the intended receiver. Antenna arrays bring about four main benefits:

- *Beamforming*: This term refers to the basic formation of a beam of energy from a set of phased arrays. Using phased antenna arrays it is possible to control the shape and direction of the signal beam from multiple antennas based on the antenna spacing and the phase of signal from each antenna element in the array. Accordingly, the creation of the beam using the technique of interfering and constructing patterns is called beamforming.
- *Beamsteering*: Beamsteering takes the concept of beamforming a stage further. It is the way in which a beam pattern can be dynamically altered by changing the signal phase in real time without changing the antenna elements or other hardware components.
- *Spatial diversity*: Typically, signals traverse multiple paths between the transmitter and receiver, and the resulting signal replicas can be destructively combined, resulting in signal fading. Antenna arrays can address this problem by simultaneously observing multiple fading realizations, thereby mitigating the effects of signal fading.
- *Spatial multiplexing*: It is possible to transmit multiple signals simultaneously on different beams, either to a single user with multiple antennas or to multiple users, as shown in Fig. 1b. This provides a traffic multiplier or multiplexing gain, provided that interference between the signals is effectively managed.

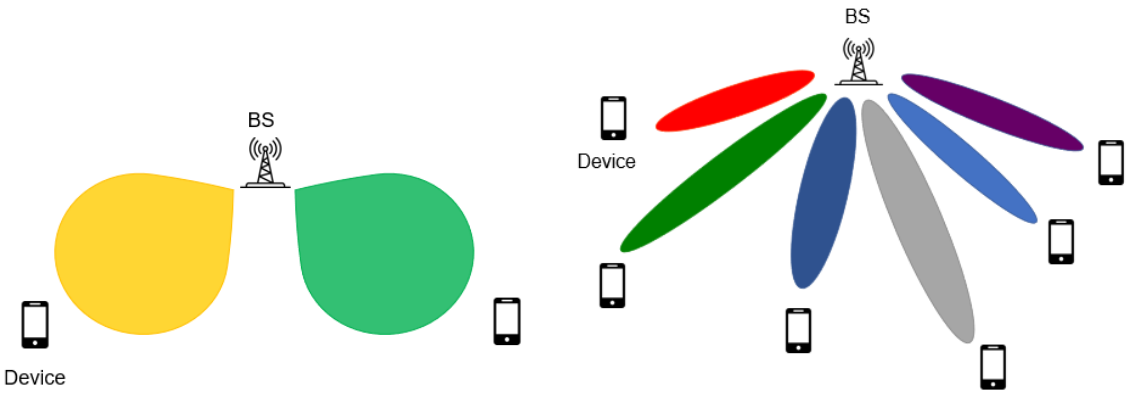

(a) Traditional BS deployment. *(b) BS with antenna arrays.*

Figure 1: (a) Traditional BS design with fixed directive antennas that broadcast each signal into a sector. (b) BS is equipped with antenna arrays that can exploit the three main multi-antenna benefits: beamforming gain, spatial diversity, and spatial multiplexing.

As the frequency increases, the transmission range necessarily shrinks and LoS propagation becomes predominant. The array signal processing literature relies on the planar wavefront approximation over the array [1]; that is, all the antenna elements receive the signal from the same angle of arrival with the same propagation path loss. This approximation becomes inadequate at high frequencies. Since the wavelength reduces dramatically and the transmission range tends to be short, the wave curvature over the array is no longer negligible [2]. When an antenna radiates a wireless signal in free space, the wavefront of the electromagnetic waves has a different shape depending on the observation distance. Traditionally, two regions have been distinguished: the Fresnel and the far-field regions. Wireless communications have almost exclusively operated in the antenna (array) far field, which is conventionally characterized by propagation distances beyond the Fraunhofer distance. However, when arrays between $20\,\text{cm}$ and $1\,\text{m}$ are utilized, the typical communication ranges up to $100\,\text{m}$ are entirely in the Fresnel region when using a carrier frequency in the THz band ($100\ \text{GHz} - 1\,\text{THz}$). Thus, the plane wave approximation does not hold anymore, and spherical wavefront propagation or some more accurate approximations such as the parabolic one [3], must be considered instead. This offers the opportunity for spatial-multiplexing. Moreover, very large bandwidths are available in the THz band, that can be exploited together with spatial multiplexing to achieve aggregate throughput up to $1\,\text{Tbit/s}$.

2.1 LoS Scenario

Consider a narrowband communication system in which the receiver is equipped with N antennas and the transmitter is a single-antenna device. We want to derive the expression of the channel coefficient between the transmitter and the receiving antennas, in a free-space propagation scenario, characterized by the absence of scatterers and obstacles. This is the so-called free-space LoS propagation scenario.

2.1.1 Far-field and Near-Field Regions of a Passive Antenna

We report the following definitions of *far-field* and *near-field* region of an antenna [4].

- The far-field region "*is that region of the field of an antenna where the angular field distribution is essentially independent of the distance from the antenna.*"
- The near-field region "*is that part of space between the antenna and the far-field region.*"

In the far-field region, the transmitting antenna behaves like a *source point* so that the radiated field can approximately be characterized by spherical wave fronts. If the antenna has a maximum dimension L_t, which is large compared to the wavelength, the far-field region is commonly taken to exist at distances greater than $2L_t^2/\lambda$ from the antenna, λ being the wavelength. In practice, L_t can be viewed as the diameter of the smallest sphere that completely contains the antenna. The quantity $2L_t^2/\lambda$ is referred to as the *Fraunhofer distance*.

2.1.2 LoS Channel Model with Antenna Arrays

The derivation of the channel model will be made on the basis of the two following assumptions.

1. Each receiving antenna of the array is located in the far field of the transmitting antenna.
2. The incident electromagnetic wave produced by the transmitting antenna and impinging on a receive antenna of the array can be approximated by a plane wave.

The plane wave approximation of Assumption 2 can be made provided that the distance between the transmit and receive antennas is greater than $d_{FA} = 2L_r^2/\lambda$, where L_r represents the maximum dimension of the *receive* antenna. It is worth observing that such a condition is equivalent to the condition that defines the far-field region of the receive antenna. Accordingly, we can say that the spherical wave front of the transmit antenna can *locally* be approximated with a planar wave front if the transmit antenna is in the far-field region of the receive antenna.

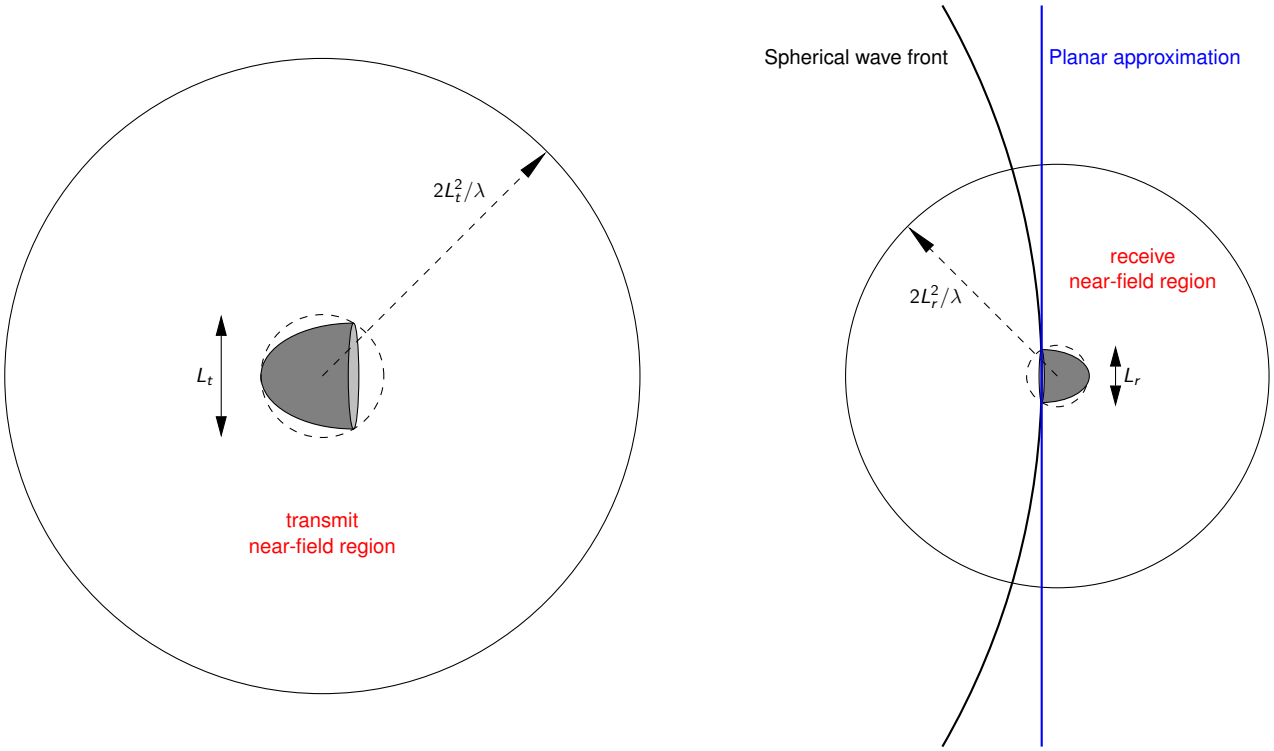

Figure 2: Meaning of Assumptions 1 and 2. Both the transmit and receive antennas are in the far-field regions of each other. The spherical wave fronts can be approximated by locally planar wave fronts.

Here, *locally* means "in the region occupied by the receive antenna". A pictorial representation of Assumptions 1 and 2 is given in Fig. 2.

Based on the above assumptions, the complex baseband channel from the transmitting antenna to the nth receiving antenna can be written as

$$h_n = \sqrt{\beta_n} e^{-j\frac{2\pi}{\lambda}d_n} \qquad n = 0, ..., N-1, \tag{1}$$

where β_n accounts for the path loss and the transmit/receive antenna gains, whereas d_n denotes the Euclidean distance between the centers of the transmitting and the n-th receiving antenna.

2.2 Alternative LoS Channel Models

When the size of the array is smaller than the transmission distance, two approximations of the channel model can be adopted. The first is the so-called parabolic model [3] while the other is the well-known planar model, commonly used in MIMO communication systems operating at sub-6 GHz.

2.2.1 Parabolic Wave Front Model

In a cartesian coordinate system $OXYZ$, let $\mathbf{s}$, $\mathbf{r}_n$ and $\mathbf{c}$ denote the position vectors of the transmit antenna, the nth receive antenna, and the center of the receive array, respectively. Accordingly, we can write $\mathbf{r}_n = \mathbf{c} + \delta_n$, where δ_n is the displacement from $\mathbf{c}$ to $\mathbf{r}_n$. Letting $\mathbf{d}_C = \mathbf{s} - \mathbf{c}$ be the displacement from $\mathbf{s}$ to $\mathbf{c}$, the distance d_n

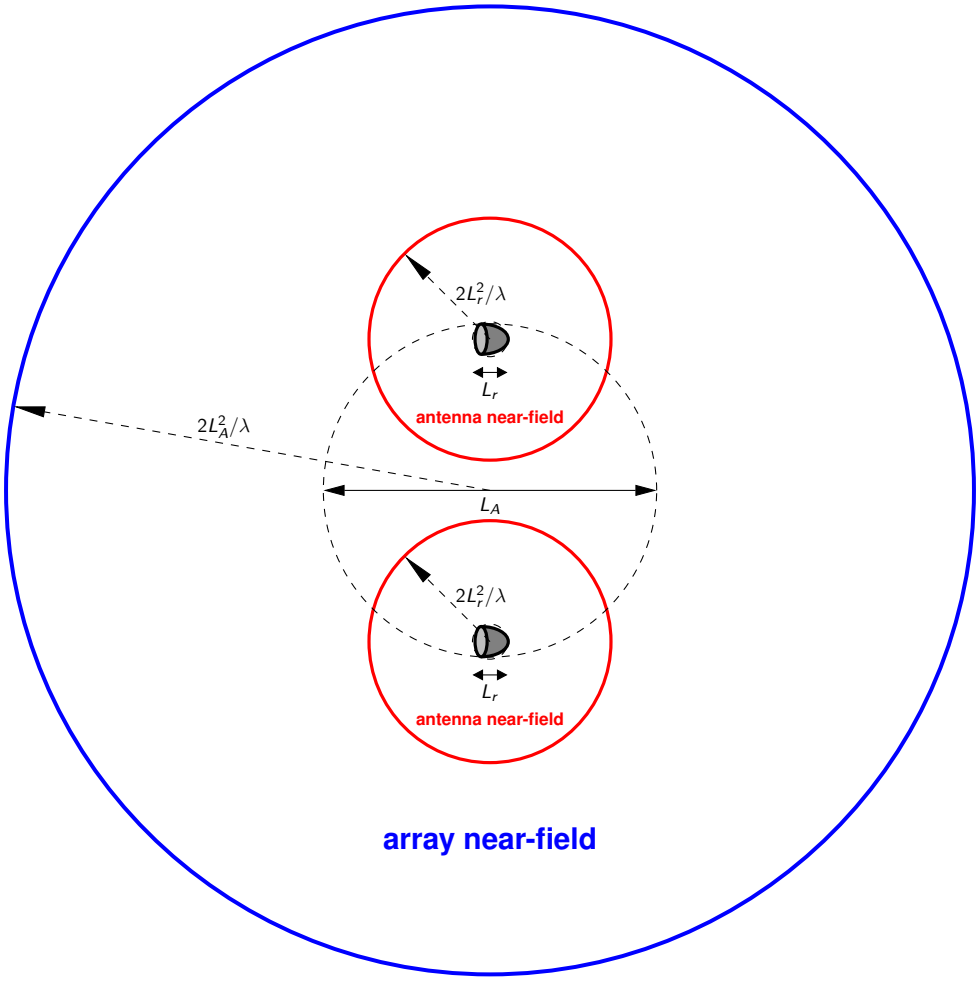

Figure 3: Antenna near-field and array near-field for an array with two antennas.

from the transmitter to the nth receive antenna is given by

$$\begin{aligned} d_n = ||\mathbf{s} - \mathbf{r}_n|| &= ||\mathbf{d}_C - \delta_n|| \\ &= \sqrt{d_C^2 + \delta_n^2 - 2(\mathbf{d}_C \cdot \delta_n)} \\ &= d_C \sqrt{1 + \frac{\delta_n^2}{d_C^2} - \frac{2(\mathbf{d}_C \cdot \delta_n)}{d_C^2}} \end{aligned} \tag{2}$$

where $d_C = ||\mathbf{d}_C||$ is the distance between the transmitter and the center of the receive array, and $\delta_n = ||\delta_n||$. Also, $\mathbf{a} \cdot \mathbf{b}$ denotes the dot (or scalar) product between the vectors $\mathbf{a}$ and $\mathbf{b}$.

Assume now that the transmitter is at a distance much larger than the array size, i.e., $d_C \gg \delta_n$. In this case, we

can use the Taylor approximation $\sqrt{1+x} \approx 1 + x/2 - x^2/8$ in (2) to write

$$\begin{aligned} d_n &\approx d_C \left\{ 1 + \frac{1}{2}\left[\frac{\delta_n^2}{d_C^2} - \frac{2(\mathbf{d}_C \cdot \boldsymbol{\delta}_n)}{d_C^2}\right] - \frac{1}{8}\left[\frac{\delta_n^2}{d_C^2} - \frac{2(\mathbf{d}_C \cdot \boldsymbol{\delta}_n)}{d_C^2}\right]^2 \right\} \\ &= d_C \left\{ 1 - \frac{\mathbf{d}_C \cdot \boldsymbol{\delta}_n}{d_C^2} + \frac{1}{2}\left[\frac{\delta_n^2}{d_C^2} - \frac{(\mathbf{d}_C \cdot \boldsymbol{\delta}_n)^2}{d_C^4}\right] + o\left(\frac{\delta_n^2}{d_C^2}\right) \right\} \\ &\approx d_C \left\{ 1 - \frac{\mathbf{d}_C \cdot \boldsymbol{\delta}_n}{d_C^2} + \frac{1}{2}\left[\frac{\delta_n^2}{d_C^2} - \frac{(\mathbf{d}_C \cdot \boldsymbol{\delta}_n)^2}{d_C^4}\right] \right\} \\ &= d_C \left\{ 1 - \frac{\delta_n \cos\alpha_n}{d_C} + \frac{1}{2}\left(\frac{\delta_n^2}{d_C^2} - \frac{\delta_n^2 \cos^2\alpha_n}{d_C^2}\right) \right\} \\ &= d_C \left\{ 1 - \frac{\delta_n \cos\alpha_n}{d_C} + \frac{1}{2}\left[\frac{\delta_n^2\left(1-\cos^2\alpha_n\right)}{d_C^2}\right] \right\} \\ &= d_C - \delta_n \left(\cos\alpha_n - \frac{\delta_n \sin^2\alpha_n}{2d_C}\right) \triangleq d_n^{(parabolic)} \end{aligned} \tag{3}$$

where $\cos\alpha_n \triangleq \dfrac{\mathbf{d}_C}{d_C} \cdot \dfrac{\boldsymbol{\delta}_n}{\delta_n}$. Plugging (3) into (1) the following parabolic model is obtained:

$$h_n^{(parabolic)} = \sqrt{\beta_n} e^{-j\frac{2\pi}{\lambda} d_n^{(parabolic)}}. \tag{4}$$

It is worth observing that the dependence of h_n on d_n is much more significant in terms of phase than amplitude. Hence, for the computation of β_n we can safely consider $d_n \approx d_C$ [3].

2.2.2 Planar Wave Front Model

The planar approximation is obtained by considering in (3) only the first order term, i.e.,

$$d_n^{(planar)} \triangleq d_C - \delta_n \cos\alpha_n \tag{5}$$

leading to the planar channel model in the form

$$h_n^{(planar)} = \sqrt{\beta_n} e^{-j\frac{2\pi}{\lambda} d_n^{(planar)}}. \tag{6}$$

2.2.3 Fraunhofer Distance of a Receiver Array

Since the second-order approximation terms at the exponent are multiplied by $2\pi/\lambda$, dropping them requires that

$$\frac{2\pi\delta_n^2}{2\lambda d_C} \ll 1$$

or, equivalently,

$$d_C \gg \frac{\pi\delta_n^2}{\lambda}.$$

Denoting by L_A the maximum dimension of the *receive array*[1], the above condition is commonly replaced by

$$d_C \gg \frac{2L_A^2}{\lambda} \triangleq d_{FA} \tag{7}$$

[1] Again, L_A can be viewed as the diameter of the smallest sphere that completely contains the array.

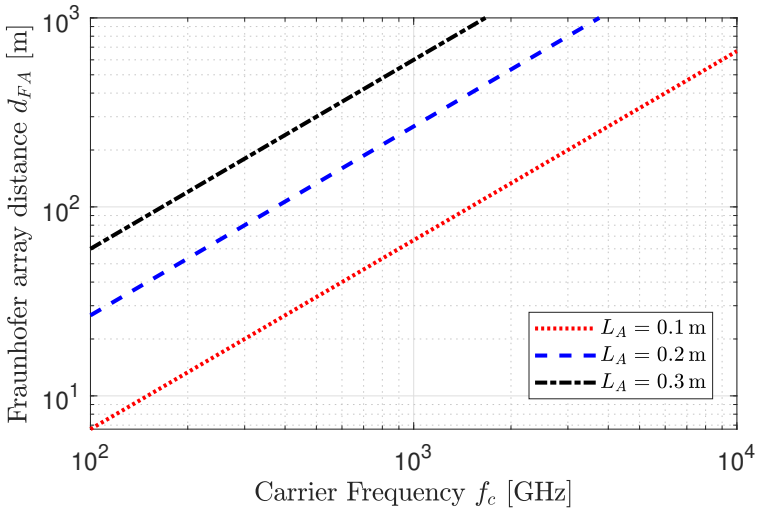

Figure 4: Fraunhofer array distance d_{FA} as a function of the carrier frequency f_c over the whole THz band.

where d_{FA} represents the Fraunhofer distance for the receive array. Accordingly, we can say that the planar approximation represents a valid channel model provided that the transmitter is in the *far-field region of the receive array*. A pictorial explanation of the near-field and far-field regions of an array with two antennas is shown in Fig. 3.

Fig. 4 shows the Fraunhofer distance as a function of the carrier frequency $f_c \triangleq c/\lambda$, where c denotes the speed of light in vacuum, for three different values of L_A. We see that with $L_A = 0.1$ m (which could correspond to a planar square array whose side is $0.1/\sqrt{2}$ m) $d_{FA} \approx 20$ m at $f_c = 300$ GHz, and increases to $d_{FA} \approx 67$ m at $f_c = 1$ THz. These values can be much larger than the typical distances in many practical scenarios.

2.3 LoS MIMO Communications

We consider the planar array shown in Fig. 5. The array consists of N_V horizontal rows and N_H antennas per row, for a total of $N = N_H N_V$ antennas. Each antenna is a squared patch antenna and has an area A. The spacing (between edges) is d_H and d_V along the horizontal and vertical directions, respectively. Thus, the horizontal and vertical lengths of the array are respectively given by

$$L_H = N_H\sqrt{A} + (N_H - 1)\, d_H \tag{8}$$

$$L_V = N_V\sqrt{A} + (N_V - 1)\, d_V. \tag{9}$$

The antennas are numbered from left to right and from the bottom row to the top row so that antenna n is located at $\mathbf{r}_n = [r_{n,x}, r_{n,y}, 0]^T$, where

$$r_{n,x} = \Delta_H \left(-\frac{N_H - 1}{2} + \mathrm{mod}\,(n-1, N_H) \right) \tag{10}$$

$$r_{n,y} = \Delta_V \left(-\frac{N_V - 1}{2} + \lfloor (n-1)/N_H \rfloor \right) \tag{11}$$

with $\Delta_H = \sqrt{A} + d_H$ and $\Delta_V = \sqrt{A} + d_V$. We assume that K single-antenna User Equipments (UEs) are active and transmit Y-polarized signals when traveling in the Z direction. We denote by $\mathbf{s}_k = [s_{k,x}, s_{k,y}, s_{k,z}]^T$ the arbitrary location for source k.

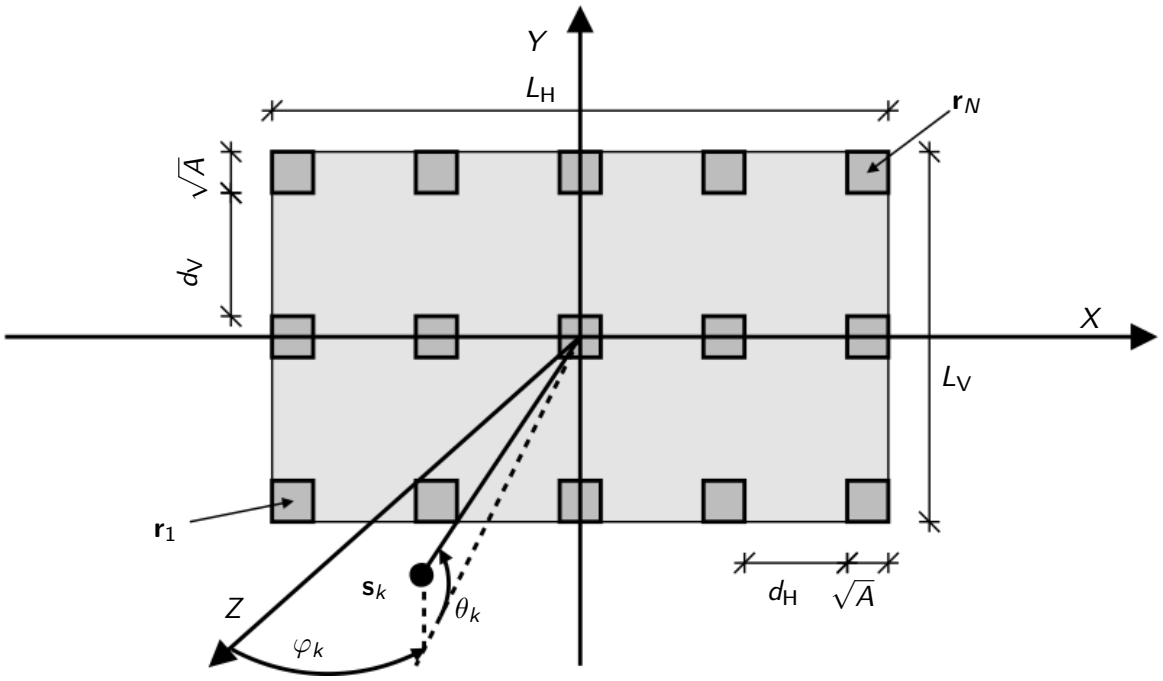

Figure 5: Diagram of the 2D planar array located in the XY-plane.

2.3.1 System Model

We consider the uplink and assume that perfect channel state information is available. The received signal is given by

$$\boldsymbol{\eta} = \sum_{k=1}^{K} \mathbf{h}_k \xi_k + \mathbf{n}, \tag{12}$$

where $\xi_k \sim \mathcal{N}_{\mathbb{C}}(0, p_k)$ is the data from UE k, $\mathbf{h}_k = [h_{k1}, \ldots, h_{kN}]^{\mathsf{T}} \in \mathbb{C}^N$ denotes the channel of UE k and $\mathbf{n} \in \mathbb{C}^N$ indicates the thermal Gaussian noise with independent and identically distributed (i.i.d.) elements $\in \mathcal{N}_{\mathbb{C}}(0, \sigma^2)$. The noise noise power σ^2 is computed as

$$\sigma^2 = (k_B B T) \cdot NF, \tag{13}$$

where $k_B \approx 1.38 \cdot 10^{-23}$J/K is the Boltzmann constant, B denotes the transmission bandwidth, T indicates the temperature and NF is the noise figure of the receiver.

2.3.2 Channel Model

To model $\mathbf{h}_k$, we consider a lossless isotropic antenna located at $\mathbf{s}_k$ that transmits a Y-polarized signal when traveling in the Z direction. The squared amplitude ζ_{kn} of the free-space channel coefficient at receive antenna n, located at $\mathbf{r}_n$, is given by [2, 5]

$$\zeta_{kn} = \frac{1}{12\pi} \sum_{i=0}^{1} \sum_{j=0}^{1} \frac{g_i(s_{k,x} - r_{n,x})\, g_j(s_{k,y} - r_{n,y})\, |s_{k,z}|}{\left[g_j^2(s_{k,y} - r_{n,y}) + s_{k,z}^2\right] \sqrt{g_i^2(s_{k,x} - r_{n,x}) + g_j^2(s_{k,y} - r_{n,y}) + s_{k,z}^2}} + \frac{1}{6\pi} \sum_{i=0}^{1} \sum_{j=0}^{1} \tan^{-1}\left(\frac{g_i(s_{k,x} - r_{n,x})\, g_j(s_{k,y} - r_{n,y})}{|s_{k,z}| \sqrt{g_i^2(s_{k,x} - r_{n,x}) + g_j^2(s_{k,y} - r_{n,y}) + s_{k,z}^2}} \right) \tag{14}$$

Parameter	Value	Parameter	Value
Carrier frequency	$f_c = 300\,\text{GHz}$	Wavelength	$\lambda = 1\,\text{mm}$
Antenna area	$A = \left(\frac{\lambda}{4}\right)^2 = 0.0625\,\text{mm}^2$	Array height	$h = 5\,\text{m}$
Horizontal spacing	$d_H = 10\lambda = 10\,\text{mm}$	Vertical spacing	$d_V = 10\lambda = 10\,\text{mm}$

Table 1: Array parameters.

where

$$g_i(\alpha) \triangleq \sqrt{A}/2 + (-1)^i \alpha. \tag{15}$$

The channel entry $h_{kn} = |h_{kn}| e^{-\mathrm{j}\phi_{kn}}$, denoting the channel from UE k to receive antenna n, is obtained as

$$|h_{kn}| = \sqrt{\zeta_{kn}} \tag{16}$$

$$\phi_{kn} = 2\pi \bmod \left(\frac{d_{kn}}{\lambda}, 1\right) \tag{17}$$

where ζ_{kn} is defined in (14) and $d_{kn} = ||\mathbf{s}_k - \mathbf{r}_n||$.

2.3.3 Spectral Efficiency and Throughput

To decode ξ_k, the vector $\boldsymbol{\eta}$ is processed with the combining vector $\mathbf{v}_k \in \mathbb{C}^N$. By treating the interference as noise, the Spectral Efficiency (SE) for UE k, measured in bit/s/Hz, is

$$\text{SE} = \log_2(1 + \gamma_k) \tag{18}$$

where

$$\gamma_k = \frac{p_k \left|\mathbf{v}_k^\dagger \mathbf{h}_k\right|^2}{\sum_{i \neq k} p_i \left|\mathbf{v}_k^\dagger \mathbf{h}_i\right|^2 + \sigma^2 ||\mathbf{v}_k||^2}, \tag{19}$$

is the Signal-to-Interference-plus-Noise Ratio (SINR). We consider both Maximum Ratio (MR) and Minimum Mean Square Error (MMSE) combining. MR has low computational complexity and maximizes the power of the desired signal, but neglects interference. MMSE has higher complexity, but it maximizes the SINR in (19). In the first case, we have that

$$\mathbf{v}_k^{\text{MR}} = \frac{\mathbf{h}_k}{||\mathbf{h}_k||}, \tag{20}$$

while in the second case

$$\mathbf{v}_k^{\text{MMSE}} = \left(\sum_{i=1}^{K} p_i \mathbf{h}_i \mathbf{h}_i^\dagger + \sigma^2 \mathbf{I}_N\right)^{-1} \mathbf{h}_k, \tag{21}$$

with $\mathbf{I}_N$ being the identity matrix of order N.

The aggregate throughput of the system, measured in bit/s, can be computed as

$$\text{Troughput} = B \sum_{k=1}^{K} \log_2(1 + \gamma_k). \tag{22}$$

Parameter	Value	Parameter	Value
Coverage Area	Square cell	Cell-side length	$L = 20\,\text{m}$ or $L = 50\,\text{m}$
Carrier frequency	$f_c = 300\,\text{GHz}$	Transmission Bandwidth	$B = 3 - 30\,\text{GHz}$
UE transmit power	$p_k = P = 0 - 30\,\text{dBm}$	Noise Figure	$NF = 8\,\text{dB}$
UE Distance	$d_C = 5 - 50\,\text{m}$	Combiner	MR or MMSE

Table 2: System parameters.

2.4 Performance Analysis in LoS Single-UE Scenario

We begin by evaluating the system performance in a single UE scenario, i.e., with $K = 1$. In this case, (22) reduces to

$$\text{Throughput} = B \log_2 (1 + \gamma_1) \tag{23}$$

with

$$\gamma_1 = \frac{p_1 \left| \mathbf{v}_1^\dagger \mathbf{h}_1 \right|^2}{\sigma^2 ||\mathbf{v}_1||^2} \tag{24}$$

being the Signal-to-Noise-Ratio (SNR). With MR combining, i.e., $\mathbf{v}_1 = \mathbf{h}_1$, the SNR reduces to

$$\gamma_1 = \frac{p_1 \left| \mathbf{h}_1^\dagger \mathbf{h}_1 \right|^2}{\sigma^2 ||\mathbf{h}_1||^2} = \frac{p_1}{\sigma^2} \mathbf{h}_1^\dagger \mathbf{h}_1 = \frac{p_1}{\sigma^2} \sum_{n=1}^{N} \zeta_{1n}. \tag{25}$$

If the path loss is approximately the same over all the receiving antennas, i.e. $\zeta_{1n} \approx \zeta_1$, then we obtain

$$\gamma_1 = N \frac{\zeta_1 p_1}{\sigma^2}. \tag{26}$$

We notice that MMSE and MR provide exactly the same throughput and SNR when $K = 1$.

2.4.1 System Parameters

We consider a carrier frequency $f_c = 300\,\text{GHz}$ that corresponds to a wavelength $\lambda = 1$ mm. We assume that square patch antennas of area $A = (\lambda/4)^2$ are used. The receiver is equipped with $N = 1024$ antennas, organized in a $N_H = 32 \times N_V = 32$ uniform square array with spacing between adjacent antenna edges equal to $d_H = d_V = 10\lambda$, as shown in Fig. 5. From (8) and (9), we obtain $L_H = L_V = 318\lambda$, and the maximum physical dimension of the receiving array L_A is

$$L_A = \sqrt{L_H^2 + L_V^2} = 318\sqrt{2}\lambda \sim 45\,\text{cm}. \tag{27}$$

Plugging (27) into (7) yields $d_{FA} \sim 404$ m.

We consider an industrial scenario for which the coverage area is a squared cell of side length L. We consider two cases: $L = 20\,\text{m}$ (corresponding to a small-scale scenario) or $L = 50\,\text{m}$ (corresponding to a large-scale scenario) [6]. We assume the receiver to be located $h = 5\,\text{m}$ higher than the UE on the vertical axis. Therefore, the UE is located in the XZ-plane at height h and has coordinates $(x, -h, z)$ with $|x| \leq \frac{L}{2}$ and $|z| \leq \frac{L}{2}$. We denote with d_C the distance of the UE from the receive array.

The parameters used across the simulations are summarized in Tab. 1 and Tab. 2 and are based on the considerations reported in our previous deliverable [7].

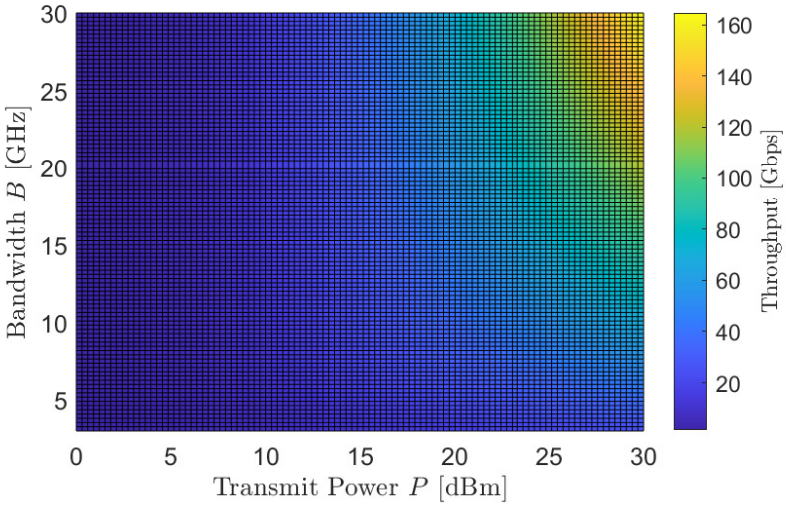

(a) Throughput.

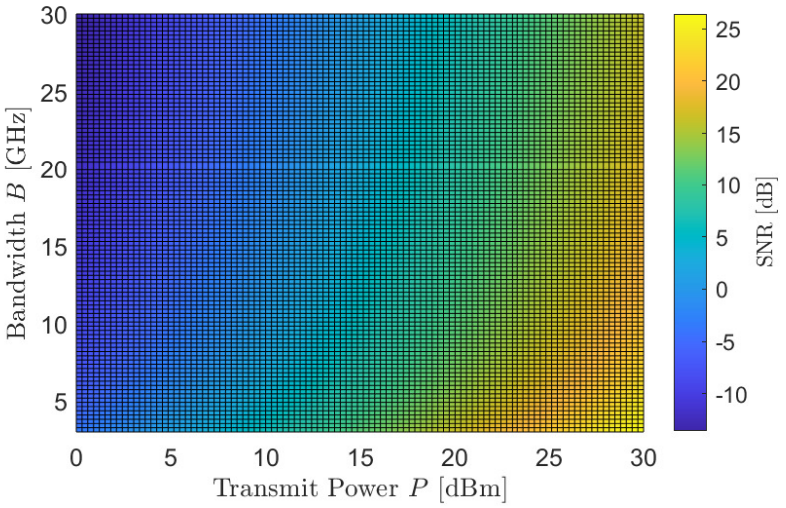

(b) SNR.

Figure 6: Throughput and SNR with $K = 1$ and $f_c = 300$ GHz. The UE is at distance $d = 10$ m.

2.4.2 Throughput Analysis

Figs. 6a and 6b show the throughout (23) (in Gbps) and the SNR (24) (in dB) as a function of the bandwidth B and the transmit power $p_1 = P$. The former varies from 3 GHz to 30 GHz, whereas the latter takes values in the range from 0 dBm to 30 dBm. We do not consider $B > 0.1\, f_c = 30$ GHz in order for the signal to be narrow band. The UE is located at $(0, -5, 5\sqrt{3})$ m so that the distance $d_C = 10$ m. Assume that the transmitter is a low-end user. In this case, a bandwidth of 2.16 GHz and a transmit power of 0 dBm are available. This yields a throughput of 1.4 Gbps, which corresponds to an SNR of -2.1 dB. The throughput increases up to 165 Gbps if $B = 30$ GHz and $P = 25$ dBm, which is the case of a high-end user. The results of Fig. 6a show that there is no bandwidth and transmit power combination that results in a throughput higher than 165 Gbps. In Sec. 2.6, we will show that a significant improvement of the throughput is achievable by spatially multiplexing multiple UEs in the system.

Let us now consider a squared cell of size $L = 20$m, which corresponds to the small room scenario described in [6]. We randomly position the UE within the cell, so that it has coordinates $(x, -5\,\text{m}, z)$ with $x_{\min} \leq |x| \leq \frac{L}{2}$ and

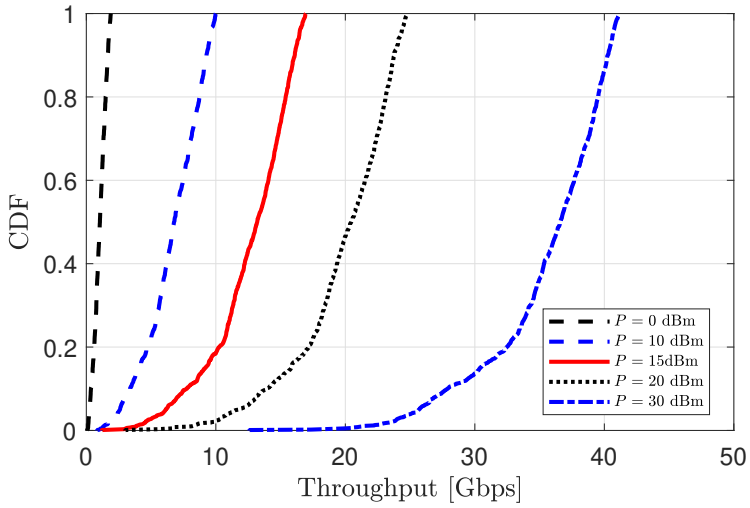

(a) Varying P with N = 1024.

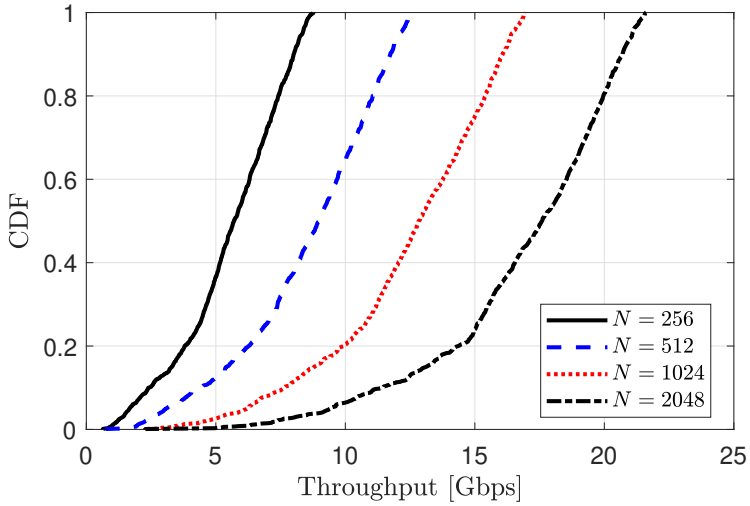

(b) Varying N with P = 15 dBm

Figure 7: Cumulative Distribution Function (CDF) of the throughput with $K = 1$, $f_c = 300$ GHz and $B = 5$ GHz. The coverage area has a radius of 20 m, corresponding to a small industrial scenario.

$z_{\min} \leq |z| \leq \frac{L}{2}$ where $x_{\min} = z_{\min} = 50$ cm denote minimum distances from the $x-$axis and z-axis, respectively. Assuming a bandwidth $B = 5$ GHz, we calculate the throughput as per (22).

From the results of Fig. 7a, we see that if $P = \{0, 10\}$ dBm, the throughput is always lower than 10 Gbps regardless of the position of the UE, therefore we need $P > 10$ dBm. If $P = 15$ dBm, the throughput is lower than 10 Gbps with 20% probability, and between 10 and 18 Gbps with 80% probability. If $P \geq 20$ dBm, the probability that the throughput is lower than 10 Gbps is negligible. Moreover, if $P = 20$ dBm, the throughput is between 10 and 20 Gbps with a 50% probability, and between 20 and 25 Gbps with a 50% probability. Eventually, if $P = 30$ dBm, the throughput is between 20 and 30 Gbps with a 15% probability, between 30 and 40 Gbps with 85% probability. Since $P \geq 20$ dBm, is impractical at very high-frequency (THz band) with the currently available technology [8], in the remainder of Sec.2.4 we assume $P = 15$ dBm.

In Fig. 7b, we calculate the throughput as per (23) varying the number of receiving antennas N with $P = 15$ dBm. We see that if $N = 256$, the throughput is always lower than 10 Gbps, for a bandwidth $B = 5$ GHz.

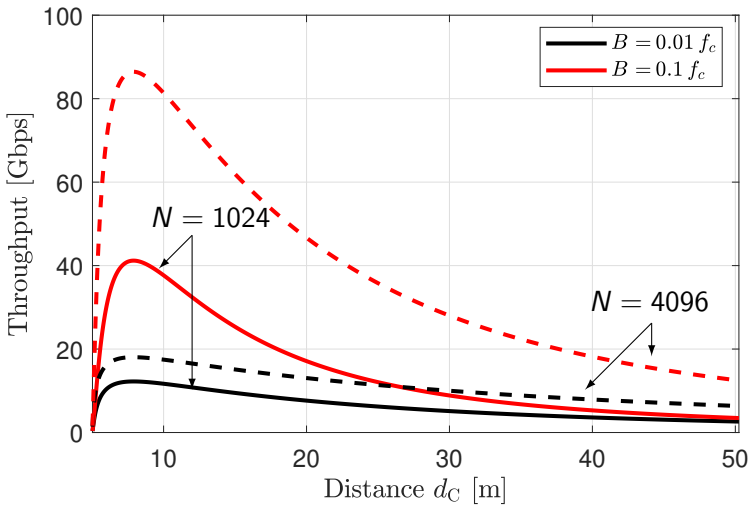

Figure 8: Throughput as a function of the UE's distance with $f_c = 300$ GHz and $P = 15$ dBm.

Therefore, if a higher throughput is required, we need $N > 256$. If $N = 512$, the throughput is lower than 10 Gbps with a 60% probability, and between 10 and 12.5 Gbps with a 40% probability. If $N = 1024$, the throughput is lower than 10 Gbps with 20% probability, between 10 and 15 Gbps with a 50% probability, and between 15 and 17.5 Gbps with a 30% probability. Eventually, if $N = 2048$, the throughput is lower than 10 Gbps with a 10% probability, between 10 and 15 Gbps with 10% probability, between 15 and 20 Gbps with 60% probability, and between 20 and 22.5 Gbps with 20% probability.

In Fig. 8, we calculate the throughput as per (23) with $P = 15$ dBm varying the distance $d_C \in [5, 50]$ m with $N = 1024$ or $N = 4096$. We consider both cases $B = 0.01\, f_c = 3$ GHz and $B = 0.1\, f_c = 30$ GHz. We point out that the impact of B and N on the throughput in (23) is different depending on whether we operate in a high or low SNR regime. More precisely, let us consider the path loss to be approximately the same for all the receiving antennas, i.e. $\zeta_{1n} \sim \zeta_1$, and let us assume $\gamma_1 >> 1$, i.e., we operate in high-SNR regime. Under these conditions, (23) simplifies into

$$\text{Throughput} = B \log_2 (1 + \gamma_1) \sim B \log_2 \gamma_1 = B \log_2 \left(\frac{\zeta_1 N p_1}{k_B N_0 B} \right). \tag{28}$$

which shows that, in the high-SNR regime, the throughput depends on N as $\log_2 N$. The dependence on B is not linear because of the term $\log_2 (\zeta_1 N p_1 / (k_B N_0 B))$. On the other hand, if $\gamma_1 << 1$, i.e. we operate in low-SNR regime, then (23) can be simplified as

$$\text{Throughput} = B \log_2 (1 + \gamma_1) \sim B \gamma_1 = \frac{B \zeta_1 N p_1}{k_B N_0 B} = \frac{\zeta_1 N p_1}{k_B N_0}. \tag{29}$$

Thus, in the low-SNR regime the throughput does not depend on the bandwidth B and grows linearly with N.

From the results of Fig. 8, we see that as the distance d_C increases, SNR gets lower and the throughput is better approximated by (29) until the dependency on B becomes negligible. For example, we see that if $N = 1024$, the throughput is the same at $d_C = 50$ m in both cases $B = \{3, 30\}$ GHz. On the other hand, at shorter distances, the SNR is higher, and the throughput increases with the bandwidth. For example, we see that at $d_C = 6$ m, with $B = 3$ GHz and $N = 1024$, the throughput is 11 Gbps. By increasing the bandwidth to $B = 30$ GHz, the throughput becomes 37 Gbps, and by increasing the number of receiving antennas to $N = 4096$, the throughput is 17 Gbps. Therefore, we can conclude that, at short distances, where we typically do not operate in a low-SNR regime, an increase in the throughput can be observed by increasing the bandwidth or the number of antennas. However, at long distances, we typically operate in the low-SNR regime, and increasing the bandwidth is not

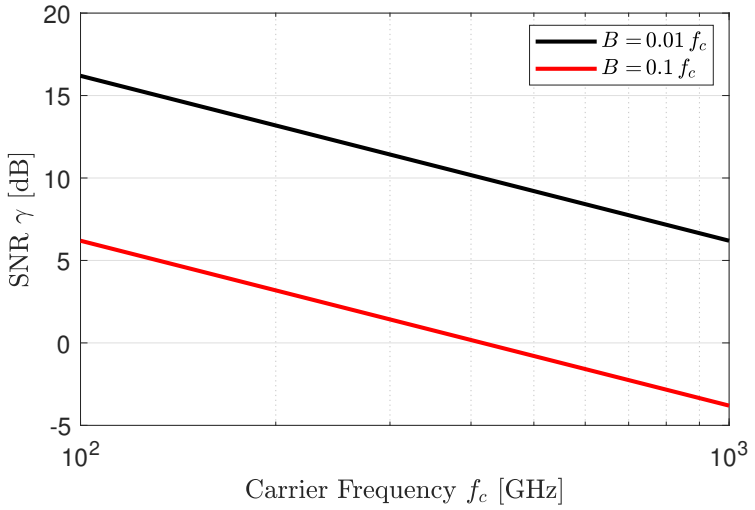

(a) SNR

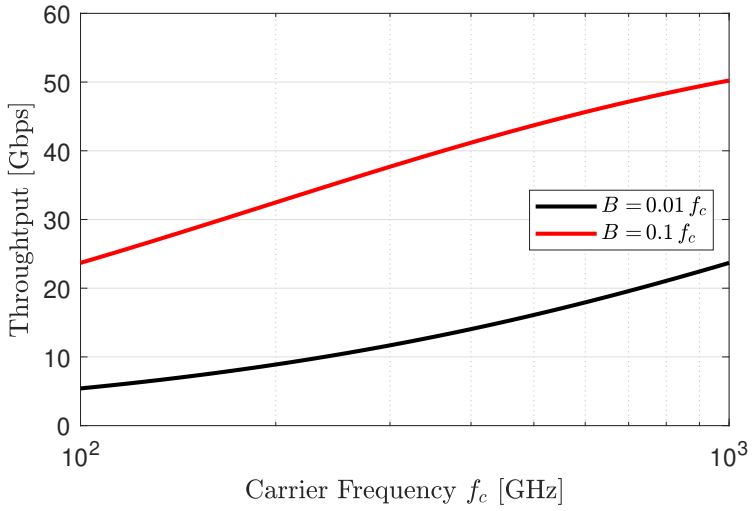

(b) Throughput

Figure 9: SNR and throughput as functions of the carrier frequency f_c with $P = 15$ dBm and $N = 1024$. The UE is at distance $d = 10$ m.

beneficial in terms of throughput, while the number of antennas becomes more important as the throughput tends to grow linearly with N. It is worth noting that we can not indefinitely exploit this trend. In fact the more N grows, the more the SNR increases, and the less accurate the low-SNR regime approximation is going to be.

2.4.3 Impact of the Carrier Frequency

Let us consider the same receiving array described in Sec. 2.4.1, and assume that the UE has coordinates $(0, -5\,\text{m}, 5\sqrt{3})\,\text{m}$ so that $d_C = 10\,\text{m}$. The transmit power is $P = 15\,\text{dBm}$ and we consider both the cases of bandwidth $B = 0.01\, f_c$ or $0.1\, f_c$. Fig. 9a and 9b show, respectively, the SNR and the throughput as functions of the carrier frequency f_c varying between 100 GHz and 1 THz.

From the results of Fig. 9a, we see that the SNR is always lower if $B = 0.1\, f_c$ compared to the case $B = 0.01\, f_c$,

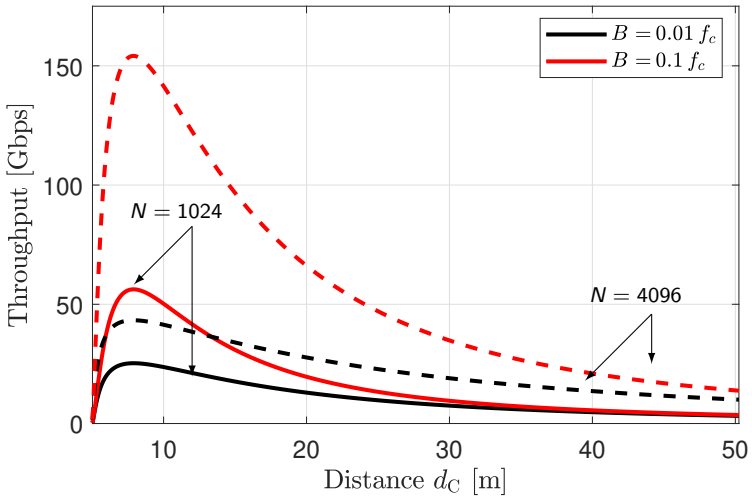

Figure 10: Throughput as a function of the UE's distance with $f_c = 1$ THz and $P = 15$ dBm.

as more thermal noise power is included in the useful bandwidth as per (13). For example, we see that with $f_c = 300$ GHz, we have an SNR of 11 dB and 1 dB, respectively. However, even though a larger bandwidth comes with a lower SNR, from (23) it is clear that the bandwidth has a double impact on the throughput. In fact, on one hand, the factor B tends to linearly increase the throughput, but, on the other hand, larger bandwidths come with lower SNRs that tends to decrease the throughput. Fig. 9b shows see that if $B = 0.1\, f_c$, despite the SNR being larger than in the case of $B = 0.01\, f_c$, the throughput is higher across the whole frequency range, with the difference being higher as f_c grows. In order to increase this throughput, we can reduce the distance d or increase the number of receiving antennas N. In Fig. 10, we show the throughput with $d \in [5, 50]$ m and both $N = 1024$ and 4096, where in the second case, we are considering $N_H = N_V = 64$, which means that the array dimensions are doubled both horizontally and vertically. We see that all the considerations we did about Fig. 8 still apply to 10. For example, we see that if $N = 1024$, the throughput is the same at $d_C = 50$ m in both cases $B = \{3, 30\}$ GHz. However, at shorter distance, the SNR is higher, and the throughput is larger as the bandwidth increases. For example,we see that at $d_C = 6$ m, with $B = 3$ GHz and $N = 1024$, the throughput is 23 Gbps. By increasing the bandwidth to $B = 30$ GHz, the throughput becomes 50 Gbps, and by increasing the number of receiving antennas to $N = 4096$, the throughput is 41 Gbps. We point out that even by transmitting at $f_c = 1$ THz, with $B = 100$ GHz and $N = 4096$, the throughput is 150 Gbps. Therefore, we need to spatially multiplex multiple UEs in order to achieve an aggregate throughput of 1 Tbps as we will discuss in Sec. 2.6.

2.5 Impact of a Mismatched Design

The aim of this section is to quantify the performance of a single UE MIMO communication system designed on the basis of the parabolic and planar channel models. We begin by first looking into the phase error introduced by the approximations and then into the impact on the communication metrics.

2.5.1 Phase Error Analysis

The approximation of d_n through the parabolic and planar models generates a mismatch between the angles of the channel matrices elements given by

$$\Delta\phi_n^{(parabolic)} = \frac{2\pi}{\lambda}|d_n - d_n^{(parabolic)}|, \tag{30}$$

$$\Delta\phi_n^{(planar)} = \frac{2\pi}{\lambda}|d_n - d_n^{(planar)}|. \tag{31}$$

The mismatch occurs between the transmitting antenna and each receiving antenna, but it can be conveniently summarized into a single metric in various ways depending on the application of interest. We consider the maximum values of the angle mismatch

$$\Delta\phi_{max}^{(parabolic)} \triangleq \max_n \left\{\Delta\phi_n^{(parabolic)}\right\}, \tag{32}$$

$$\Delta\phi_{max}^{(planar)} \triangleq \max_n \left\{\Delta\phi_n^{(planar)}\right\}. \tag{33}$$

which are meaningful metrics, especially in those applications dominated by worst-case error such as spatial-multiplexing [3]. Let us consider the receiving array in Fig. 5 whose parameters are summarized in Tab. 1. We consider a single UE to be located at $(0, -h, z)$ with $z \in [0.5\,, 50]$ m. Therefore, the distance d_C is given by

$$d_C = \sqrt{h^2 + z^2}. \tag{34}$$

Let us assume we need $\Delta\phi_{max} \leq \pi/8$. From Fig. 11a, we observe that at 300 GHz $\Delta\phi_{max}^{(planar)}$ is above the threshold of $\pi/8$ over the whole distances interval which means that the planar model would be too rough within any distance $d \leq 50$m. On the other hand, we see that $\Delta\phi_{max}^{parabolic}$ is below the threshold as long as $d \geq 6$m. In a number of industrial scenarios the BS is 5m higher than the UEs [6]. Therefore in these scenarios the distance between the BS and the UEs is typically greater than 6m and the parabolic model can be an accurate approximation. In Fig. 11b we investigate the case $f_c = 1$ THz and $N = 4096$. Since the array dimensions are doubled both horizontally and vertically with respect to the case of Fig. 11a, we expect both the planar and the parabolic approximations to be less accurate. In fact, we can see that the planar curve is above the threshold of $\pi/8$ over the whole distances interval once again, which means that the planar model would be too rough within any distance $d \leq 50$m also at $f_c = 1$ THz. This conclusion is supported by the $d_{FA} \sim 5.4$ km, which implies the UE is very deep into the near-field region of the receiver. Therefore, the planar approximation is not accurate.

On the other hand, we see that $\Delta\phi_{max}^{parabolic}$ is below the threshold for any distance $d \geq 5$ m. Therefore, the parabolic model can be accurate at 1 THz, not only for $d \geq 6$ m, but also for $5\,m \leq d \leq 6\,m$.

2.5.2 Throughput Analysis

We now investigate the impact of a mismatched design. Consider the same scenario described in Sec. 2.4.3, and focus on $f_c = 300$ GHz and $f_c = 1$ THz. As discussed in Sec. 2.4.3, we consider $N = 1024$ with $f_c = 300$ GHz, and $N = 4096$ with $f_c = 1$ THz. We assume that the transmission bandwidth B is 5 GHz regardless of the carrier frequency. We calculate the throughput as per (22) and compute the combiner according to the spherical, parabolic and planar models.

From Fig. 12a, we see that if $f_c = 300$ GHz, the difference between the spherical and parabolic model is negligible. This means that the mismatch does not have a significant impact on the throughput for any $d_C \in [5, 50]$ m. On the other hand, we see that the planar model suffers from a severe mismatch loss. More precisely, with $d_C = 50$ m, the throughput associated with the spherical and planar models are 2.6 and 1.7 Gbps, respectively. The difference significantly increases as d_C decreases, until the maximum gap at $d_C = 6$ m, where the throughput are 12 and 0.36 Gbps, respectively.

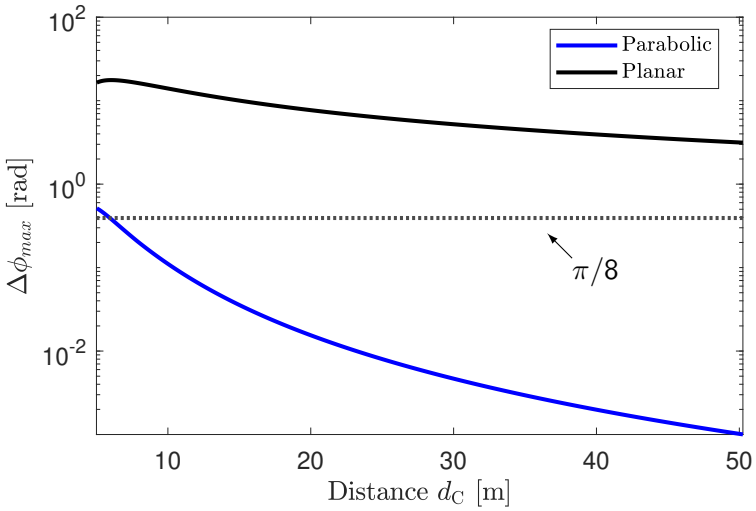

(a) $f_c = 300$ *GHz and* $N = 1024$.

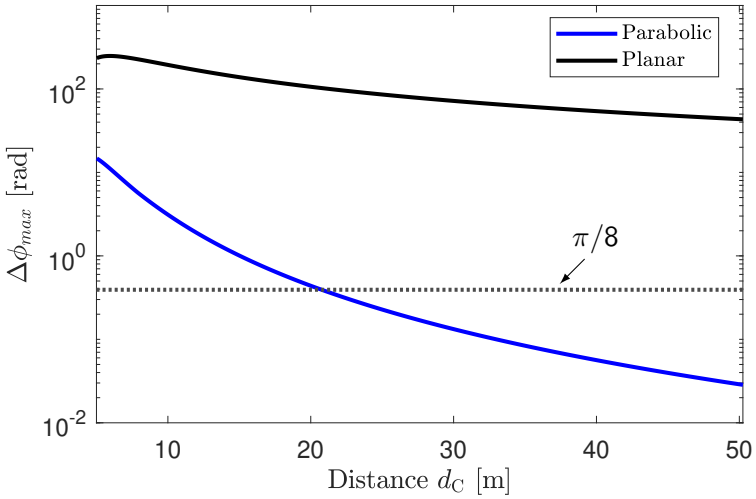

(b) $f_c = 1$ *THz and* $N = 4096$.

Figure 11: Analysis of $\Delta\phi_{max}^{parabolic}$, $\Delta\phi_{max}^{planar}$ *as functions of UE's distance* d *with* $f_c = 300$ *GHz and* $N = 1024$. *The case with* $f_c = 1$ *THz and* $N = 4096$ *is also considered.*

Fig. 12b shows that if $f_c = 1$ THz, the impact of the mismatch is larger at higher frequencies. More precisely, on one hand, we see that the impact of the mismatch using the planar model is so strong that the throughput is always lower than 180 Mbps with both $N = \{1024, 4096\}$. On the other hand, comparing the spherical and parabolic models, we observe that the impact of the mismatch is negligible with $N = 1024$, but it is not in the case of $N = 4096$. In fact, in the latter case, the receiving array is 4 times larger than with $N = 1024$. Therefore, the local approximation of the spherical wave fronts as paraboloids or planes is less tight, and the parabolic and planar models are less accurate. However, the impact of the mismatch using the parabolic model is still negligible for $d_C \geq 15$ m but it is stronger as d_C decreases. The maximum gap is reached at $d_C = 6$ m where the throughput computed according to the spherical and parabolic models are 39 and 9 Gbps, respectively.

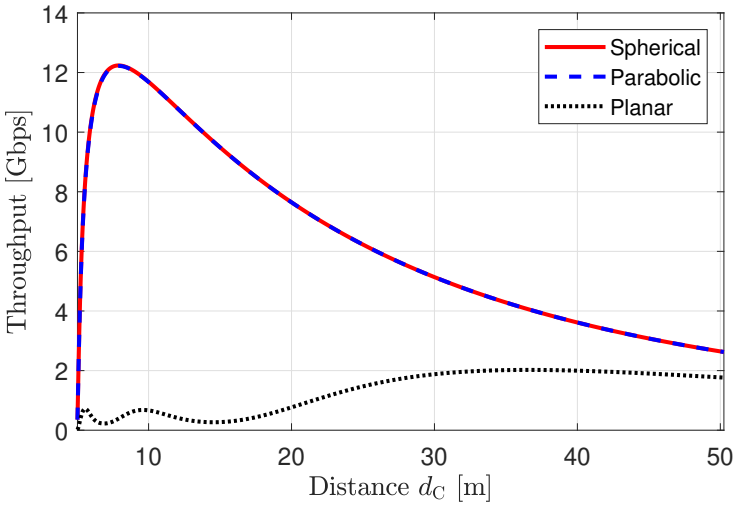

(a) $f_c = 300$ *GHz and* $N = 1024$.

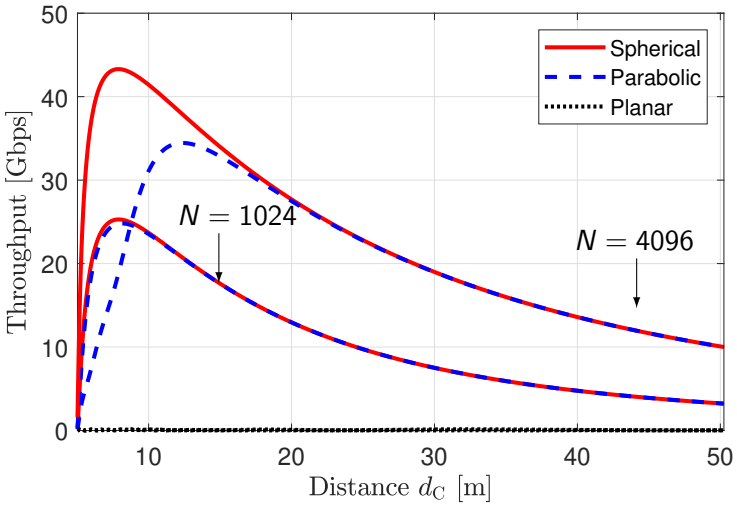

(b) $f_c = 1$ *THz and* $N = \{1024, 4096\}$.

Figure 12: Throughput with $f_c = 300$ *GHz or* $f_c = 1$ *THz,* $B = 0.01\, f_c$, $P = 15$ *dBm and* $N = 1024$ *or* 4096.

2.6 Performance Analysis in LoS Multi-UE Scenario

We now extend the analysis to multi-user LoS scenarios where K UEs are simultaneously active and served in the uplink by exploiting the spatial multiplexing capabilities of the receive array.

2.6.1 Interference Gain

We start considering a two-UEs scenario (i.e., $K = 2$). In particular, we analyze the normalized interference gain, given by (as obtained from (19))

$$\text{Normalized Interference Gain} = \frac{|\mathbf{v}_1^\dagger \mathbf{h}_2|^2}{||\mathbf{v}_1||^2} \tag{35}$$

where $\mathbf{v}_1$ is computed according to the spherical model. Both the MMSE and MR combiners are considered. The receiving array is shown in Fig. 5 and its geometric parameters are summarized in Tab. 1. Let us now

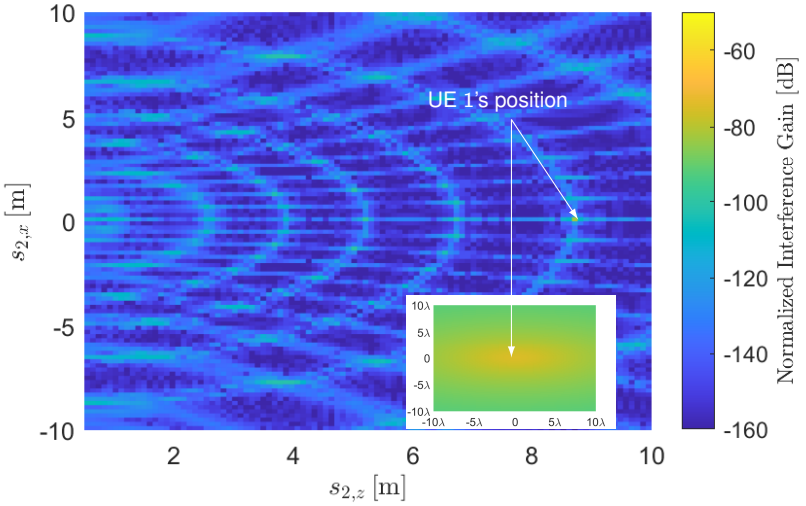

(a) MMSE.

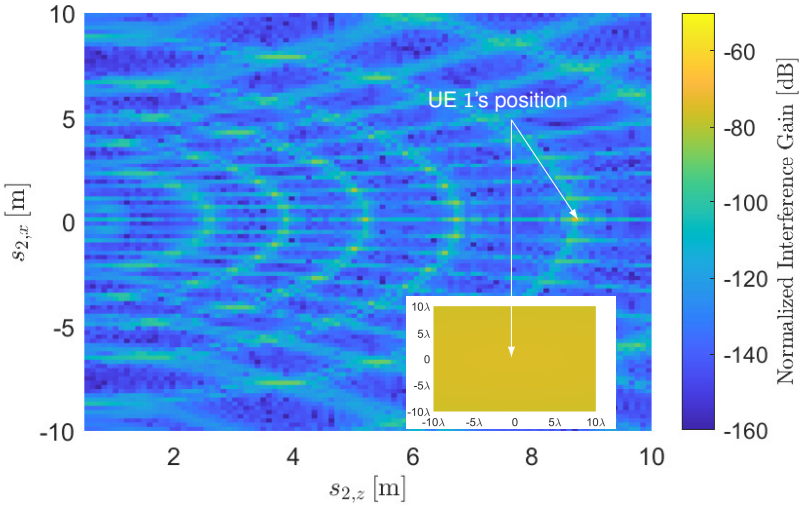

(b) MR .

Figure 13: Interference gain using MMSE and MR combiners for a fixed UE 1 *as a function of different locations of an interfering UE* 2*.*

consider a square cell of size $L = 20$m, which corresponds to the small room scenario described in [6], centered in $(0, -5\,\mathrm{m}, 0)$. We assume that UE 1 is located at the fixed position $\mathbf{s}_1 = \left(0, -5\,\mathrm{m}, 5\sqrt{3}\,\mathrm{m}\right)$, whereas the interfering UE 2 is randomly positioned within the cell, so that its coordinates are $\mathbf{s}_2 = (s_{2,x}, -5\,\mathrm{m}, s_{2,z})$ with $s_{x,\min} \leq |s_{2,x}| \leq \frac{L}{2}$ and $s_{z,\min} \leq |s_{2,z}| \leq \frac{L}{2}$ where $s_{x,\min} = s_{z,\min} = 50\,\mathrm{cm}$ denote the minimum distances from the $x-$axis and z-axis, respectively. Since we assume $f_c = 300\,GHz$, the Fraunhofer array distance $d_{FA} \approxeq 404\,\mathrm{m}$, both the UEs are in the near-field region of the receiving array. We assume that both UEs transmit with the same power $p_1 = p_2 = 15\,\mathrm{dBm}$.

Fig. 13 reports the normalized interference gain with MMSE (Fig. 13a) and MR (Fig. 13b). Each figure contains a magnification around UE 1's location, in which the distance of UE 2 from UE 1 is measured in wavelengths (for a total span of $10\lambda \times 10\lambda = 1 \times 1\,\mathrm{cm}^2$). Fig. 13a shows that the interference with MMSE is high only in small space regions, one of which is around UE 1, whose semi-major axis (along both directions) is on the order of the wavelength. This phenomenon is referred to as *beamfocusing*. The focusing does not occur only at UE 1's position because the spacing between the antenna elements is $d_H = d_V = 10\lambda > \frac{\lambda}{2}$. Therefore, there

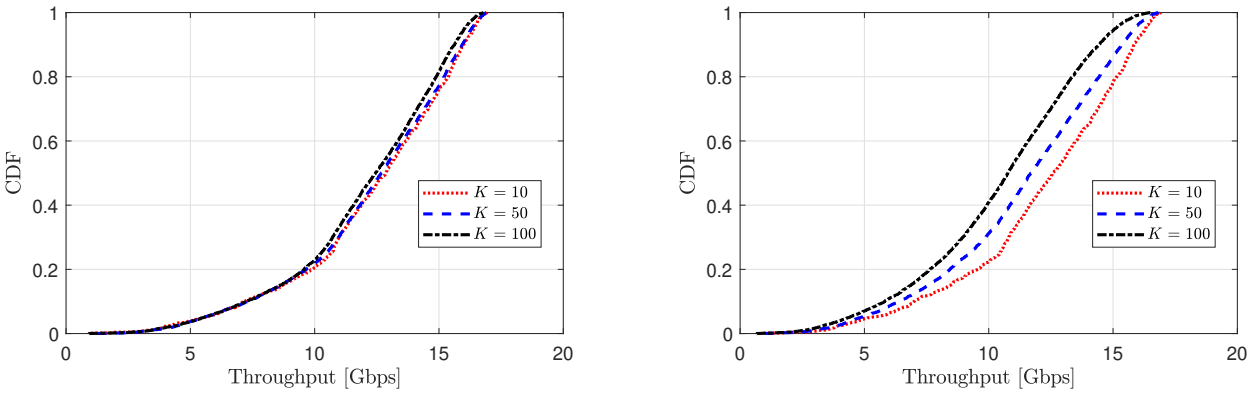

(a) MMSE. *(b) MR.*

Figure 14: CDF of the throughput per UE with $f_c = 300$ GHz, $K = \{10, 50, 100\}$, and both MMSE and MR.

is a spatial aliasing effect that results in multiple focusing points. Currently, $d_H, d_V \leq \frac{\lambda}{2}$ is impractical at very high frequencies since λ is very small, so that aliasing is unavoidable in practical applications. In order to do beamfocusing, we need to exploit the curvature of the transmitted spherical wave fronts over the array aperture to separate UEs in the depth domain. This means that beamfocusing is only possible in the near-field, and more precisely the distance between the receiver array and the transmitter must be lower than $\frac{d_{FA}}{10}$ [9]. In our case this condition is met since $\frac{d_{FA}}{10} \approx 40\,\text{m}$, and the maximum distance from the array of any UE in the cell is $15\,\text{m}$. In the far-field of the receiving array, where the spherical wave fronts are essentially planar over the receiving array, it is only possible to separate UEs in different directions, but not in the depth domain. Fig. 13b shows that beamfocusing is also possible with the MR, and the UEs can still be separated in both the direction and the depth domains. However, interference is always higher than with MMSE. Therefore, we expect MMSE to have better performance than MR, for any UEs distribution within the cell, in terms of aggregate throughput. The price to pay is an increase in the implementation costs.

2.6.2 Throughput Analysis

Let us consider the same scenario described in Sec. 2.6.1 with $K = \{10, 50, 100\}$. We assume that the UEs are uniformly distributed in the cell so that they have coordinates $(s_{k,x}, -5\,\text{m}, s_{k,z})$ with $s_{x,\min} \leq |s_{k,x}| \leq \frac{L}{2}$ and $s_{z,\min} \leq |s_{k,z}| \leq \frac{L}{2}$ where $s_{x,\min} = s_{z,\min} = 50\,\text{cm}$. We compute the UEs density per 100m^2 as

$$\rho = \frac{100K}{L^2}, \qquad \left[\frac{UEs}{100\text{m}^2}\right]. \tag{36}$$

Each UE transmits with the same power $p_k = P = 15\,\text{dBm}$ over a bandwidth $B = 5\,\text{GHz}$. We consider both MMSE and MR, and calculate the throughput as per (22).

In Fig. 14 we show the CDF of the throughput with MMSE (Fig. 14a) and MR (Fig. 14b). From Fig. 14a we see that the all the curves are almost overlapped. This means that, when MMSE is used, interference does not have a significant impact on the throughput of each UE with $K \leq 100$. We also note that the throughput is lower than $10\,\text{Gbps}$ with a 20% probability, between $10\,\text{Gbps}$ and $15\,\text{Gbps}$ with a 60% probability, and between $15\,\text{Gbps}$ and $17.5\,\text{Gbps}$ with a 20% probability. In Fig. 14b we can observe a different trend because MR is not designed to cancel the interference between UEs, which significantly impacts the performance. More precisely, we see that the more UEs are active at the same time the more the CDF of the throughput is shifted to the left. For any given UEs distribution, the throughput each UE gets is lower than with MMSE, with the difference being higher as K increases. For example, it can be seen that, with $K = 10$, the CDF of the throughput is almost the same for both the combiners. However, in passing from $K = 10$ to $K = 100$ the throughput is essentially the same with the MMSE, but it gets worse with the MR. More precisely, using the MR, the throughput is

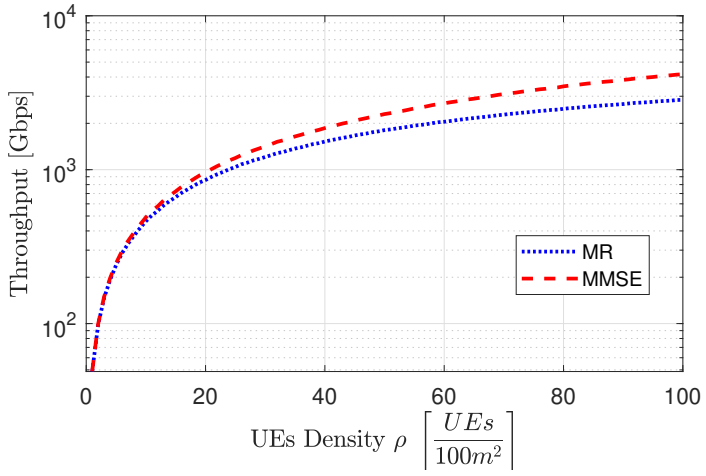

Figure 15: Analysis of aggregate throughput as a function of UEs density with $f_c = 300$ GHz and both MMSE and MR.

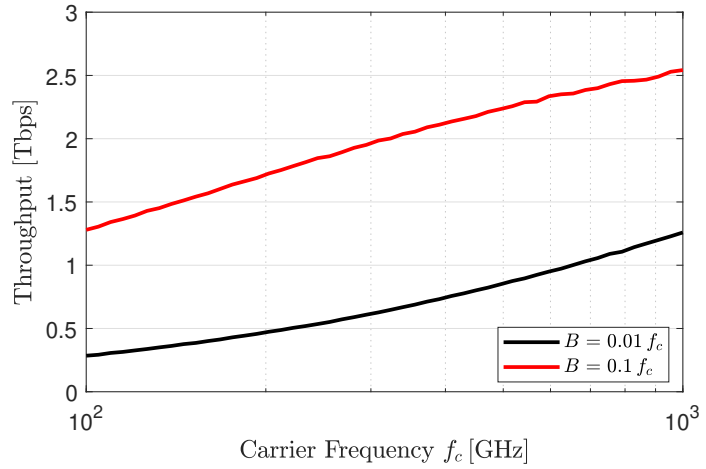

Figure 16: Analysis of the aggregate throughput as a function of carrier frequency f_c with $K = 80$.

lower than 10 Gbps with a 40% probability, between 10 Gbps and 15 Gbps with a 55% probability, and between 15 Gbps and 17.5 Gbps with a 5% probability.

In Fig. 15 we report the aggregate throughput in (22) as a function of the UEs density $\rho \in [1 - 100]$ $\left[\frac{UEs}{100m^2}\right]$. We see that even though the throughput is always higher with MMSE than with MR, the difference is smaller for lower UE densities and becomes larger as ρ grows, because MMSE combacts interference while MR does not. With $\rho = 20$ $\left[\frac{UEs}{100m^2}\right]$, the throughput is 960 and 860 Gbps with MMSE and MR, respectively. However, with $K = 100$ the throughput becomes 4.1 and 2.8 Tbps, respectively. It is worth noting that, with $\rho \geq 24$ $\left[\frac{UEs}{100m^2}\right]$, both the MMSE and the MR can achieve throughput larger than 1 Tbps.

2.6.3 Impact of the Carrier Frequency

Let us now consider the same scenario described in Sec. 2.6.2 with $\rho = 20$ $\left[\frac{UEs}{100m^2}\right]$, or, equivalently, $K = 80$. Without changing the receiving array physical dimension, we consider a carrier frequency $f_c \in [100\,\text{GHz} - 1\,\text{THz}]$, and we calculate the aggregate throughput as per (22) with an MR combiner.

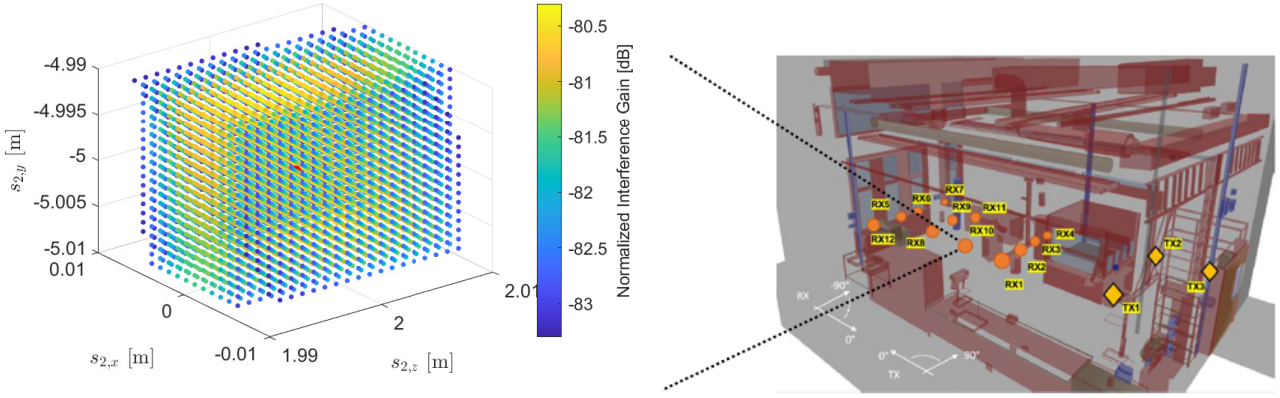

(a) Normalized interference gain within a cube of volume $20\lambda \times 20\lambda \times 20\lambda$ around the device.

(b) Example of an industrial scenario [6, Fig. 4].

Figure 17: Interference gain using MR for a fixed UE 1 as a function of different locations of an interfering UE 2, representing two sensors inside an industrial machine.

Fig. 16 shows that, even though a larger bandwidth decreases the SNR because more thermal noise is collected in the operational bandwidth (as shown in Fig. 9a), the linear dependence of the throughput on the bandwidth compensates for the SNR reduction resulting in a throughput increment with the bandwidth for both cases $B = \{0.01\, f_c, 0.1\, f_c\}$. We observed a similar behaviour in Fig. 9b in the single UE scenario, and, thanks to the interference cancellation provided by beamfocusing, the same trend is observed in the multi UEs scenario. More precisely, we see that the aggregate throughput is larger in the case of $B = 0.1\, f_c$ compared to the case $B = 0.01\, f_c$ for any carrier frequency f_c. Moreover, the throughput increases with the carrier frequency because we are assuming that the bandwidth scales up with the carrier frequency f_c. It is worth noting that, if $B = 0.1\, f_c$, the aggregate throughput is larger than 1 Tbps with f_c between 100 and 300 GHz, and above 2 Tbps with f_c between 300 GHz and 1 THz. On the other hand, if $B = 0.01\, f_c$, the throughput is between 0.25 and 0.5 Tbps with $f_c \in [100, 200]$ GHz, between 0.5 and 1 Tbps with $f_c \in [200, 700]$ GHz, and between 1 and 1.25 Tbps with $f_c \in [0.7, 1]$ THz.

2.6.4 Preliminary Results in Intra-Machine Industrial Scenario

We now consider an industrial scenario where a machine is equipped with $K = 2$ active sensors (referred to as UEs). An example is shown in Fig. 17b. The sensors transmit to the receiving array shown in Fig. 5, whose parameters are summarized in Tab. 1. We assume a carrier frequency $f_c = 300$ GHz (i.e. $\lambda = 1$ mm), and we focus our attention on a cube volume inside the machine of size $L_m = 20\lambda = 0.02$ m, centered in $\mathbf{M} = (M_x, M_y, M_z) = (0, -5, 2)$ m. We assume that UE 1 is fixed in the center of the cube $\mathbf{M}$, so that $\mathbf{s_1} = \mathbf{M}$, while we vary the position of UE 2 anywhere inside the cube, so that it has coordinates $\mathbf{s}_2 = (s_{2,x}, s_{2,y}, s_{2,z})$ with $|s_{2,x} - M_x|, |s_{2,y} - M_y|, |s_{2,z} - M_z| < \frac{L_m}{2}$. We assume that each UE transmits with the same power $p_k = 15$ dBm and a bandwidth $B = 5$ GHz. All the other system parameters are summarized in Tab. 2. We consider the MR, and we calculate the normalized interference gain $|\mathbf{v}_1^\dagger \mathbf{h}_2|^2 / ||\mathbf{v}_1||^2$ where $\mathbf{v}_1$ is computed according to the spherical model.

In Fig. 17a, we present the normalized interference gain as a function of UE 2's position, and we see that the interference gain is not 3 dB lower than its maximum only in a limited volume around UE 1's position. This behaviour indicates that both the UEs are located in the near-field of the receiver, and because of that, we are able to do beamfocusing. Indeed, we have $||\mathbf{s}_1||, ||\mathbf{s}_2|| < \frac{d_{FA}}{10} \approx 40$ m. If the machine was in the far-field of the receiver, it would only be possible to focus the beam on specific directions rather than specific points. Therefore, any region where the interference gain is higher than a certain threshold would theoretically be an infinite cone, without taking the path-loss into account.

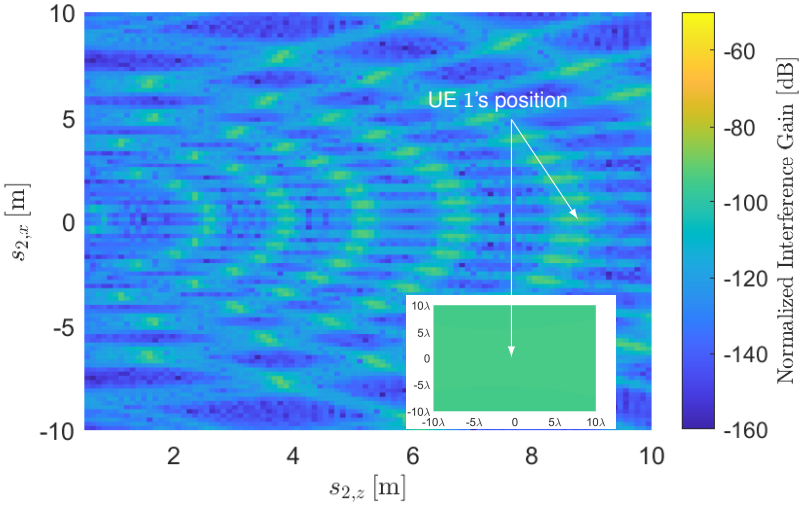

(a) MMSE.

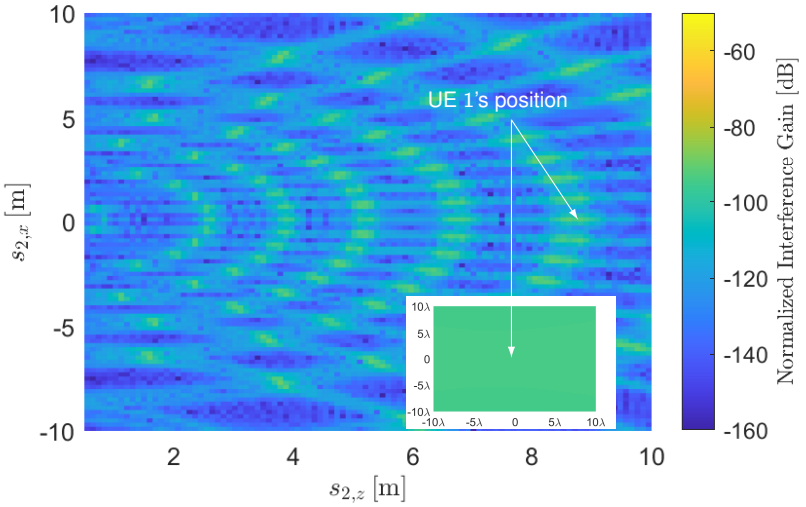

(b) MR .

Figure 18: Interference gain using mismatched (planar) MMSE and MR combiners for a fixed UE 1 *as a function of different locations of an interfering UE* 2*.*

2.6.5 The Impact of a Mismatched Design

Interference Gain: We now analyze the normalized interference gain $|\mathbf{v}_1^\dagger \mathbf{h}_2|^2 / ||\mathbf{v}_1||^2$ where $\mathbf{v}_1$ is computed according to the planar model, with both MMSE and MR. The same scenario described in Sec. 2.6.1 is considered.

Fig. 18 reports the normalized interference gain with the MMSE combiner being used in Fig. 18a, whereas the MR is considered in Fig. 18b. Each figure contains a magnification around UE 1's location, in which the relative distance of UE 2 from UE 1 is measured in wavelengths (for a total span of $10\lambda \times 10\lambda = 1 \times 1\,\text{cm}^2$).

In both Fig. 18a and Fig. 18b, we see that the interference gain is high only in limited space regions, but the size of these regions is significantly larger than in Fig. 13. In fact, since the UEs are not in the far-field of the receiving array, the spherical curvature of the wave front is not negligible on the receiving aperture, and can be exploited to do beamfocusing. However, since the focusing is obtained calculating the combiners with

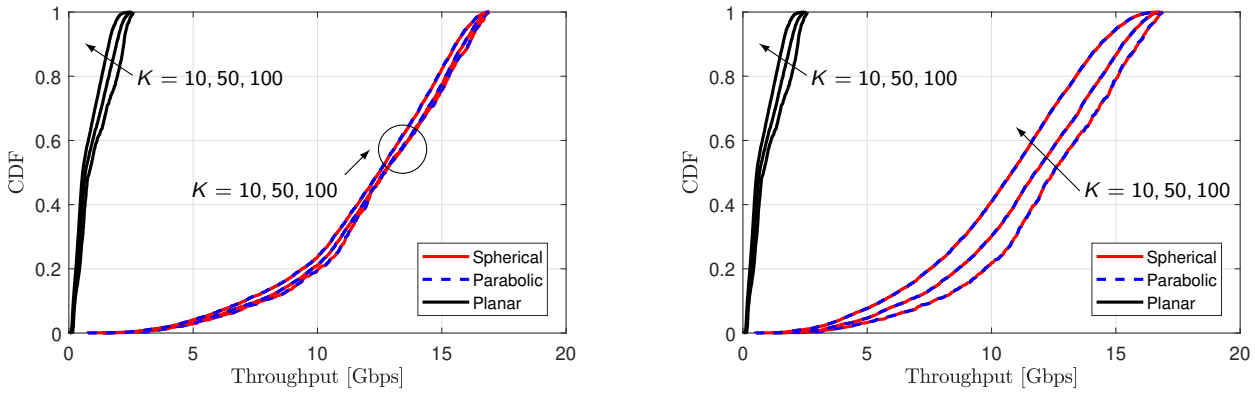

(a) MMSE. *(b) MR.*

Figure 19: CDF of the throughput per UE with $f_c = 300$ GHz, $K = \{10, 50, 100\}$, and both MMSE and MR combiners computed according to the spherical, parabolic and planar models.

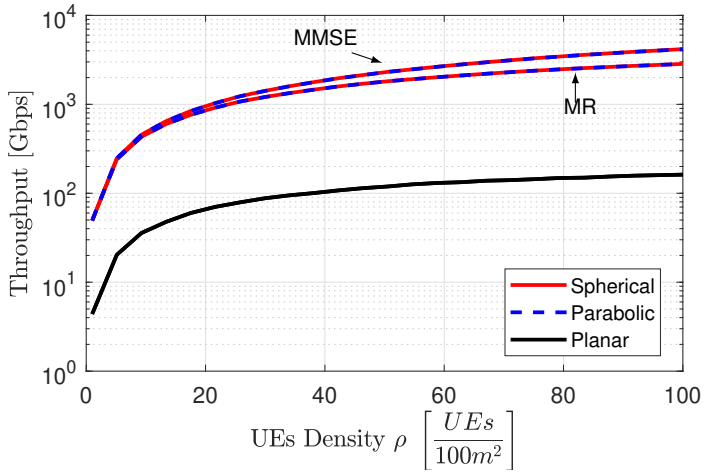

Figure 20: Analysis of aggregate throughput as a function of UEs density with $f_c = 300$ GHz and both MMSE and MR computed according to spherical, parabolic and planar models.

the planar model, the mismatch causes the high interference regions to become significantly larger. More precisely, both the magnifications around UE's 1 position in Fig. 18a and Fig. 18b show that the interference gain is equal to about -90 dB over a span of $10\lambda \times 10\lambda$ around UE's 1 position. We also note that the impact of the mismatch is dominant over the choice of the combiner. In fact, there is no significant difference between MMSE and MR.

Throughput: Let us consider the same scenario described in Sec. 2.6.2. We calculate both the MMSE and MR combiners according to the spherical, parabolic and planar model, and we compare the aggregate throughput to quantify the mismatch impact.

In Fig.19, we report the CDF of Throughput as per (22) with $K = \{10, 50, 100\}$ UEs. We see that if the planar model is used, the mismatch significantly decreases the throughput compared to cases where the spherical or parabolic models are used, regardless of the combiner and the number of UEs. More precisely, we see that none of the UEs achieves a throughput larger than 2.5 Gbps. On the other hand, the parabolic model curves are overlapped to the spherical ones that we already discussed in Fig. 14. In other words, there is no significant impact of the mismatch in our scenario when the parabolic model is used.

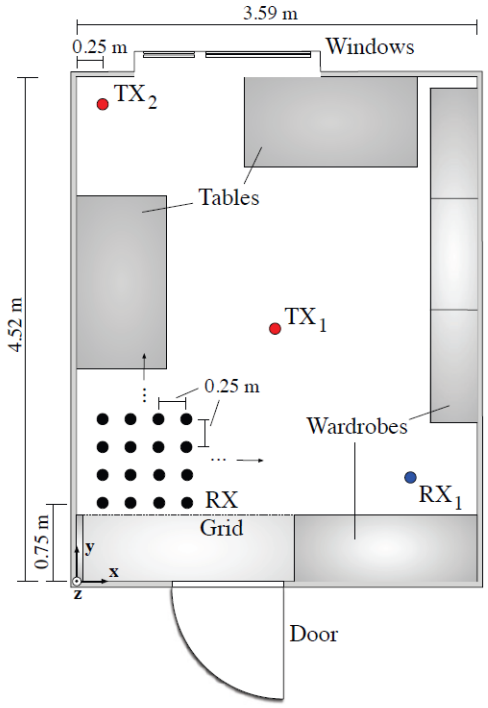

Figure 21: The office scenario [10, Fig. 1].

In Fig. 20, we report the aggregate throughput in (22) as a function of UE's density $\rho \in [1, 100]$ $\left[\frac{UEs}{100m^2}\right]$. We consider both MMSE and MR, and we calculate them according to the spherical, parabolic and planar model to evaluate the mismatch impact. We see that if the planar model is used, the aggregate throughput is significantly lower than using either the parabolic or the spherical ones. More precisely, regardless of the combiner being used and the number of UEs, the aggregate throughput is never larger than 161 Gbps. On the other hand, we find once again that the parabolic model provides the same aggregate throughput as the spherical one, and this aggregate throughput depends on both the combiner being used and the number of UEs as we previously discussed in Sec. 2.6.2.

2.7 Preliminary Results with True Channel Measurements

One of the scenarios of interest for the TIMES project is an office where multiple devices are connected at the same time with an access point mounted under the ceiling [6]. Let us consider the example of this scenario described in [10]. Equipped with several wardrobes and two tables, the setup corresponds to a common use case of a THz WLAN, where an access point mounted under the ceiling supplies radio coverage in the entire room. The room has the dimensions $3.59\,\text{m} \times 4.52\,\text{m} \times 2.82\,\text{m}$. All other lengths can be obtained from the true-to-scale scheme in Fig. 21. The walls and the ceiling are coated with the same plaster, the floor is covered with carpet, the wardrobes as well as the tables consist of different kinds of wood, the windows are made of glass and the door as well as the window frames are metalized. We consider the same receiving array described in Sec. 2.4.1 whose parameters are summarized in Tab. 1, and we assume that its center is located under the ceiling, in the center of the room, so that it has coordinates $(1.795\,\text{m}, 2.26\,\text{m}, 2.72\,\text{m})$. We randomly displace $K = \{2, 8, 16\}$ active UEs in 180 positions equally distributed throughout the room from $x = 0.25\,\text{m}$ and $y = 0.75\,\text{m}$ to $x = 3\,\text{m}$ and $y = 4.25\,\text{m}$ in steps of 25 cm. Representing a handheld nomadic device or a laptop, the UEs are assumed to be at a height of $0.8\,\text{m}$. Each UE transmits with the same power $p_k = 15\,\text{dBm}$. We assume the same hybrid channel model as in [10], which combines the spatial, temporal and frequency

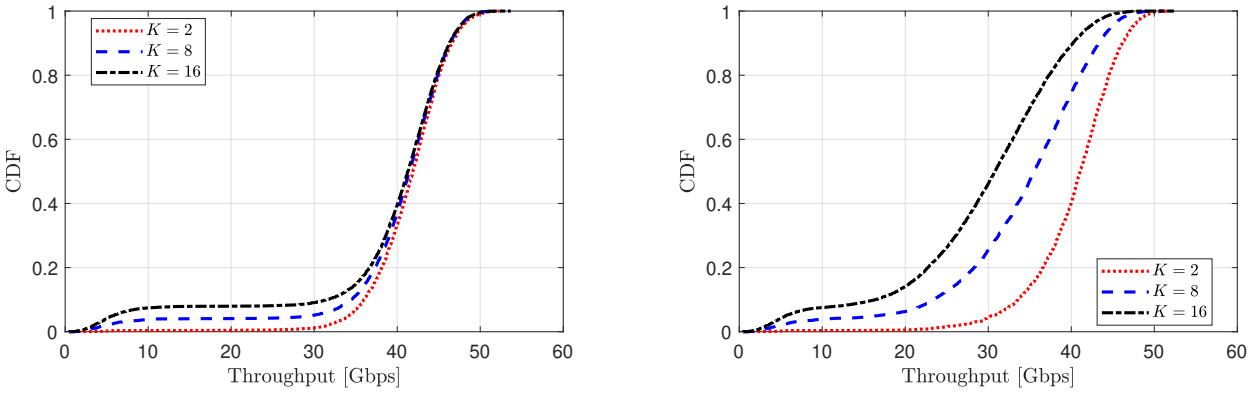

(a) MMSE. *(b) MR.*

Figure 22: CDF of the throughput per UE in an indoor room scenario with $f_c = 300$ GHz, $K = \{2, 8, 16\}$ and both MMSE and MR.

domains. As the basis, a spatial path-specific channel transfer function is defined as

$$H_{i,k}\left(f_c, \phi_{AoD}, \theta_{AoD}, \phi_{AoA}, \theta_{AoA}\right) = a_{i,k} \cdot e^{j\varphi_{i,k}} \cdot D_i(f) \cdot e^{-j2\pi\tau_{i,k}(f-f_c)} \cdot \delta\left(\phi_{AoD} - \phi_{AoD,i,k}\right) \cdot \delta\left(\theta_{AoD} - \theta_{AoD,i,k}\right) \cdot \delta\left(\phi_{AoA} - \phi_{AoA,i,k}\right) \cdot \delta\left(\theta_{AoA} - \theta_{AoA,i,k}\right), \tag{37}$$

which formulates the channel properties of the i-th path of UE k over the frequency f. $a_{i,k}$ specifies the amplitude of the ray at the carrier frequency f_c and $\phi_{i,k}$ is its phase, whereas $\tau_{i,k}$ and $\Phi_{AoA,i,k/AoD,i,k}$, $\theta_{AoA,i,k/AoD,i,k}$ are its time of arrival and Angle of Arrival (AoA)/Angle of Departure (AoD) in the azimuth and elevation, respectively. Furthermore, $e^{-j2\pi\tau_{i,k}(f-f_c)}$ accounts for the frequency-dependent phase rotation on the propagation path. $D_i(f)$ denotes a frequency dispersion function. In the simplest case, rays are subject to a frequency-dependent log-linear increase of their attenuation. All the other details on the computation of $H_{i,k}$ can be found in [10]. Let us now assume the same channel model described in 2.3.2 where the path-loss in (16) is computed as

$$|h_{k,n}| = \beta_k = \sum_{i=1}^{N_{rays,k}} H_{i,k}\left(f_c, \phi_{AoD}, \theta_{AoD}, \phi_{AoA}, \theta_{AoA}\right), \tag{38}$$

where $N_{rays,k}$ denotes the number of paths of UE k, and the all the details about its calculation can be found in [10]. Note that we are considering the path-loss to be the same on the receiving array aperture. Assuming a carrier frequency $f_c = 300$ GHz, a bandwidth $B = 5$ GHz, and a Noise Figure at the receiver $NF = 8$ dB, we calculate the throughput as per (22) for both MMSE and MR combiners. The simulation parameters are summarized in Tab. 1 and 2.

Fig. 22 reports the CDF of the throughput per UE where the MMSE is considered in Fig. 22a, whereas the MR is shown in Fig. 22b. The MMSE is designed to cancel the interference between the UEs, and we can see that it outperforms the MR with the difference being larger with more UEs. Moreover, from Fig. 22a, we observe that the difference in the distribution of the throughput per UE is negligible up to $K = 16$ UEs. More precisely, the throughput is lower than 30 Gbps with a 10% probability, between 30 and 40, Gbps with a 20% probability, between 40 and 45 Gbps with a 40% probability, and between 45 and 50 Gbps with a 20% probability. On the other hand, since the interference is not taken into account by the MR, in Fig. 22b we see that the throughput is significantly lower the more UEs are active. For example, if $K = 16$, the throughput is lower than 20 Gbps with a 15% probability, between 20 and 30 Gbps with a 35% probability, between 30 and 40 Gbps with a 40% probability and between 40 and 50 Gbps with a 10% probability.

Fig. 23 reports the aggregate throughput as per (22) as a function of the number of UEs $K \in [2, 32]$ with both MMSE and MR. We see that the MMSE achieves always larger throughput than the MR, which validates the results shown in Fig. 22. We also observe the throughput grows linearly thanks to the interference between

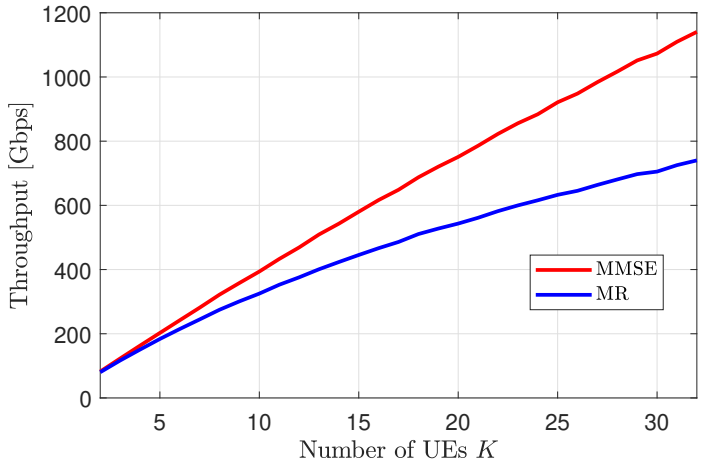

Figure 23: Analysis of the aggregate throughput as a function of the number of UEs K based on a realistic office scenario channel model with $f_c = 300$ GHz.

UEs being cancelled, while the trend is sub-linear with the MR that does not take interference into account. Moreover, the MMSE provides throughput larger than 1 Tbps with $K \geq 27$ UEs, whereas the MR achieves about 750 Gbps with $K = 32$ UEs. It is worth mentioning that $K > 16$ in our office scenario corresponds to $\rho > 1$ UE per m^2, which is practical only in specific applications.

2.8 Fully-Digital vs Hybrid Architectures

In the above sections, the assumption is to consider the unconstrained fully-digital beamformer in order to completely perform signal processing in the baseband. It is known how to perform channel estimation using a fully-digital scheme. However, it requires a dedicated RF chain for each antenna element, leading to a significant increase in the cost and power consumption. The observation of the signals from each antenna element becomes prohibitive, especially when the number of antennas becomes large enough as in Electrically Large Aperture Arrays (ELAAs), in which a huge number of small-sized antennas can be packed in a relatively small unit.

With the aim of reducing the overall complexity while guaranteeing reasonable performance at the same time, hybrid beamformer architectures have been proposed in the literature as a promising alternative to the fully-digital [12]. In a hybrid beamformer, the number of RF chains N_{RF} is lower than the number of antennas N, typically at least equal to the number of streams, which implies that the dimensionality of the digital beamformer is reduced. Fig. 24a and 24c showcase Phase Shifter (PS)-based hybrid beamformers, where the RF chains can be either connected to all the N antennas, *fully-connected*, or a subset of them, referred to as *sub-connected*. The use of analog PSs is convenient due to the low power consumption of the analog components. In the case of a hybrid precoder, the fully-connected and sub-connected analog beamformers care given by:

$$\mathbf{F}_{\text{RF}}^{\text{fully}} = [\mathbf{f}_{\text{RF},1}^{\text{fully}}, \dots, \mathbf{f}_{\text{RF},N_{\text{RF}}}^{\text{fully}}], \tag{39}$$

$$\mathbf{F}_{\text{RF}}^{\text{sub}} = \text{blkdiag}\left([\mathbf{f}_{\text{RF},1}^{\text{sub}}, \dots, \mathbf{f}_{\text{RF},N_{\text{RF}}}^{\text{sub}}]\right), \tag{40}$$

where $\mathbf{f}_{\text{RF},n}^{\text{fully}} \in \mathbb{C}^{N\times 1}$ and $\mathbf{f}_{\text{RF},n}^{\text{sub}} \in \mathbb{C}^{\frac{N}{N_{\text{RF}}}\times 1}$ represents the analog beamformers for the n-th RF chain in the fully-connected and sub-connected architectures, respectively. The operator $\text{blkdiag}\{\cdot\}$ denotes a block diagonal

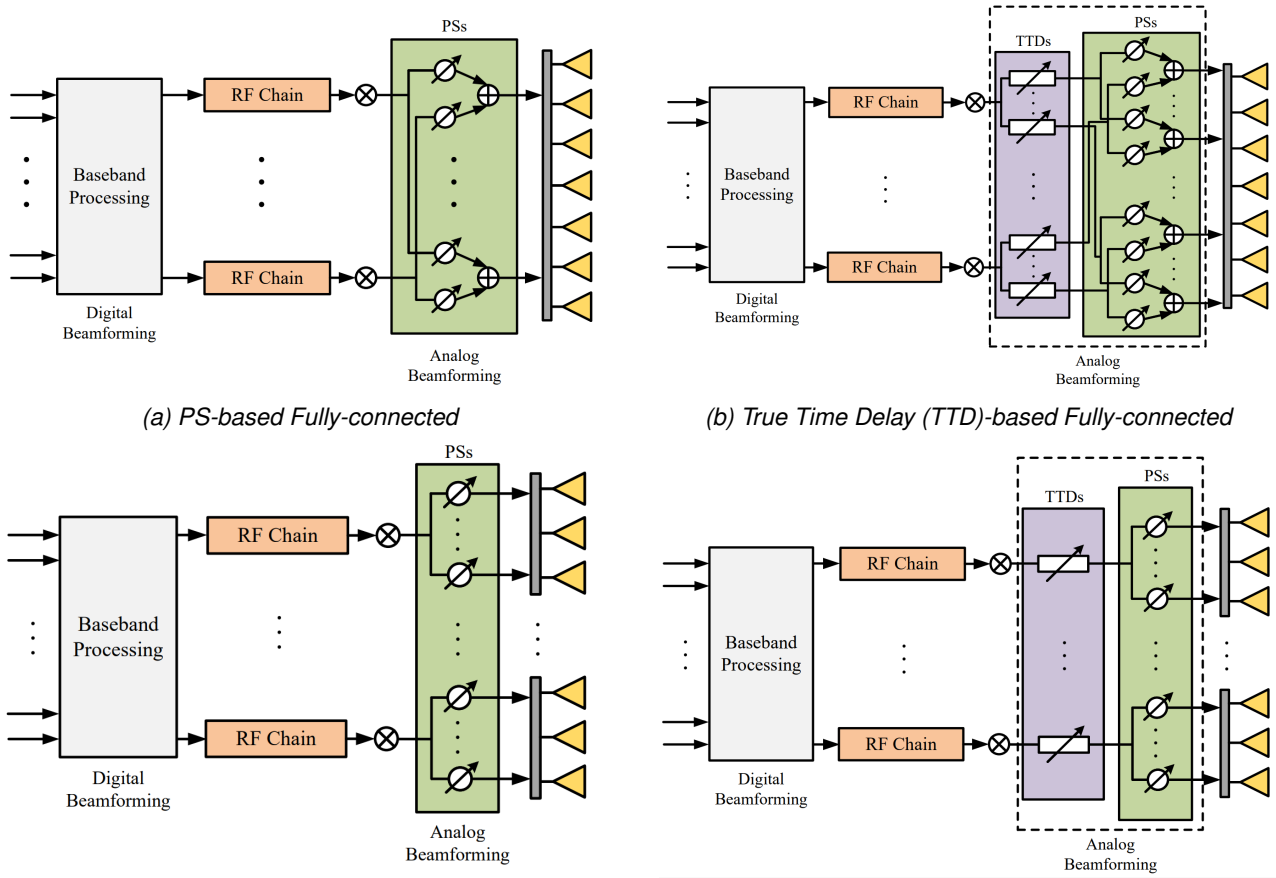

(a) PS-based Fully-connected

(b) True Time Delay (TTD)-based Fully-connected

(c) PS-based Sub-connected

(d) TTD-based Sub-connected

Figure 24: Example of hybrid beamformer architectures [11, Fig. 12].

matrix. The analog beamformers must satisfy the unitary modulus constraint as follows

$$|[\mathbf{f}_{\mathrm{RF},n}^{(\mathrm{full/sub})}]_m| = 1, \forall m, n. \tag{41}$$

It is worth noting that PSs process the incoming signal considering a constant wavelength. However, in wideband systems, this assumption may not hold. TTD have been proposed to mitigate the beam-squint effect in Orthogonal Frequency Division Multiplexing (OFDM) wideband communications. The use of a TTD for each antenna element [13] may produce performance close to the fully-digital scheme. However, the power consumption of TTDs makes them not feasible in real scenarios. Therefore, in Fig. 24b and Fig. 24d *fully-connected* and *sub-connected* TTD-based hybrid beamformers are displayed in order to achieve a trade-off between performance and overall complexity.

In [12], the authors show that assuming perfect Channel State Information (CSI), a hybrid architecture with $2K$ RF chains, where K represents the number of information streams, can achieve the performance close to a fully-digital architecture.

In order to make it feasible in an industrial scenario, the following subsection aims to answer the following question: *is it possible to estimate the near-field channel with a hybrid beamformer in an industrial scenario?*

2.8.1 Channel Estimation in the Near Field with Hybrid Beamformers

In order to achieve the aggregate throughput of 1 Tbps, as explained in Sec. 2.6, different challenges have to be faced. Primarily, in an industrial scenario envisioned in the TIMES project dozens, if not hundreds of moving UEs are expected. Therefore, the system is likely to suffer from pilot contamination, since the number of orthogonal pilots might be lower than the number of UEs. One of the reasons for the limitation in the number of pilots is due to the shortened coherence time at extremely high frequencies, as per the THz band. As a consequence, spatial multiplexing plays a fundamental role in achieving 1 Tbps of aggregate throughput. However, it requires the accurate estimation of CSI to effectively exploit the spatial diversity.

To address this problem, the use of fully-digital architectures becomes prohibitive for ELAAs, as unveiled in section 2.8. On the other hand, merely analog beamforming leads to significant performance loss compared to the fully-digital. This is because there is no such method for channel estimation in the near-field using only analog PSs. Albeit in the far-field region the angular domain is utilized to recover the CSI, in the near-field, where the electromagnetic propagation has different properties, both angular and distance domains need to be taken into account. This section aims to investigate state-of-the-art solutions for the channel estimation problem aided with hybrid beamforming architectures.

The precoder expressions in (20) and (21) assume perfect CSI, which is unattainable in practical scenarios. Consequently, a channel estimation has to be performed. The received SNR is crucial, with higher SNR yielding a more accurate estimation. Typically, at least $\gamma_k \geq 0$ dB $\forall k$ is required to ensure reliable channel recovery. The near-field region offers new opportunities to enhance the performance of wireless communications, such as discriminating different UEs in the distance domain, i.e. beamfocusing. However, it poses several challenges pertaining to channel estimation, especially with an architecture limitation posed by the hybrid beamformer, where the available information to estimate the channel is reduced and the noise might be colored. Furthermore, the far-field assumptions do not hold in the near-field, where the wave front of the propagating signal can not be locally approximated as planar, as discussed in section 2.2. Moreover, in the case of ELAAs, where there are more antenna elements, more and more channel coefficients need to be estimated. In [14], the near-field channel estimation problem is addressed by using a hybrid precoding architecture with $N_{\mathbf{RF}}$ RF chains and N antenna elements. To estimate the near-field channel, each single-antenna UE transmits an orthogonal P-lenght pilot. Since the channel estimation is independent among UEs, the following notation is referred to a given UE k. In particular, for an OFDM communication with M subcarriers, the received pilot sequence at the m-th subcarrier and time slot p is

$$\mathbf{y}_{m,p} = \mathbf{A}_p \mathbf{h}_{m,p} \xi_{m,p} + \mathbf{A}_p \mathbf{n}_{m,p}, \tag{42}$$

where $\mathbf{A}_p \in \mathbb{C}^{N_{\text{RF}} \times N}$ represents the analog combining matrix of the hybrid beamformer, which must satisfy the modulus constraint $|\mathbf{A}_p(i,j)| = 1$, and $\xi_{m,p}$ is the uplink pilot. If we assume $\xi_{m,p} = 1 \; \forall (m,p)$, the received pilot at the m-th subcarrier is denoted as

$$\mathbf{y}_m = \mathbf{A}\mathbf{h}_m + \mathbf{n}_m, \tag{43}$$

where $\mathbf{n}_m = [\mathbf{n}_{m,1}^T \mathbf{A}_1^T, \dots, \mathbf{n}_{m,P}^T \mathbf{A}_P^T]^T \in \mathbb{C}^{PN_{\text{RF}} \times 1}$ represents the combined noise, $\mathbf{A} = [\mathbf{A}_1^T, \dots, \mathbf{A}_P^T]^T \in \mathbb{C}^{PN_{\text{RF}} \times N}$ is the overall combining matrix, and $\mathbf{h}_m \in \mathbb{C}^{N \times 1}$ denotes the channel channel for all the considered time slots. Although the far-field channel is usually sparse in the angular domain, this does not reflect in the near-field region. In fact, electromagnetic propagation has a different behavior in the near-field, making the energy no longer concentrated in one angle, but spread towards multiple angles, namely *energy spread* [14]. Fig. 25 clarifies this by showing the amplitude of the channel in the case of far-field or near-field. It is evident that in the far-field case, the angle domain is sufficient to discriminate the contribution of three different paths. However, if the propagation is in the near-field, relying solely on the angular domain is not enough. To obtain the channel sparsity, both angle and distance domains need to be exploited. As a consequence, far-field-based channel estimation solutions suffer from drastic performance degradation. The LoS near-field channel at the m-th subcarrier, assuming a constant path loss across the antenna elements, can be expressed as

$$\mathbf{h}_m = g e^{-j\frac{2\pi}{\lambda} r} \mathbf{b}(\theta, r), \tag{44}$$

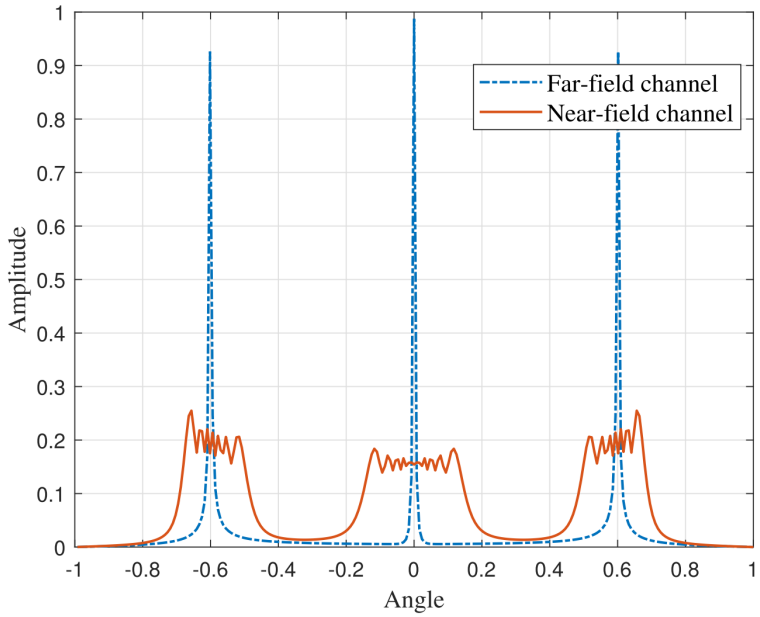

Figure 25: Comparison between the near-field and far-field channels in the angular domain representation [14, Fig. 2].

where g, θ, and r are the complex channel gain, angle, and distance of the LoS path. $\mathbf{b}(\theta, r)$ is the near-field steering vector in the polar domain defined as:

$$\mathbf{b}(\theta, r) = [e^{-jk_c(r^{(0)}-r)}, \dots, e^{-jk_c(r^{(N-1)}-r)}]^T, \tag{45}$$

where $r^{(n)}$ is the distance between a given UE and the n-th antenna, and r denotes the distance of a UE with respect to the origin of the reference system. The near-field channel can be represented according to the polar-domain representation $\mathbf{h}_m^{\mathcal{P}}$ as follows:

$$\mathbf{h}_m = \mathbf{W}\mathbf{h}_m^{\mathcal{P}}, \tag{46}$$

where $\mathbf{W} \in \mathbb{C}^{N \times Q}$ denotes the polar-domain transform matrix, and Q is the number of sampled near-field steering vectors. In Fig. 26b and Fig 26a it is noticeable how the near-field steering vector differs from the far-field one. In particular, the authors in [14] discovered that the angle should be sampled uniformly, and the distance should be sampled non-uniformly to minimize the correlation between different samples, represented by the columns of $\mathbf{W}$. After designing the $\mathbf{W}$ matrix, the compressive sensing-based algorithm in [14] can be used to perform channel estimation assuming a hybrid architecture.

Given the methodologies described in this section, we expect to apply them to estimate the LoS channel in an industrial scenario, where dozens of UEs can be active in the working area and reside in the near-field region of the transmitting ELAAs. With the estimated channel spatial multiplexing can be exploited, aiming to achieve the throughput of 1 Tbps.

2.9 Frequency Dependent Beam Directions

Frequency scanning antennas represent an alternative solution to achieve spatial multiplexing without the need for a complex transceiver architecture. These antennas can either be used to perform a point-to-multipoint communication or to communicate to a single receiver in motion. The concept of a frequency-scanning antenna has been demonstrated in [15] for frequencies around 72 GHz to 79 GHz. In [16], frequency scanning antennas for 230 GHz to 245 GHz has been investigated.

To obtain a frequency scanning antenna, series-fed antenna arrays are used and beam steering is achieved by varying the frequency. This is done by separating the radiating elements by half of the free-space wavelength.

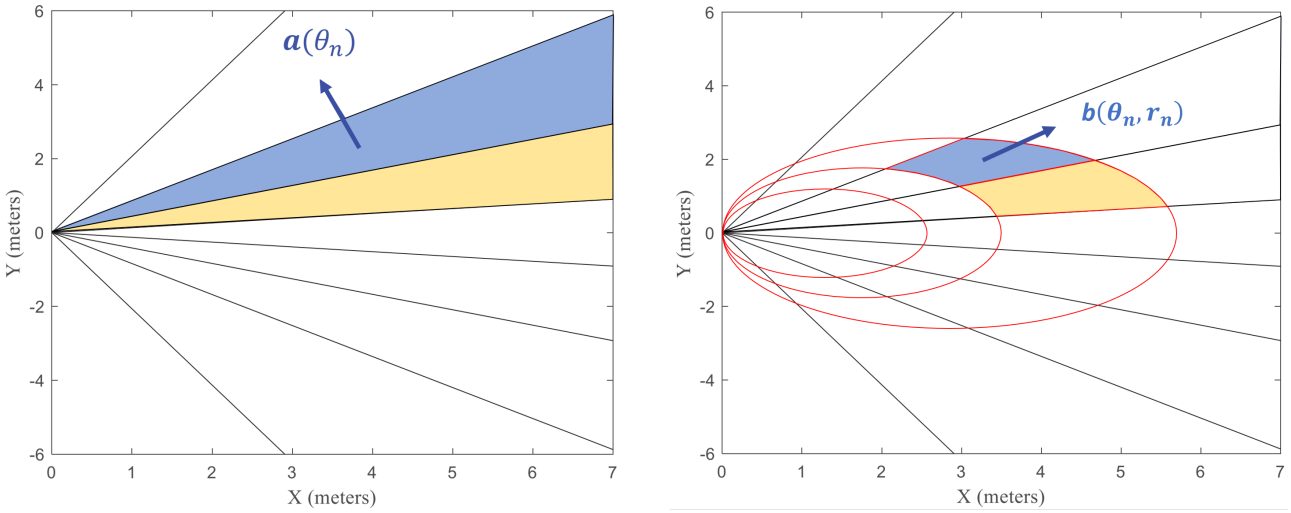

(a) Angular domain. *(b) Polar domain.*

Figure 26: Near-field channel estimation with (a) angular-domain and (b) polar-domain representation.

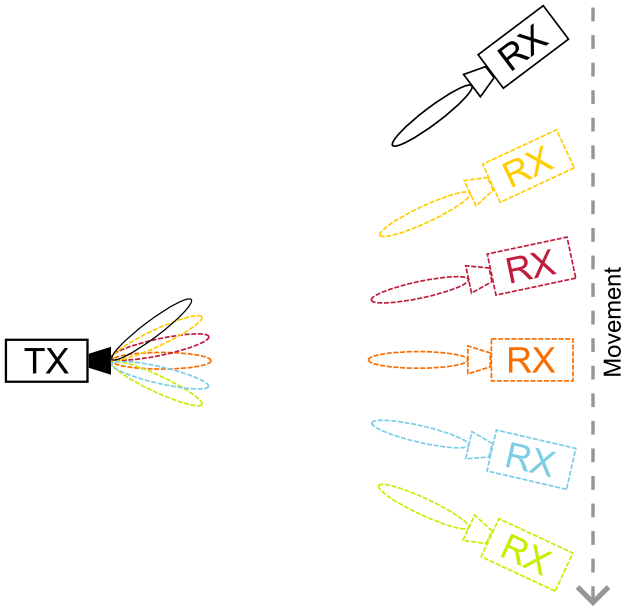

Figure 27: Scenario of a frequency scanning transmitter and a moving receiver

The transmission lines which are connecting the elements have a length proportional to the guided wavelength of the center frequency. Consequently, all elements radiating in phase and the beam are focused at broadside. This leads to a phase shift between the radiating elements at frequencies that differ from the center frequency. As a consequence, the beam is steered away from the broadside direction. To control the sensitivity of steering over the input frequency the length of the transmission lines can be changed [15].

The concept of frequency-scanning antennas will be extended to frequencies around 300 GHz. To perform communication from a transmitter to a single receiver in motion with a frequency-scanning antenna an inter-frequency handover procedure has to be implemented.

In the proof-of-concept that will be developed within the context of this project, the transmission of real-time data will be achieved by means of modems operating in Frequency Division Duplex (FDD) or Time Division

Duplex (TDD) configurations. The use of FDD will require a specific solution to handle the different carrier frequencies in up-link and down-link directions. They will be designed in the context of WP 5, and will have an impact to the handover procedure. The concrete concept will be developed once the details in the RF part are finalized.

Therefore, for the implementation of the handover procedure we will start with the TDD solution, which is based on modems operating according to IEEE Std 802.15.2023 [17, 18]. With TDD, the frequencies for uplink and downlink are the same, so that the antennas behave the same in receive and transmit mode. The modems operate with 2.16 GHz wide channels at a carrier frequency of around 60 GHz, which will be upconverted to 300 GHz. By switching the carrier frequency of those links the scanning angle will be changed, see Fig. 27 yielding the transmission in another beam. In order to perform a handover between the different beams, the received power levels of the connected beam and the neighbouring beam are constantly monitored and if certain conditions are fulfilled a hand-over to the neighbouring beam will be triggered. To showcase this principle, we will perform two levels of demonstrations:

- Simulation-based demonstration: This will be done in a system-level demonstration in SiMoNe enabling the investigation of n different channels and beams. With this simulation, we will be able to study the characteristics of the required Key Performance Indicators (KPI), to determine the principle behaviour of the algorithm, find the best control parameters and investigate the impact of multi path propagation.
- Proof-of-Concept (PoC) by hardware demonstration: TUBS will procure 4 TDD modems enabling to set-up a hardware-based demonstrations for the handover between two beams.

Once the details of the FDD implementation of the antennas are finalized, we will adapt the TDD-handover algorithm to the FDD case. This adaptation will be done in a simulation-based demonstration and a PoC hardware demonstration.

2.10 Remarks

THz communications have the potential to offer much higher data transfer rates compared to traditional RF communication operating up to the millimeter-Wave (mmWave) bands. Antenna arrays play a crucial role in THz communication systems, enabling high beamforming and spatial multiplexing gains. The high spatial multiplexing gain at THz frequencies translates to an increase in the overall throughput of the communication system. By exploiting spatial diversity, THz systems can support a larger number of simultaneous devices, leading to higher data rates and improved spectral efficiency. Despite the encouraging results, we must be aware of the following caveats.

- *Acquiring channel state information*: The analysis was based on perfect knowledge of the propagation channels, which change over time and frequency, and thus must be estimated. The time interval over which the channel maintains constant is known as coherence time T_c, and can be computed according to the following rule of thumb [19]

$$T_c = \frac{\lambda}{4v} \tag{47}$$

  where v is the velocity of the mobile UE. The coherence bandwidth B_c describes the frequency interval over which the channel response is approximately constant. A coherence block consists of a number of subcarriers and time samples over which the channel response can be approximated as constant and flat-fading. Therefore, it can be computed as

$$\tau_c = T_c B_c = \frac{\lambda}{4v} \frac{1}{T_d}. \tag{48}$$

  To estimate the channel, pilot symbols are typically embedded in the transmitted signals. During the coherence block, these known symbols are used at the receiver to infer the channel response. Each user may have a dedicated set of pilot symbols, facilitating separate channel estimation for different users.

From (48), it may appear that the coherence block decreases with increasing frequency (indicating faster channel variation). However, in the context of industrial THz communications systems, which are expected to operate in LoS conditions within relatively compact cell radius and serve slowly moving UEs, the reduction in delay spread and consequent increase in coherence time represent a counteracting effect to the linear scaling with λ. Assuming a carrier frequency of $f_c = 300\,\text{GHz}$ (corresponding to $\lambda = 1\,\text{mm}$), a mobility of $v = 5\,\text{m/s}$, and a channel bandwidth of $B_c = 3\,\text{GHz}$ as described in [20], we obtain a coherence time of $T_c = 50\,\mu\text{s}$ and a coherence block of $\tau_c = 150 \cdot 10^3$ channel uses. This number is sufficient for effective channel estimation and subsequent data transmission, even if a large number of UEs is active.

- *Accurate channel state information*: The beamwidth of an antenna array in the elevation (azimuth) domain is inversely proportional to its normalized vertical height L_V (horizontal width L_H) measured in multiples of the wavelength [19]. For a fixed effective area, L_V and L_H scale linearly with λ, so that the beamwidth is proportional to λ^{-1} [19]. Therefore, although large antenna arrays enable communications at THz due to their high gain, they only do so if the narrow beams are well directed towards the transmitter/receiver, which requires an accurate channel estimation. Moreover, the usage of narrow beams implies that THz communications strongly suffer from the blocking of the LoS path since most other paths depart/arrive at angles, which are not aligned with the beam directions of the arrays. This makes challenging to provide coverage over a large area and to support highly mobile UEs.
- *Hardware implementation*: Antenna arrays must have a dynamically controllable response. This requires a dedicated RF chain per each radiating element (per each subset or radiating element). This design is very challenging with today's technology at very high frequencies, because the size, cost, and power consumption of the required hardware is prohibitive for use in UEs [21–23]. In particular, the Power Amplifiers (PAs) and Digital-to-analog Converters (DACs) / Analog-to-digital Converters (ADCs) are very power consuming at THz (if the bandwidth is increased) and so is the parallel processing of a large number of data streams with billions of samples per second. Therefore, alternative approaches such as analog and hybrid analog-digital beamforming [2] [24] as well as low-resolution DACs / ADCs [25] are subjects of current research.

[2] Analog beamforming introduces phase shifts to the signals going from a single RF chain to the individual radiating elements. Hybrid analog-digital beamforming refers to an antenna array in which each antenna consists of multiple radiating elements whose phases can be individually controlled via analog beamforming.

3 Waveform Design and Tracking for THz-ISAC

THz communication is envisioned as a key technology of next-generation wireless systems due to its ultra-broad bandwidth. One step forward, THz ISAC system can realize both unprecedented data rates and millimeter-level accurate sensing. However, THz-ISAC meets stringent challenges on waveform design to fully exploit the special properties of THz channels and transceivers. In order to enable such integration, the waveform design is crucial as the same waveform will be used for both functionalities. OFDM, which is the waveform employed in LTE and 5G, is considered to be an effective solution. Moreover, OFDM has been also considered for Radar due to its range and velocity resolution [26]. Despite offering several advantages, OFDM suffers from high Peak-to-Average Power Ratio (PAPR) and places high constraints on the RF components and amplifiers, especially in high frequencies where RF amplifiers are not easily implemented, and thus, will cause non-linear distortion and reduce the sensing range. Moreover, low PAPR of the transmit signal is vital for THz transmitters to guarantee effective transmission power and high energy efficiency [27]. Thus, Discrete Fourier Transform (DFT)-s-OFDM with the single-carrier characteristic is more competitive than OFDM for THz communications. To overcome the PAPR issue of OFDM, DFT-s-OFDM has been considered as an effective solution and has also been part for both LTE and 5G systems in the uplink. Unfortunately, the introduction of DFT will affect the sensing accuracy of OFDM. Consequently, a lot of effort has been paid to improve the sensing performance of DFT-s-OFDM. For example, the work in [28] proposed a novel frequency domain spectral shaping technique to enhance the spectral domain of DFT-s-OFDM by adjusting the correlation of signals. However, the communication performance is reduced and the Bit Error Rate (BER) is increased. The work in [29] proposed a framework for chirp-based communications by exploiting DFT-s-OFDM. However, this also led to an increased BER. In the next section, we investigate the potential of DFT-s-OFDM for THz ISAC and propose the design a flexible DFT-s-OFDM waveform that is superior to OFDM. A properly designed waveform for ISAC enables the estimation of certain parameters and attributes of an object, while considering the communication performance as well. However, due to mobility in the environment, the parameters of an object may need to be tracked over time. In fact, another important aspect for enabling ISAC is tracking. The benefit of sensing and tracking is twofold. Firstly, the precise sensing offered by THz technology and tracking applications can increase the safety of the environment by properly detecting in advance uncooperative objects (e.g., forklifts, carts) approaching a machine or worker or entering a restricted area. Secondly, sensing combined with tracking can help increase the reliability of communication links by detecting incoming moving objects/people and predicting potential link obstructions in advance. Furthermore, depending on the dimensions of the target relative to the distance between the target and the sensing receiver, the sensed object can be modeled as a point target or and extended target. In the scenarios defined in the TIMES project, i.e., indoor industrial environments at THz, the far-field assumption may no longer be applicable, and hence, a sensed object may need to be modelled as an extended target. Section 3.2 provides an initial discussion and analysis on the tracking of extended targets for THz ISAC.

3.1 Waveform Design

We propose a multi-block DFT-s-OFDM to find a trade-off between the PAPR and the sensing performance. Simulation results show that the sensing performance can be enhanced at the expense of PAPR for the waveform. To this end, this section provides the following main contributions:

- We propose a flexible multi-block DFT-s-OFDM waveform, where the DFT spreading block stage is divided into multiple DFT spreading blocks. Thus, in turns, we control the frequency response of the waveform.
- We compare the sensing performance of the proposed waveform with plain DFT-s-OFDM and OFDM waveforms.
- Simulation results shows that the proposed waveform offers trade-off between the sensing performance and PAPR.

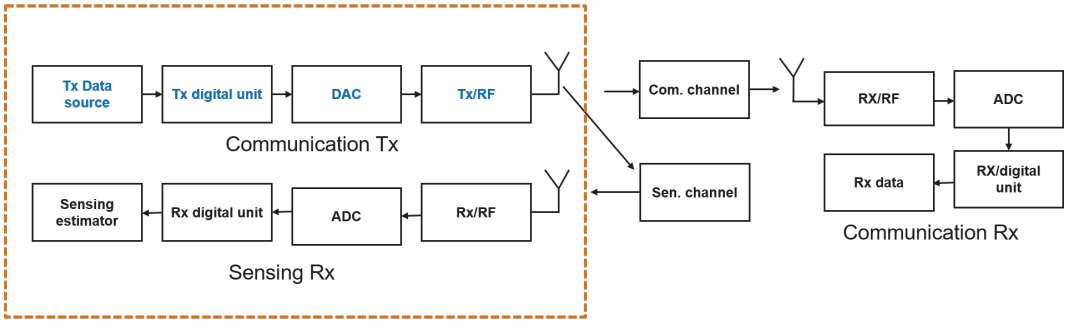

Figure 28: System model for THz-ISAC systems.

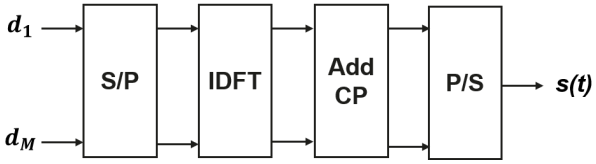

Figure 29: OFDM transmitter.

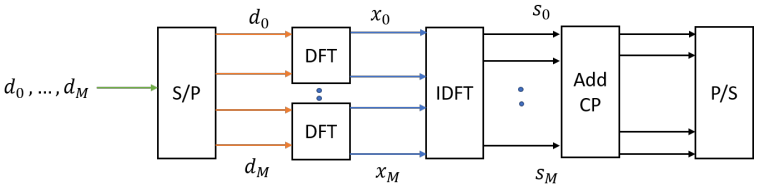

Figure 30: Proposed L blocks DFT-s-OFDM ISAC transmitter.

3.1.1 System Model

Fig. 28 considers a mono-static ISAC system and let $d_m, \forall m = 1, \ldots, M$, denote the data symbols to be transmitted with symbol duration of T s, where the data symbols are independently drawn from the same constellation, e.g., 64-QAM, and M is the total number of data symbols.

We introduce the channel models for THz-ISAC, including a LoS communication channel model and a single target sensing channel model, respectively as follows. On one hand, the Channel Impulse Response (CIR) of the LoS communication channel is [30]

$$h_c(t,\tau) = \alpha_c e^{j2\pi\nu_{\text{LoS}}t}\delta(\tau - \tau_{\text{LoS}}), \tag{49}$$

where $\delta(\cdot)$ denotes the Dirac delta function, α_{LoS} represent the attenuation for the LoS ray, respectively. The propagation delay τ_{LoS} for the LoS ray can be computed by the equations $\tau_{\text{LoS}} = \frac{r_{\text{LoS}}}{c_0}$, where r_{LoS} stands for the LoS path distance and and c_0 is the speed of the light. Meanwhile, the time-varying channel response $h_c(t,\tau)$ is influenced by the Doppler shift ν_{LoS} along the LoS path which are calculated by $\nu = \frac{f_c v}{c_0}$, where v represents the relative speed between the Transmitter (TX) and the Com Receiver (RX) along the corresponding path, f_c refers to the carrier frequency.

On the other hand, the CIR of the single target sensing channel is described as

$$h_s(t,\tau) = \alpha_p e^{j2\pi\nu_p t}\delta(\tau - \tau_p), \tag{50}$$

where α_p is the attenuation. Due to the two-way propagation, the delay and the Doppler shift are calculated by $\tau_p = \frac{2r_p}{c_0}$ and $\nu_p = \frac{2f_c v_p}{c_0}$, where r_p and v_p stand for the range and relative speed, respectively. The speed can be positive or negative, which is determined by the moving direction of the target or the communication receiver.

In the radar sensing channel, a negative speed means that a target is moving away. In the communication channel, a negative speed means that the communication receiver is moving away from the transmitter. The power attenuation of sensing echoes is depends on the Radar Cross Section (RCS) of the sensing target [30, 31].

The Channel Frequency Response (CFR) is given as follows:

$$H_s(m\Delta f, \tau_p) = \alpha_p e^{j2\pi\nu_p m T_o} e^{j2\pi m\Delta f \tau_p}. \tag{51}$$

3.1.2 OFDM Radar

The baseband OFDM time domain signal of one OFDM symbol can be expressed as:

$$x(t) = \sum_{m=0}^{M-1} d_m \exp(j2\pi(m\Delta f)t), \qquad 0 \le t \le T, \tag{52}$$

where M is the total number of sub-carriers, f_c is the centre carrier frequency, and Δf is the sub-carrier spacing. To avoid the interference among different sub-carriers, the orthogonality can be attained using the following condition:

$$\Delta\, f = \frac{1}{T}. \tag{53}$$

Using this condition and consider discrete time system, the discrete time OFDM signal can be written as follows:

$$x(n) = \sum_{m=0}^{M-1} d_m \exp(j2\pi m \frac{1}{T} n \frac{T}{N}), 0 \le n \le N, \tag{54}$$

$$x(n) = \sum_{m=0}^{M-1} d_m \exp(j2\pi \frac{nm}{N}), 0 \le n \le N, \tag{55}$$

Where $M = N$ in order to recover the M transmitted symbols from the received OFDM symbol. Note that (55) represents the Inverse-Fast Fourier Transform (IFFT) operation. We apply IFFT to data symbols d_m to obtain the OFDM symbols with N samples that are transmitted over time sample n. The IFFT is linear operation such that the input and the output are with the same dimension to to be able to recover the signal. Note that, OFDM transmission is normally done using frames with L symbols, assuming l transmitted symbols, OFDM frame is given as follows:

$$x_l(n) = \sum_{l=0}^{L-1} \sum_{m=0}^{M-1} d_{m,l} \exp(j2\pi \frac{nm}{N}), 0 \le n \le N, \forall l. \tag{56}$$

Let us write the OFDM transmission in matrix form as follows, we first consider data symbols in matrix form as $\mathbf{D} \in \mathcal{C}^{M\times L}$. Thus, the transmitted OFDM signal is given as follows:

$$\mathbf{X} = \mathbf{WD}, \tag{57}$$

where $\mathbf{W} \in \mathcal{C}^{M\times M}$ is the inverse DFT matrix where the (n, m) entry is filled with $\exp(j2\pi\frac{nm}{N})$. The received signal at the sensing receiver is given as follows:

$$\mathbf{Y} = \mathbf{HWD} + \mathbf{N}, \tag{58}$$

by using the least square estimator, the estimated channel is given as follows:

$$\tilde{\mathbf{H}} = \mathbf{H} + \mathbf{Z}/\mathbf{X}, \tag{59}$$

After obtaining the estimated channel frequency response $\tilde{\mathbf{H}}$, we use the periodogram method to obtain the Doppler and delay parameters [26].

3.1.3 Performance Evaluation

In this section, we provide various simulation results to illustrate the performance of the proposed DFT-s-OFDM waveform system compared with OFDM and plain DFT-s-OFDM waveforms proposed for ISAC systems. The key parameters include center frequency of 300 GHz, sub-carrier spacing of 1 MHz, M sub-carriers, block size of 256, and 4-QAM modulation.

Fig. 31 shows the Root-Mean-Square Error (RMSE) for target estimation for different waveforms. As can be seen the OFDM waveform offers high accuracy for target estimation compared with the two DFT-s-OFDM variants. However, OFDM suffers from high PAPR. As can be observed the proposed DFT-s-OFDM offers high accuracy compared with the plain DFT-s-OFDM.

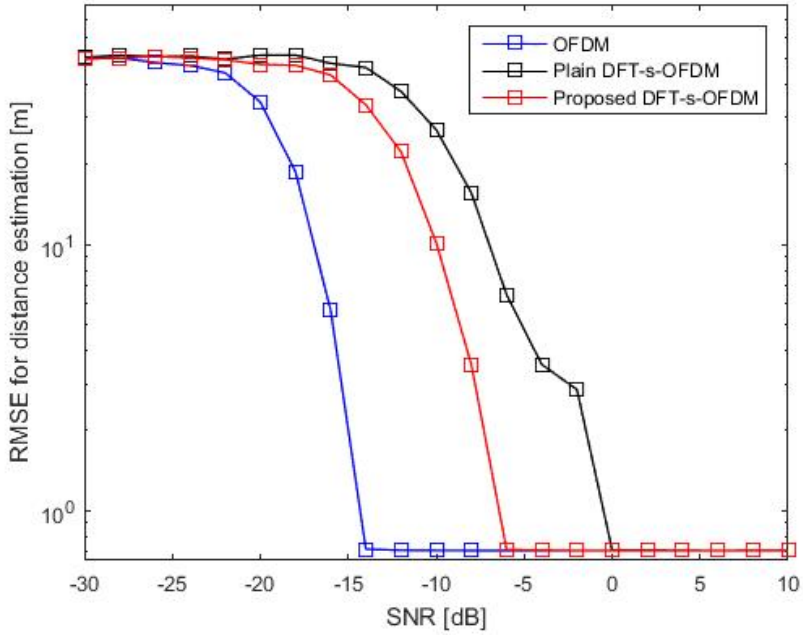

Figure 31: RMSE for target estimation for different waveforms. The target is located at a distance of $d = 100$ meters and its velocity is 80 m/s. Total number of sub-carriers $M = 256$ and the DFT-s block size is 256. Number of DFT-s blocks is 16 for the proposed.

3.2 Tracking of Extended Objects

As mentioned before, tracking can provide increased safety of the environment by properly detecting certain targets. In addition, tracking can also help increase the reliability of communication links, e.g., by predicting potential link obstructions. For what concerns the first scenario, which is depicted in Fig. 32, the exploitation of an ISAC-based system and the tracking capabilities to improve safety in industrial-type environments is particularly interesting for TIMES. Sensing can thus make it possible to detect uncooperative objects (such as carts and forklifts) and obstacles in unwanted areas or workers near machinery, thus enabling the ability to detect them and localize them accurately, together with the possibility of predicting their trajectory in advance, using proper and accurate tracking algorithms. This can allow the implementation of the necessary accident-avoiding countermeasures.

The second scenario, in Fig. 33, concerns the ISAC-enabled sensing-assisted communications for improved THz link reliability. In fact, due to very sharp beams, THz communications likely experience obstructions (by moving objects or simple debris due, e.g., to mechanical processing), causing communication outages. This aspect is extremely detrimental in industrial environments where link reliability and low-latency communications

are necessary to compete with well-established wired systems. Therefore, ISAC-enabled sensing-assisted communication systems, where sensing information is also used to assist the beam management in a communication link, can improve this non-trivial issue.

In particular, sensing and tracking capabilities can be exploited to early detect and locate any passive objects (e.g., robotic harms, people, carts, debris) that can obstruct a communication link. Localization and trajectory prediction in ISAC-enabled sensing-assisted systems coupled with tracking algorithms thus can allow detection of the incoming obstacle in advance, estimate its position and velocity, and, of course, predict its future trajectory evolution a few seconds in advance. This way, a mesh network has enough time to set up a backup link to overcome the obstacle thanks to multi-hop communications or the use of Reconfigurable Intelligent Surface (RIS). This part is crucial to ensure link reliability.

In this section, we focus on tracking and specifically on tracking an extended target. Indeed, at THz and in industrial environments (usually indoors), such as the scenarios defined in the TIMES project, the far-field assumption is no longer valid, and thus, in the near-field, a target cannot be considered point-like.

For this reason, the filtering problem statement at the basis of the tracking algorithm, coupled with the extended target model and a particular possible implementation thereof, are presented in the following subsections.

In particular, a Bayesian approach, based on [32], has been proposed for tracking an extended object in clutter based on two simple axioms:

1. the numbers or received target and clutter measurements in a frame are Poisson distributed (so several measurements may originate from the extended target)
2. the target extent is modeled by a spatial probability distribution and each target-related measurement is an independent 'random draw' from this spatial distribution (convolved with a sensor model).

This model turns out to be especially suitable for a particle filter implementation.

3.2.1 System Model

The target parameters to be estimated are contained in the state vector $\mathbf{X}_k$, where k denotes the time step. The state vector includes the usual target descriptors such as position and velocity together with parameters that specify the spatial extent of the target for the measurement model.

The state vector is assumed to evolve according to a known Markov model: $P(\mathbf{X}_k|\mathbf{X}_{k-1})$.

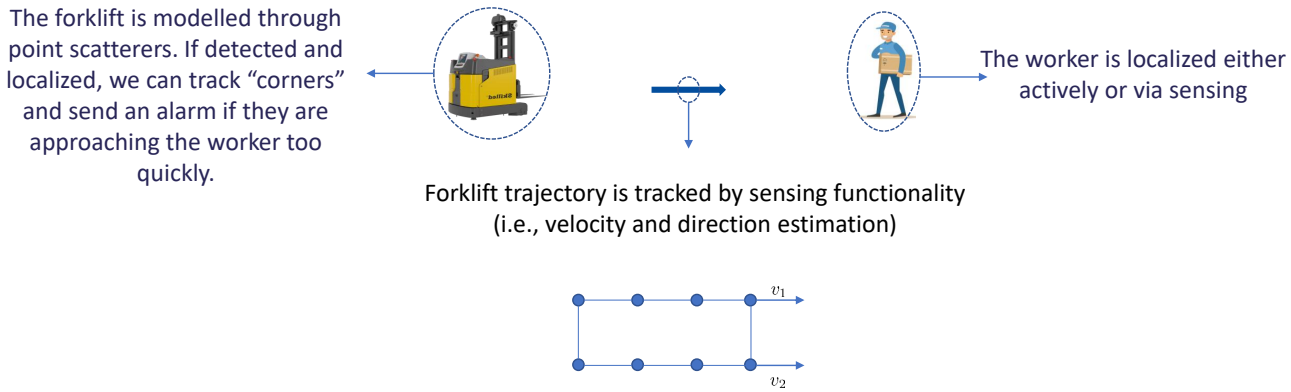

Figure 32: Industrial-type scenario where ISAC-based system and tracking capabilities can be used to improve safety.

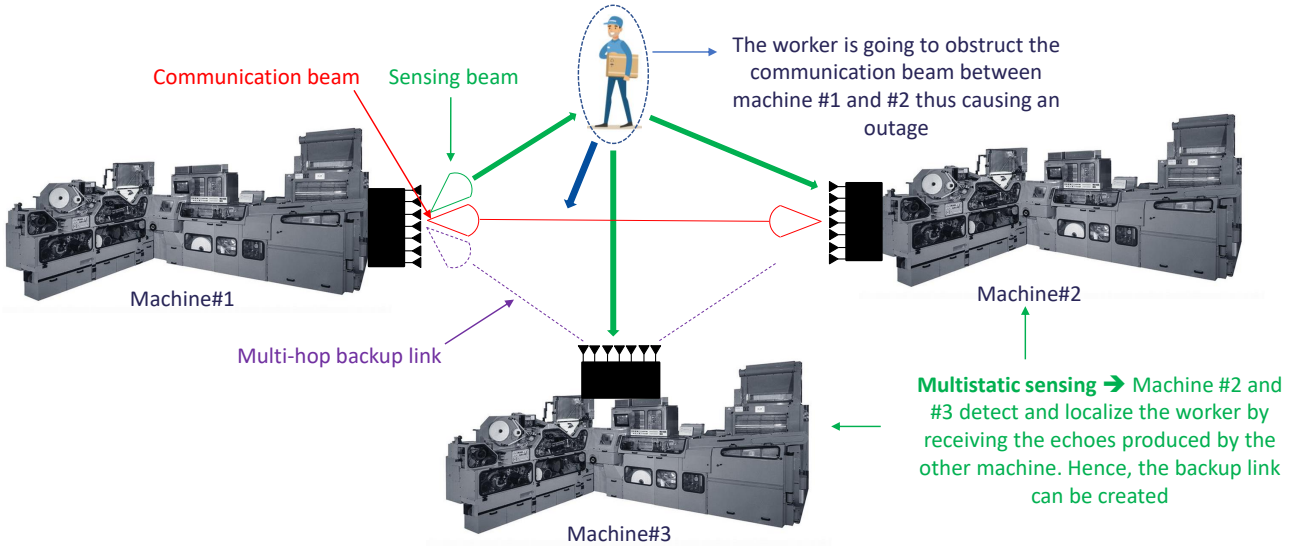

Figure 33: ISAC-enabled and tracking sensing-assisted communications for improved THz link reliability in industrial scenario.

3.2.2 Measurement Model

At each time step k, a frame of n_z sensor measurements $\mathbf{Z}_k = \{\mathbf{z}_1, \cdots, \mathbf{z}_{n_z}\}_k$ becomes available. It is important to note that each of these n_z measurements originates either from random clutter or from the target.

For this reason, we define a mapping $\phi : \{1, \cdots, n_z\} \rightarrow \{0, 1\}$ that assigns each measurement to the target (1) or to clutter (0). It is important to note that ϕ is unknown. In this model, we assume that:

- clutter measurements are independent of the target and distributed according to $P(\mathbf{z}_j|\phi(j) = 0, \mathbf{X}_k) = P_C(\mathbf{z}_j)$, where $P_C(\cdot)$ is known;
- target measurements are distributed according to the spatial extent model: $P(\mathbf{z}_j|\phi(j) = 1, \mathbf{X}_k) = P_T(\mathbf{z}_j|\mathbf{X}_k)$, where $P_T(\cdot)$ is known.

Furthermore, given ϕ and $\mathbf{X}_k$, all measurements in the frame $\mathbf{Z}_k$ are independent, so

$$P(\mathbf{Z}_k|\phi, \mathbf{X}_k) = \prod_{j=1}^{n_z} P(\mathbf{z}_j|\phi(j), \mathbf{X}_k). \tag{60}$$

The number n_T of measurements in the frame that originate from the target is assumed to follow a Poisson distribution with mean λ_T, where this parameter could be an element of the state vector.
Therefore, the probability of n_T target detections per frame is given by

$$P(n_T|\mathbf{X}_k) = \frac{\lambda_T^{n_T}}{n_T!} e^{-\lambda_T}. \tag{61}$$

Likewise, the number n_C of clutter measurements is modeled by a Poisson distribution with mean λ_C, as follows

$$P(n_C|\mathbf{X}_k) = \frac{\lambda_C^{n_C}}{n_C!} e^{-\lambda_C}. \tag{62}$$

In this case, the distribution of the total number n_z of measurements received in a frame is also Poisson with mean $\lambda_T + \lambda_C$

$$P(n_z|\mathbf{X}_k) = \frac{(\lambda_T + \lambda_C)^{n_z}}{n_z!} e^{-(\lambda_T + \lambda_C)}. \tag{63}$$

Note that both λ_T and λ_C are problem specific parameters. They can either be set to predetermined values, or added to the list of parameters to be estimated.

3.2.3 Problem Statement

To complete the problem description, we assume that the prior distribution $P(\mathbf{X}_1)$ of the state vector is available and known at time step $k = 1$.

Given a sequence of measurements $\mathbf{Z}'_k = (\mathbf{Z}_1, \cdots, \mathbf{Z}_k)$ and supposing the motion and measurement model and the prior state distribution as known, the tracking of extended objects problem consists in determining the posterior distribution $P(\mathbf{X}_k|\mathbf{Z}'_k)$.

3.2.4 Formal Bayesian Filter

On the basis of the above model, a general formal Bayesian recursive filter may be derived.

First, we suppose that the posterior Probability Density Function (PDF) $P(\mathbf{X}_{k-1}|\mathbf{Z}'_{k-1})$ at time step $k-1$ is available, where $\mathbf{Z}'_{k-1} = (\mathbf{Z}_1, \cdots, \mathbf{Z}_{k-1})$.
It is required to construct the posterior PDF $P(\mathbf{X}_k|\mathbf{Z}'_k)$ at the following time step k. Moreover, the prior PDF at time k may be obtained from the motion model and the posterior PDF at the previous time step $k-1$ (that are assumed as known), via the Chapman-Kolomogorov equation, as follows

$$P(\mathbf{X}_k|\mathbf{Z}'_{k-1}) = \int P(\mathbf{X}_k|\mathbf{X}_{k-1})P(\mathbf{X}_{k-1}|\mathbf{Z}'_{k-1})d\mathbf{X}_{k-1}. \tag{64}$$

Subsequently, the prior PDF may be updated with information from the latest set of measurements $\mathbf{Z}_k$ via Bayes rule, so that the posterior PDF at time step k can be written as

$$P(\mathbf{X}_k|\mathbf{Z}'_k) \propto P(\mathbf{Z}_k|\mathbf{X}_k)P(\mathbf{X}_k|\mathbf{Z}'_{k-1}). \tag{65}$$

The two relations in (64) and (65) are the general form of the formal Bayesian recursive filter.

Note that in (65), the prior PDF $P(\mathbf{X}_k|\mathbf{Z}'_{k-1})$ at time step k, defined in (64), is assumed as known but the likelihood $P(\mathbf{Z}_k|\mathbf{X}_k)$ must be specified.
Consider the likelihood $P(\mathbf{Z}|\mathbf{X})$, where for convenience the time subscript k has been omitted for the moment. The measurement set $\mathbf{Z}$ implicitly specifies the number n_z of measurements in the frame in addition to the values of the measurements which we denote with $\mathbf{Z}^\dagger$, i.e., $\mathbf{Z} = (\mathbf{Z}^\dagger, n_z)$.

Using the partition of all possible mappings ϕ (for the given n_z), the likelihood may be rewritten as

$$\begin{aligned} P(\mathbf{Z}|\mathbf{X}) &= \sum_{\phi\in\{0,1\}} P(\mathbf{Z}, \phi|\mathbf{X}) \\ &= \sum_{\phi} P(\mathbf{Z}^\dagger|\phi, n_z, \mathbf{X})P(\phi, n_z|\mathbf{X}) \\ &= \sum_{\phi} P(\mathbf{Z}^\dagger|\phi, \mathbf{X})P(\phi, n_z|\mathbf{X}) \end{aligned} \tag{66}$$

where, using the information that the measurements are conditionally independent in (60), $P(\mathbf{Z}^\dagger|\phi, \mathbf{X}) = \prod_{j=1}^{n_z} P(\mathbf{z}_j|\phi(j), \mathbf{X})$.

Now, using the partition of all possible numbers of target measurements, we have

$$\begin{aligned} P(\phi, n_z|\mathbf{X}) &= \sum_{n_T=0}^{n_z} P(\phi, n_z, n_T|\mathbf{X}) \\ &= \sum_{n_T=0}^{n_z} P(\phi|n_z, n_T, \mathbf{X})P(n_z|n_T, \mathbf{X})P(n_T|\mathbf{X}). \end{aligned} \tag{67}$$

For n_T target measurements out of a frame of n_z measurements, there are $n_\phi = \binom{n_z}{n_T} = \frac{n_z!}{n_T!(n_z-n_T)!}$ equally-plausible association mappings; so, if there are n_T measurements associated with the target by ϕ, then

$$P(\phi|n_T, n_z) = \frac{1}{n_\phi} = \frac{n_T!(n_z - n_T)!}{n_z!} \tag{68}$$

else, if ϕ is incompatible with n_T and n_z, $P(\phi|n_T, n_z) = 0$. Note that ϕ is only compatible with one choice of n_T, because there is only one possible value of n_T given a certain function ϕ (that associates a number of 1s equal to n_T). This means that in (67) only one term of the summation is non-zero.

The number n_T of measurements originating from the target is given by the Poisson model in (61) and if n_C is the number of clutter associations, also Poisson distributed, then (62) can be rewritten as

$$P(n_z|n_T, \mathbf{X}) = P(n_C = n_z - n_T|\mathbf{X}) \tag{69}$$

$$= \frac{\lambda_C^{n_z-n_T}}{(n_z - n_T)!} e^{-\lambda_C}. \tag{70}$$

Substitution of (61), (68) and (69) into (67) gives, after cancellation of terms, the following expression

$$P(\phi, n_z|\mathbf{X}) = \frac{1}{n_z!} \lambda_T^{n_T} \lambda_C^{n_z-n_T} e^{-(\lambda_T+\lambda_C)}. \tag{71}$$

The result in (71) together with (60) specifies the likelihood via (66). Thus, the required posterior PDF of the target state in (65), can be rewritten as

$$P(\mathbf{X}_k|\mathbf{Z}'_k) \propto P(\mathbf{X}_k|\mathbf{Z}'_{k-1}) \sum_{\phi\in\{0,1\}} \left(\frac{\lambda_T}{\lambda_C}\right)^{n_T(\phi)} \prod_{j=1}^{n_z} P(\mathbf{z}_j|\phi(j), \mathbf{X}_k) \tag{72}$$

where the time subscript has been restored and the n_T has been written $n_T(\phi)$ to emphasize that ϕ determines n_T.
Therefore, n_T is an unknown parameter because it depends on ϕ that is assumed unknown in Section 3.2.2. Note that if the clutter is uniformly distributed over the sensor Field of View (FOV) with density ρ, then (72) reduces to

$$P(\mathbf{X}_k|\mathbf{Z}'_k) \propto P(\mathbf{X}_k|\mathbf{Z}'_{k-1}) \sum_{\phi\in\{0,1\}} \left(\frac{\lambda_T}{\rho}\right)^{n_T(\phi)} \prod_{j=1,\phi(j)\neq 0}^{n_z} P_T(\mathbf{z}_j|\mathbf{X}_k) \tag{73}$$

where $P_T(\mathbf{z}|\mathbf{X}_k)$ is the PDF of a measurement originating from the target at the time step k, i.e., as we defined above, it is the spatial extent model (supposed as known). The product in (73) should be interpreted as unity for the case $\phi(j) = 0$ for all j (related to clutter measurements).
It can be shown, as proved in [32], that the summation over ϕ in the likelihood may be evaluated to give

$$P(\mathbf{X}_k|\mathbf{Z}'_k) \propto P(\mathbf{X}_k|\mathbf{Z}'_{k-1}) \prod_{j=1}^{n_z} \left(1 + \frac{\lambda_T}{\rho} P_T(\mathbf{z}_j|\mathbf{X}_k)\right) \tag{74}$$

where $P(\mathbf{X}_k|\mathbf{Z}'_{k-1})$ can be obtained via the Chapman-Kolomogorov equation in (64) and it is known because it requires the knowledge of the motion model and the posterior PDF at time $k-1$, which are assumed as known.

We remark that this convenient result is a direct consequence of the Poisson assumptions and it allows the likelihood to be evaluated without constructing association hypotheses, which is especially valuable for a particle filter implementation.

The PDF $P_T(\mathbf{z}|\mathbf{X})$ of measurements originating from the target, also defined as the spatial extent model, depends on:

1. the target model, which describes how measurement sources $\mathbf{Y}$ are distributed in the space over the target. So the PDF of a source $\mathbf{Y}$ given target parameters $\mathbf{X}$ may be written $P(\mathbf{Y}|\mathbf{X})$. This may be viewed as a model of the spatial extent of the target;
2. the measurement error process (or sensor error model) $P(\mathbf{z}|\mathbf{Y})$, which describes the measurement z arising from the source $\mathbf{Y}$, i.e., the measurement values depend only on $\mathbf{Y}$. $P(\mathbf{z}|\mathbf{Y})$ is typically a Gaussian perturbation about a function of $\mathbf{Y}$.

Therefore, the PDF of a measurement $\mathbf{z}_j$ originating from the target is given by the following convolution

$$P_{\mathrm{T}}(\mathbf{z}|\mathbf{X}) = \int P(\mathbf{z}|\mathbf{Y})P(\mathbf{Y}|\mathbf{X})d\mathbf{Y}. \tag{75}$$

There are many possible extended target models, ranging from the classical point-like target (where $P(\mathbf{Y}|\mathbf{X})$ reduces to a delta functional on the relevant components of the state vector) to complex representations of particular target structures. The range includes models corresponding to sets of point sources and more “diffuse" representations. This spatial model could be a bounded distribution such as a uniform PDF or an unbounded distribution such as a Gaussian. It is also possible to model source concentrations via mixture models of the form

$$P(\mathbf{y}|\mathbf{X}) = \sum_{i=1}^{N_{\mathrm{C}}} w_i(\mathbf{X})P_i(\mathbf{y}|\mathbf{X}) \tag{76}$$

where the $w_i(\mathbf{X})$ are positive weights that sum to unity, and N_{C} is the number of the component PDFs $P_i(\mathbf{y}|\mathbf{X})$. Both depend on the target state vector $\mathbf{X}$.
For this mixture model, the probability of a target source originating from component i is $w_i(\mathbf{X})$, and since each measurement is independent, multiple sources may arise from particular components. It is also possible to use negative mixture weights to generate the desired PDF, provided the overall mixture remains non-negative. However, clearly in this case the weights do not have the above physical interpretation. By choosing the spread, location and weight of the mixture components, it is possible to model concentrations of measurement sources in addition to a broad background distribution. The mixture weights can also be tailored according to the target-sensor geometry, for example, for head-on aspects, the forward component of the target model is likely to be dominant.

3.2.5 Proposed Problem Setting

In this subsection, the target and clutter models, and the distributions required for the Bayesian filtering for tracking, derived in Section 3.2.4, are presented for a possible implementation of the filter. Our choices are for a simplified and preliminary version of the tracking system implementation for ISAC, but they seem reasonable and compatible with the scenarios defined in the introduction.

3.2.6 Target Model

In this work, as proposed in [33], the target is modeled as a set of grid elements $\mathcal{P}$ within a designated rectangular region $\mathbf{A} \subset \mathbb{R}^2$ with a fixed size and an area of $|\mathbf{A}|$, as shown in Fig. 34.
At each time step the sensor measurement is made, the extended target is composed of a random number $n_{\mathrm{T}} < |\mathcal{P}|$ of scatterers. Given that each grid element inside $\mathbf{A}$ can be active, i.e., the target scatterer is localized inside that element, with probability q, the number of active points, or target scatterers, follows a binomial distribution, with probability q and number of trials $|\mathcal{P}|$, i.e., $n_{\mathrm{T}} \sim B(q, |\mathcal{P}|)$.

This may seem to be in contrast to the assumption given in Section 3.2.2, where the number of target measurements in a frame is assumed to follow a Poisson distribution with mean λ_{T}.
However, if we consider a finite but very large number of elements on the grid, i.e., $|\mathcal{P}| \to \infty$, each of which is independent active or non-active, the binomial distribution can also be very well approximated by a Poisson distribution, with mean $\lambda_{\mathrm{T}} = q|\mathcal{P}|$.

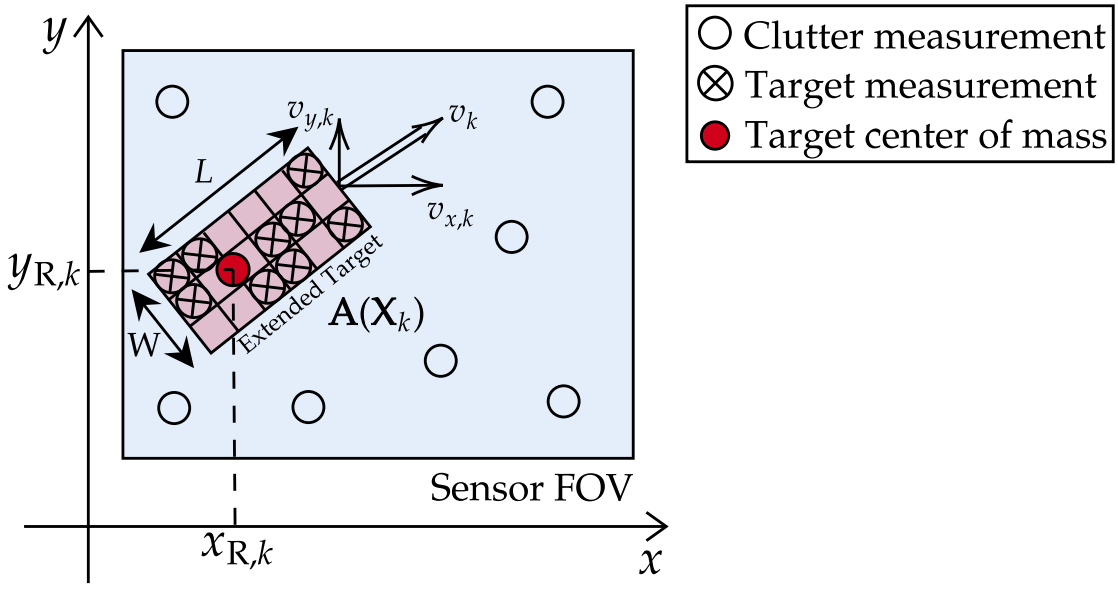

Figure 34: Extended target modeled as a set of scatterers corresponding to grid elements within a rectangular region with fixed size, W and L, and area $\mathbf{A}(\mathbf{X}_k)$. Its center of mass position $(x_{R,k}, y_{R,k})$ and orientation (defined by the velocity component $v_{x,k}$ and $v_{y,k}$) are according to the predicted state vector $\mathbf{X}_k$ at time k. The clutter measurements are assumed to be uniformly distributed on the sensor FOV area.

3.2.7 Clutter Model

A radar sensor not only provides measurements originating from the target object but also from other objects in its FOV, and therefore random clutter occurs. For this reason, a clutter measurement likelihood model is required.
As already stated in Section 3.2.4, clutter measurements are assumed to be uniformly distributed in the sensor FOV area A_{FOV}, with probability

$$P_C(\mathbf{z}_j|\mathbf{X}_k) = \begin{cases} \frac{1}{A_{FOV}} & if \ \ \mathbf{z}_j \in \text{FOV}, \ \phi(j) = 0 \\ 0 & elsewhere \end{cases} . \tag{77}$$

The number of clutter measurements per frame is Poisson distributed with mean $\lambda_C = \rho A_{FOV}$.

3.2.8 Filter Implementation

Based on the proposed target model, the formal Bayesian filter discussed in Section 3.2.4 can be implemented by defining the distributions required in the Bayesian filtering, and the tracking algorithm for the implementation of the filter.

In particular, first we assume that the state vector at a generic time step k is defined as

$$\mathbf{X}_k = [x_{R,k}, y_{R,k}, v_{x,k}, v_{y,k}]^T \tag{78}$$

where $x_{R,k}$ and $y_{R,k}$ are the cartesian coordinates of the extended target center of mass, while $v_{x,k}$ and $v_{y,k}$ are the target velocity components.
The generic sensor measurement j, within the measurement frame $\mathbf{Z}_k$ available at time step k, originating from either the target or the clutter, can be represented by the following vector

$$\mathbf{z}_j = [x_{j,k}, y_{j,k}] \tag{79}$$

where $x_{j,k}$ and $y_{j,k}$ are the cartesian coordinates of the scatterer j estimated by the sensor at time step k.

To this point, based on the proposed target and clutter models, and the considered Bayesian filter, the distributions required for the Bayesian estimation of the state vector parameters, are listed below.

- **Prior state distribution**:
$$P(\mathbf{X}_1) \sim \mathcal{N}(\boldsymbol{\mu}_0, \mathbf{Q}_0) \tag{80}$$
where $\boldsymbol{\mu}_0 = [x_{R,0}, y_{R,0}, v_{x,0}, v_{y,0}]$ and $\mathbf{C}_0 = diag(\sigma^2_{x,0}, \sigma^2_{y,0}, \sigma^2_{v_{x,0}}, \sigma^2_{v_{y,0}})$.
- **Motion model**:
$$P(\mathbf{X}_k|\mathbf{X}_{k-1}) \sim \mathcal{N}(\mathbf{A}_{k-1}\mathbf{X}_{k-1}, \mathbf{Q}_{k-1}) \tag{81}$$
where, by assuming a linear motion model with zero-mean Gaussian process noise and small update time interval T_{update}, $\mathbf{X}_{k-1}$ is the state vector estimated at the time step $k-1$, $\mathbf{Q}_{k-1}$ is the covariance matrix of the process noise and $\mathbf{A}_{k-1}$ is the transition matrix of the constant velocity motion model, defined as
$$\mathbf{A}_{k-1} = \begin{bmatrix} \mathbf{I}_n & T_{\text{update}}\mathbf{I}_n \\ \mathbf{0}_n & \mathbf{I}_n \end{bmatrix} \tag{82}$$
where n is the spatial dimension of the problem, in this case set to $n = 2$.
A simple but reasonable way to define the process noise covariance matrix is to set $\mathbf{Q}_{k-1} = \alpha T_{\text{update}}\mathbf{I}_n$, where α is the constant motion uncertainty coefficient.
- **Prior density**:
$$P(\mathbf{X}_k|\mathbf{Z}'_{k-1}) = \int P(\mathbf{X}_k|\mathbf{X}_{k-1})P(\mathbf{X}_{k-1}|\mathbf{Z}'_{k-1})d\mathbf{X}_{k-1} \tag{83}$$
evaluated through the Chapman-Kolomogorov equation, as stated in Section 3.2.4.
- **Posterior density**:
$$P(\mathbf{X}_k|\mathbf{Z}'_k) \propto P(\mathbf{X}_k|\mathbf{Z}'_{k-1}) \prod_{j=1}^{n_z} \left(1 + \frac{q|\mathcal{P}|}{\rho} P_{\mathrm{T}}(\mathbf{z}_j|\mathbf{X}_k)\right) \tag{84}$$
where the proposed extended target measurement likelihood is given by
$$P_{\mathrm{T}}(\mathbf{z}_j|\mathbf{X}_k) \sim \begin{cases} \mathcal{N}(\mathbf{z}_j, \mathbf{C}_j) & if \;\; \mathbf{z}_j \in \mathbf{A}(\mathbf{X}_k) \\ 0 & elsewhere \end{cases} \tag{85}$$
where $\mathbf{X}_k$ is the predicted state vector at time step k evaluated through the motion model, $\mathbf{A}(\mathbf{X}_k)$ is the rectangular target area $\mathbf{A}$, according to the predicted state vector $\mathbf{X}_k$, and $\mathbf{C}_j = diag(\sigma^2_{x,j}, \sigma^2_{y,j})$, where $\sigma^2_{x,j}$ and $\sigma^2_{y,j}$ are the variances of the position coordinates of the scatterer j, which are related to the measurement uncertainty along the two cartesian coordinates, depending on the sensor range resolution.
According to this model, it can be observed that the product in the posterior density expression is the product of equally weighted Gaussians with different mean vectors, corresponding to the estimated position coordinates of the associated scatterers. If we assume that each of these has the same covariance matrix $\mathbf{C}$, the resulting distribution is also Gaussian with the same weight and covariance matrix $\mathbf{C}$, but having a mean vector composed of the coordinates of the barycenter of the estimated target scatterer position, according to the predicted state vector at time k, i.e., for $\mathbf{z}_j \in \mathbf{A}(\mathbf{X}_k)$.

For what concerns the tracking algorithm necessary to obtain the estimation of the state vector, starting from the posterior density, the proposed model turns out to be particularly suitable for a particle filter implementation, as already remarked at the end of Section 3.2.4, which will be the subject of future work.

4 Analysis and Mitigation of Hardware Impairments

The proper characterization of wireless transceivers is essential for the development of THz systems capable of delivering high-performing sensing and communication services. Indeed, undesired effects arising from imperfection in the RF components of wireless devices can negatively impact the system performance if not properly handled. Typically, the severity of these impairments is more pronounced with increasing operating frequency and bandwidth, hence their characterization and mitigation is even more important when targeting THz bands. To this aim, it is important to analyze the transceiver architecture, isolate the sources of impairments, and evaluate their contributions individually.

In this section, we introduce the transceiver architecture adopted in this project and identify potential impairments that may influence its behavior. Then, we describe each contributing impairment and quantify their effect by means of measurements on real RF hardware components. Finally, we analyze the impact that these impairments have on the performance of an OFDM system operating at THz frequencies and propose possible mitigation techniques. We must stress that the design of the THz frontends is being carried out as part of WP 5 and is not yet finalized. Therefore, the analysis presented in this section is based on preliminary RF designs which however well represent the behavior of the final system.

4.1 THz Transceivers Architectures

Different architectures can be used to realize wireless transceivers operating at THz frequencies. A popular choice is the direct-conversion (or zero-Intermediate Frequency (IF)) architecture. The popularity of this approach stems from the simplicity of its implementation and on-chip integration. The basic principle of operation consists in directly converting the signal from baseband to the RF carrier and vice-versa. Although this architecture eliminates the need to have high-Q image reject and bandpass channel selection filters, thus facilitating complete monolithic integration, at such high frequencies it is prone to Direct Current (DC) offsets and I/Q imbalance problems [34]. Another possible solution to operate at THz and sub-THz frequency bands is the super-heterodyne architecture, where up/down-conversion is carried out in two stages through an intermediate frequency. This approach is widely adopted due to its immunity to DC offsets and high selectivity gains. However, in the process of down-converting the signal from pass-band to IF, the image-frequency problem arises, thus requiring an image rejection filter that precedes down-conversion. This issue complicates on-chip integration and makes the receiver less flexible in terms of frequency tuning.

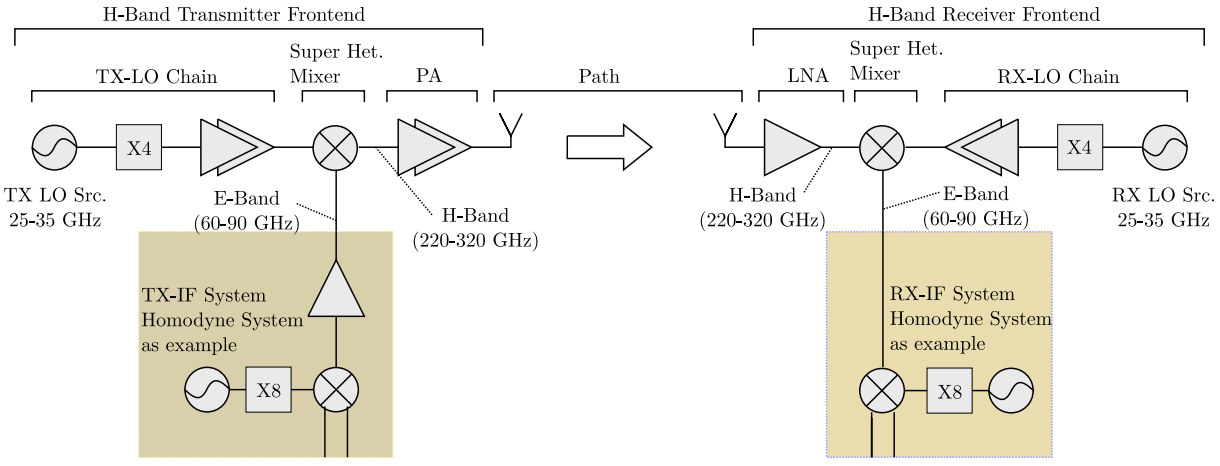

Figure 35: Planned H-band superheterodyne H-band system architecture with additional IF-system.

In this project, a robust super-heterodyne transceiver is selected over the less performing zero-IF architecture. Fig. 35 gives an overview of the RF system. The individual impairments are introduced based on the block diagram and described in more detail in the following subsections. The contribution are divided in

- Phase noise: Phase Noise results in random phase changes in RF-signals. Phase noise is inserted in different parts of the RF-System. It can origin from the signal generation (IF-System) or primarly in the Local Oscillator (LO)-generation of the H-band or IF-system. In non-coherent systems the phase noise contributions adds up and frequency multiplications also amplify phase noise.
- Power Amplifier Non-Linearities: Generally all semiconductor based components of the RF-system can act non-linear when driven in certain operation points. However, the frontend system design can avoid compression of most other devices by adequate gain-partitioning. Soley the PA is deliberately driven in compression to obtain optimal output-power. So non-linear behaviour in system simulation of the power amplifier is of most interest in link-level simulations.
- Beam-squinting: When antenna arrays are used, beamforming is applied to ensure high SNR ratio at THz frequencies. Accurate beamforming that results in high antenna gains requires a large number of antenna elements. Moreover, the availability of large chunks of spectrum at the THz band implies the possibility to adopt very large bandwidths. The combination of the adoption of very large bandwidths and large number of antenna elements results in a significant propagation delay across the antenna, thus creating the beam-squinting phenomenon [13]. Since beam-squinting can be mitigated by adjusting the phase-shifters of the transceiver, implying that it is a result of inadequate phase-shifts, they will be discussed in this chapter.
- LO-Chain Harmonics: Because of technical difficulties producing high quality and high power carriers at mmWave or sub-mmWave frequencies electronically, carriers are often generated in lower frequency domains and multiplied in the frontends using higher order harmonics. As shown in the Fig. 35, amplifier circuits can cope with conversion losses of these analog multiplications. With generation of harmonics, other orders of the wanted harmonics are produced inherently and the suppression of them is limited using filter and matching networks but unwanted harmonics can not be cancelled completely. This may apply in the given setup in Fig. 35 to the LO-carrier and the carrier of the IF-signal, producing even more intermodulation products through their multiplication in the mixer stage.
- Frequency response: All components shown in the systems block diagram have a non-flat frequency response. This originates from various sources, but some reasons are mounting techniques, ohmic losses, reactance in filter and matching networks which are employed between every circuit.
- Additive White Gaussian Noise (AWGN) Contribution: Thermal noise has high influence on the signal quality and is defined often by the additive white Gaussian noise. This is mainly dependent on the antenna performance, the wireless channel, free space path loss, antenna temperature and the noise figure of the Low Noise Amplifier (LNA). As these dependencies are not covered by this deliverable, we point to deliverable 2.4, which covers the link-budget calculations.

Most of the following quantification of the RF impairments are based on measurements on existing/preliminary RF hardware. One front-end generation used mostly for the IF-system is the hardware, reported in [35] and [36]. H-band measurements are conducted with the superheterodyne chipset from the ThoR project, in the following referred to as "ThoR frontend", reported in [37].

4.2 Phase Noise

The phase noise refers to random low-frequency deviations of the phase and/or frequency of an RF-Signal. Mostly phase noise is the frequency domain expression, whereas in time domain it is often referred as phase jitter. Phase noise adds random phase deviation to the RF-signal decreasing signal quality.

$$a(t) = A * \cos\Big(\omega t + \phi(t)\Big) \tag{86}$$

Equation 86 gives a time domain representation of the phase noise, whereas $\phi(t)$ represents the random deviation of the signals' phase. However, phase noise is quantified mostly in dBc/Hz at a given offset frequency using spectrum-analyzer-based techniques. Because of the wireless transmission, the carrier generation in the sender and the corresponding receiver are non-coherent. In conclusion, the random phase variations are not

correlated and thus the phase noise contribution adds up in a first-order approximation. This behavior is shown in Fig. 36 where different measurements are reported: with the low-Phase Noise (PN) Dielectric Resonator Oscillator (DRO), the PN-influence does not show. If the RX-carrier generation is replaced by a higher-PN Phase Locked Loop (PLL), then the influence becomes visible. When the TX-carrier is also generated by a PLL, the PN-influence nearly doubles, showing the additive PN-behaviour of non-coherent PN-contributions.

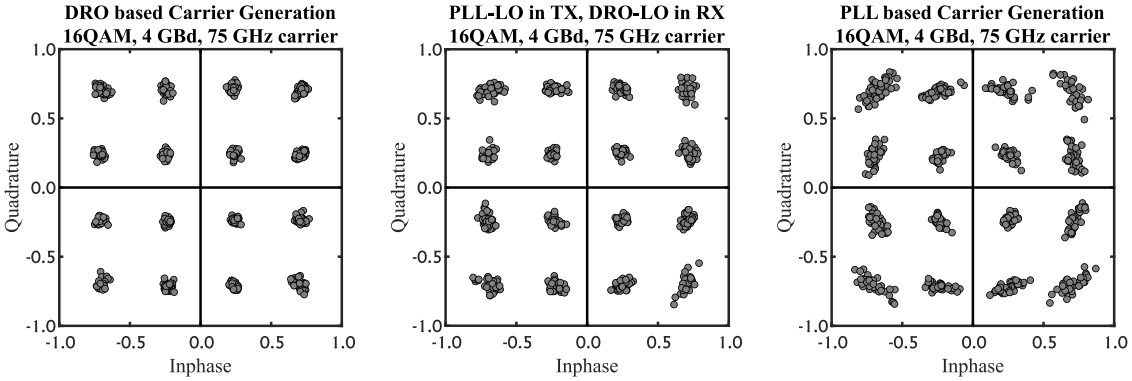

Figure 36: Comparison of single carrier 16 QAM signal with Elipse-HW with different carrier generation methods. Left plot is DRO-based carrier generation and the right plot shows PLL-based carrier generation. The middle plot shows a measurement were RX and TX carriers had been generated differently.

This also shows: the phase noise is dependant on the oscillator technology and its implementation: In this section three signal generation techniques are discussed, compared and the results quantified.

High spectral purity and low phase noise can be achieved using photonic mixing of two narrowly spaced laser sources. This technology yields good carrier quality, the frequency is tunable by changing the spacing of the laser lines. However, the system is bulky and not yet economically feasible for low-cost implementations, like to ones targeted in TIMES. Another technique is DRO, which are based on resonators, build of an enclosed metallic tubes, which is filled by an dielectric material. These oscillators have excellent phase noise and quality factor compared to other electronic oscillators, but can not be tuned or just be mechanically tuned in frequency. Another commonly used option is the usage of PLL. This technology relies on voltage controlled oscillators which are stabilized by an phase control loop. This reduces the low frequency phase noise but compared to DRO the overall phase noise is increased. For many scenarios in TIMES-project, an adjustable LO-frequency is needed. For instance in use-cases using frequency selective leaky-wave antennas, the direction of arrival can be tuned, by tuning the center frequency of the RF-Signal. Conclusively the usage of a PLL-based carrier generation will be probable in the TIMES use-cases.
In the following the three mentioned techniques are compared by their phase noise. Table 3 gives an overview and a comparison of band of operation and output power. To compare the different techniques at around 240 GHz, a multiplication factor has to be considered. It is indicated, that additional multiplier stages are inherently increasing the phase noise contribution. Using ideal frequency multipliers, the phase noise increased by $20log(N)dB$, with N being the multiplication factor.

Fig. 37 gives an comparison of the three techniques over the offset frequency. The phase noise generated by the device them self is plotted by the dashed line. Considering the multiplication factors for 240 GHz, the behaviour is shifted in y-axis. It is observed, that although the high multiplication factor of 24, the DRO has almost the best phase noise behaviour. The PLL suppresses the low frequency phase noise better than the alternatives but has an higher overall phase noise towards the higher offset frequencies.

Table 3: Comparison of phase noise for different LO generation techniques.

Oscillator	Frequency range	Output power	Phase Noise at 1 MHz	THz Phase Noise* at 1 MHz	Src
Photonic LO (CNRS)	68 GHz - 82 GHz	>10 dBm	-110 dBc/Hz	-99 dBc/Hz	[38]
DRO (COTS)	10.43 GHz	1 dBm	-140 dBc/Hz	-113 dBc/Hz	[39]
PLL (IAF)	25 GHz - 33.75 GHz	5 dBm	-110 dBc/Hz	-92 dBc/Hz	[40]

*corrected phase noise with ideal frequency multiplication towards H-band.

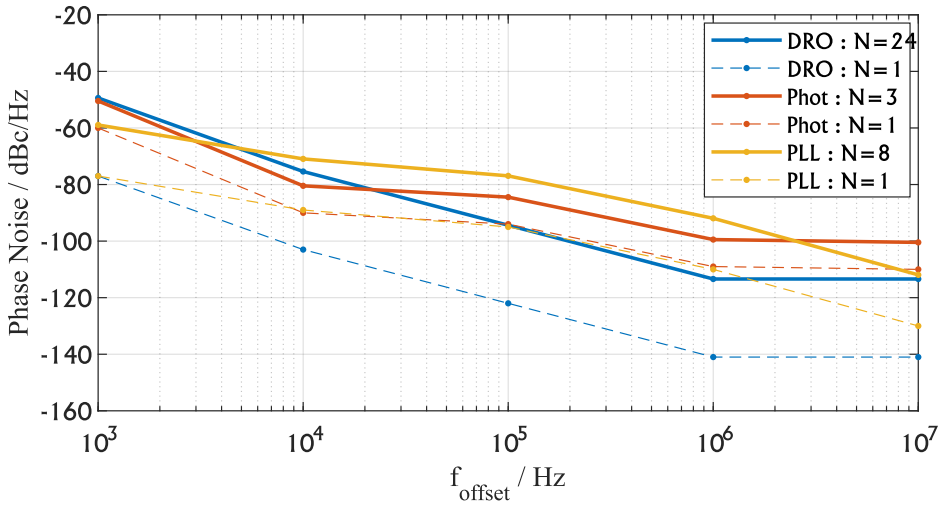

Figure 37: Phase noise performance of different carrier generation technologies vs. offset frequency.

4.3 Power Amplifier Non-Linearities

At THz frequencies, PA non-linearities becomes a crucial aspect to consider. This is mainly due to the limitation on the linear range of operation as manufacturing efficient off-the-shelf PAs may be challenging at THz frequencies when compared to lower ones, and thus the impact of distortions on an adopted waveform and modulation order must be taken into account in link-level simulations. Additionally, it is important to have a PA non-linearity model to understand the impact it has on transmit power dynamics when adopting a certain waveform given the severe propagation loss in the THz range, and on the spectral spread and interference characteristics in the case of the presence of adjacent channels in the network.

PA-non-linearity models can be classified into three categories [41, Fig. 1]:

- Memory-less non-linearity models: behavioral models characterizing the non-linear Amplitude-to-Amplitude (AM-AM) distortion as a function power.
- Quasi-memory-less non-linearity models: behavioral models characterizing the non-linear AM-AM and Amplitude-to-Phase (AM-PM) distortion functions.
- Non-linearity models with memory: behavioral models considering the non-static distortions that depend on the past input levels, modeled through non-linear transfer functions (Volterra kernels).

To model PA non-linearity effect, we adopt a similar approach to that in [42], which promotes the quasi-memoryless Rapp model proposed in [43] to realize the AM-AM and AM-PM distortion relations. The AM-AM

($F_{AM-AM}(x)$) and AM-PM (($F_{AM-PM}(x)$)) distortions may be realized by applying

$$F_{AM-AM}(x) = \frac{Gx}{(1+|\frac{Gx}{V_{sat}}|^{2p})^{(\frac{1}{2p})}}, \tag{87}$$

$$F_{AM-PM}(x) = \frac{(Ax^q)}{(1+|\frac{x}{B}|^q)^q}, \tag{88}$$

where G represents the small signal gain, p denotes the smoothness factor, V_{Sat} is the saturation voltage coefficient and the coefficients A, B, q are AM-PM distortion curve parameters.

Since the operating frequency of the model proposed in 3rd Generation Partnership Project (3GPP) belongs to the 30 to 70 GHz range, the AM-AM and AM-PM distortion parameters may have to be changed. We hence use the derived parameters from the study in [44], where the authors propose AM-AM distortion parameters based on a survey on the PA performances at the D-band (110 to 170 GHz). The suggested parameters are as follows: $G = 13.59$, $V_{sat} = 1.35$ and $p = 1.41$. Since there is lack of data in the literature regarding the AM-PM distortion, the parameters adopted by 3GPP can be used as a starting point in this project, which propose $A = -345$, $B = 0.17$ and $q = 4$. Figures 38 and 39 depict the AM-AM and AM-PM distortions as a function of the input power P_{in} for the proposed Rapp parameters in [42] and 3GPP in [44], respectively.

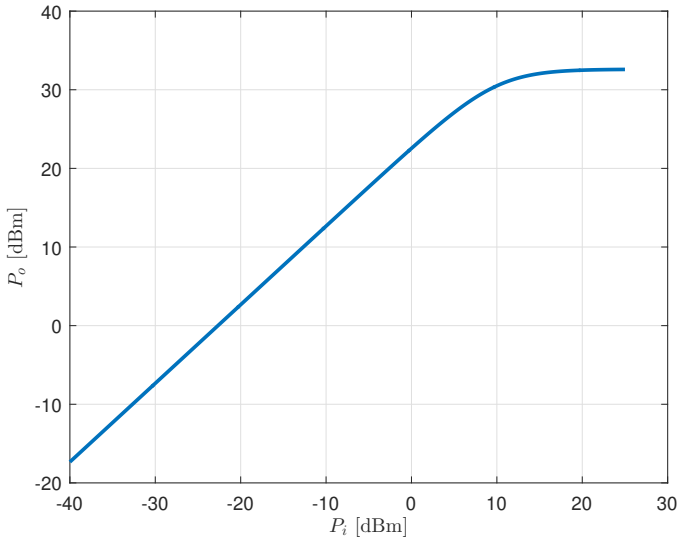

Figure 38: AM-AM distortion model based on D-band adopted parameters in [44]

Fig. 40 shows exemplary linearity measurements of a Solid State Power Amplifier (SSPA) in InGaAs technology by Fraunhofer IAF. The design and measurments of this device is reported in [45] The plot shows the transducer gain over the input power for different frequencies. Most of the frequencies reach a output related 1 dB compression point of 12 to 13 dBm. These linearity measurements are conducted by single tone measurements comparing the signal Power of a input tone with the signal power of the output tone. Measurements of the outputs phase are not yet included so a modelling according to the earlier described Rapp-Model can not yet be done.

4.4 I/Q Imbalance

The H-Band front end in TIMES has a super-heterodyne system architecture, which converts E-Band signal (60-90 GHz) to the H-band (220-320 GHz) using a commercially available E-band modem as a base for I/Q signals generation. In this section, we focus on modeling the I/Q imbalances from the E-band TX/RX LO chains. Ideally, the in-phase and quadrature paths are assumed to have the same gain and exactly 90^o phase

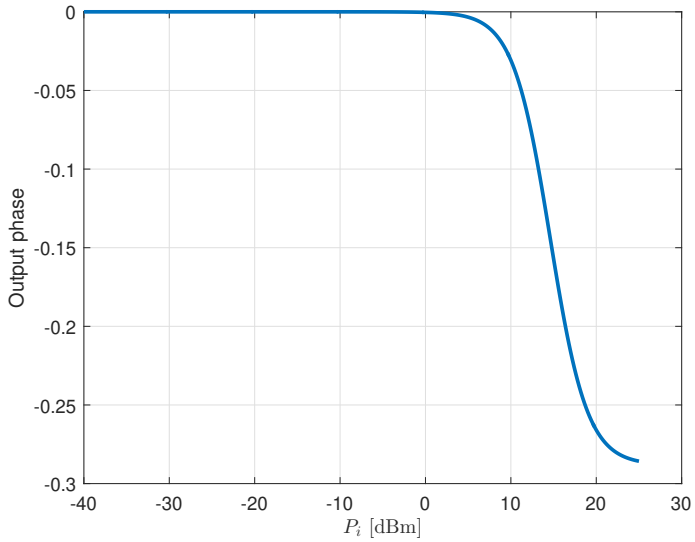

Figure 39: AM-PM distortion model based on D-band adopted parameters in [42]

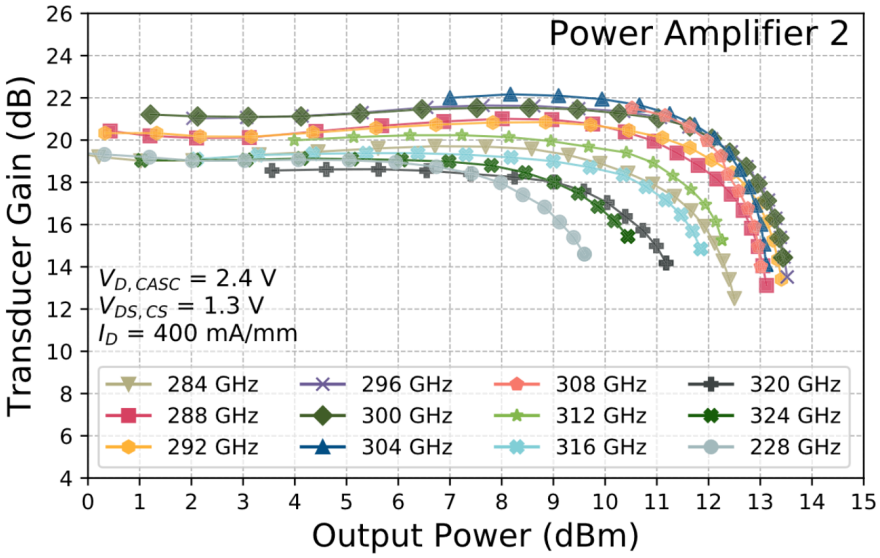

Figure 40: Linearity measurements (single tone) of a state of the art solid state power amplifier in InGaAs mHEMT technology by Fraunhofer IAF from [45].

shift, however, this is not the case in practice, and gain and phase imbalances are present, which degrades the systems performance after the signals up conversion (TX I/Q imbalance) and before down conversion at the receiver (RX I/Q imbalance). Moreover, due to the possibility of adopting very large bandwidths at the THz/sub-THz band, I/Q imbalance will be frequency dependent due to the mismatch between the low-pass filters at the in-phase and quadrature branches, the individual branch matching networks and integration parasitics. For instance, experiments have shown in [46] that while adopting a zero-IF architecture, frequency dependent I/Q mismatch was pronounced and increases the error vector magnitude if left untreated.

One other aspect to consider that could be prevalent in the THz/sub-THz regime is the timing mismatch between the in-phase and quadrature branches. Due to the very high sampling rates and Complementary Metal-Oxide Semiconductor (CMOS) process variations caused by e.g. the aging of the hardware components or

the device temperature, timing mismatches that are significant when compared to the sampling interval can degrade the system performance if not continuously tracked and compensated for at both the transmitter and the receiver [47].

To summarize, there are three aspects to consider at the sub-THz/THz bands when modeling I/Q imbalances:

- Gain and phase mismatches due to the non-ideal performance of the phase shift-er and signal paths.
- Frequency dependent I/Q imbalance due to the non-identical impulse responses of the low-pass filters at the in-phase and quadrature branches.
- Timing mismatches between the in-phase and quadrature paths due to the very high sampling rates at each of the branches.

In a laboratory example setup with the homodyne Elipse communication Link, using an Arbitrary Waveform Generator M8195A and an Realtime Scope Keysight DSO-Z 204A and coherent carrier generation, following IQ-Impairments have been observed for a 2 GHz broadband communication signal:

- Gain imbalance: -0.556 dB
- Phase imbalance: -4.842 degree

4.5 Local Oscillator Chain Harmonics

In this section, the limitations of transmit signal quality, arising from inter-modulation of unwanted harmonics caused by the electronic carrier generation based on frequency multiplication, in a superheterodyne 300 GHz transmit analog front end are analyzed. Using an electronic microwave frequency synthesizer in conjunction with cascaded frequency multipliers delivering an overall multiplication factor of 24, a 210 to 228 GHz carrier is generated. The fourth harmonic generated by the on-chip integrated frequency multiplier-by-three is measured to be present in the RF frequency domain with significant power levels, creating interferers for the modulated signals. An analysis of the spurious tone is performed as a function of the local oscillator power and frequency as well as IF input power to obtain signal-to-interferer power levels as the relevant frequencies lie within the transmitter RF frequency band of operation. For a more detailed description on how the measurement has been conducted and the operation states, please refer to [48]. All the information are based on experiments/measurements using the hardware from the ThoR-project.

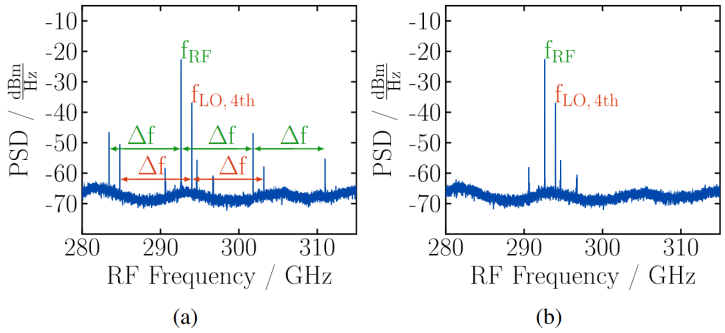

Figure 41: Measured RF spectra (a) without and (b) with waveguide bandpass filter inserted in the LO path. RF hardware from ThoR-Project was used. Operating conditions: f_{LO} = 73.5 GHz, f_{IF} = 72.125 GHz, P_{IF} = −18 dBm. (from [48]

As a conclusion, depending on the operating point, the power levels and the IF- and RF-frequency configuration, the spurious free dynamic range is varying between 11.2 dB and 24.3 dB, when the unwanted LO-harmonic are in-band. There are however also operating points, where no interferer is in-band. System

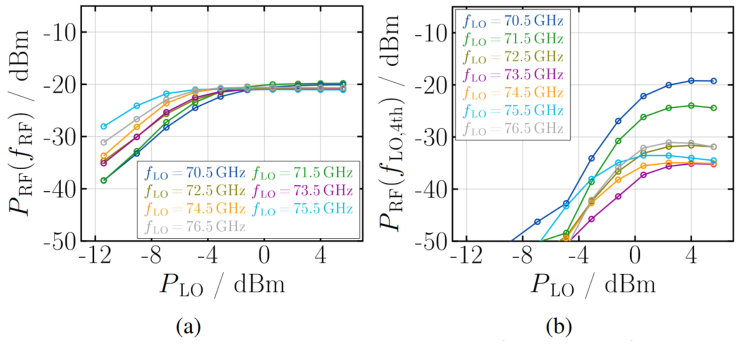

Figure 42: Measured RF power contributions of (a) f_{RF} and (b) $f_{LO,4th}$ as a function of LO input power for different LO frequencies over the LO tuning range of the TX module.

simulations, based on the measured data indicate, that the behaviour of these in-band tones can be modelled as additive interference.

4.6 Front-End Frequency Response

As already introduced, each component of the front end has a non-flat gain shape. So evidently the concatenated frequency responses add up to a more corrugated frequency response. This is highly depending on the operating points of the transmitter and receivers. A prediction of the channel-flatness of the transmitter and receiver hardware can hardly be conveyed because an individual characterization primarily of the frequency translating circuits is not precisely possible for every operating state. To quantify the channel response of the hardware for broadband modulated data, a communication experiment is conducted, which is shown in Fig. 43. An equalizer is used to maximize the signal quality. As a result the impulse response of the linear equalizer should converge towards the inverse of the impulse response of the channel. To eliminate additional effects and contributions, the measurement is done in a full coherent system, where IF-carrier, RF-carriers, signal generator and the sampling scope are linked by the same reference clock. Additionally no wireless channel is included, instead a wave-guide attenuator with a flat frequency response replaces the wireless channel.

In Fig. 44 the equalized frequency response of the broadband single carrier measurement is shown. Highlighting the gain shape of the complete TX-RX front end for a given operating point, bandwidth and carrier frequency. In this case the symbol rate is 4.5 GBd, the H-band carrier frequency is 302 GHz. As no channel is involved, the inverse of the equalizer frequency response can be used as a estimate/approximation for the gain shape of the front-ends.

4.7 Beam-Squinting

Due to the severe path-loss at the THz band, highly directive communications is envisioned to combat path loss. Directivity can be achieved through adopting a beamforming approach, and owing to the short wavelength at the THz band, in the case of adopting antenna arrays at the transmitter or receiver, arrays with large number of elements may be efficiently packed resulting in antennas with high gains implemented on devices with a small form factor. Moreover, due to the availability of very large bandwidths at the sub-THz/THz bands, e.g. as envisioned in IEEE 802.15.3d, a single chunk of around 69 GHz bandwidth can be utilized [49]. In this case, while carrying out beamforming, the conventional adjustments of the phases of each of the antenna elements will result in the beam-squinting phenomenon. Assuming uniform linear arrays (ULAs), a single RF chain and simple analog beamforming at the ULA, the channel response of the n^{th} antenna element can be shown to be $e^{-j2\pi n\frac{\sin(\theta)}{\lambda}}$, where θ is the angle of departure/angle of arrival and λ is the wavelength. The corresponding beamforming coefficient response is $e^{j2\pi n\frac{\sin(\phi)}{\lambda_{f_c}}}$, with λ_{f_c} is the wavelength at a specific frequency f_c and ϕ is the beamfocus angle [50]. Obviously, when $f \neq f_c$, gain and phase errors will occur. It can be shown that the array

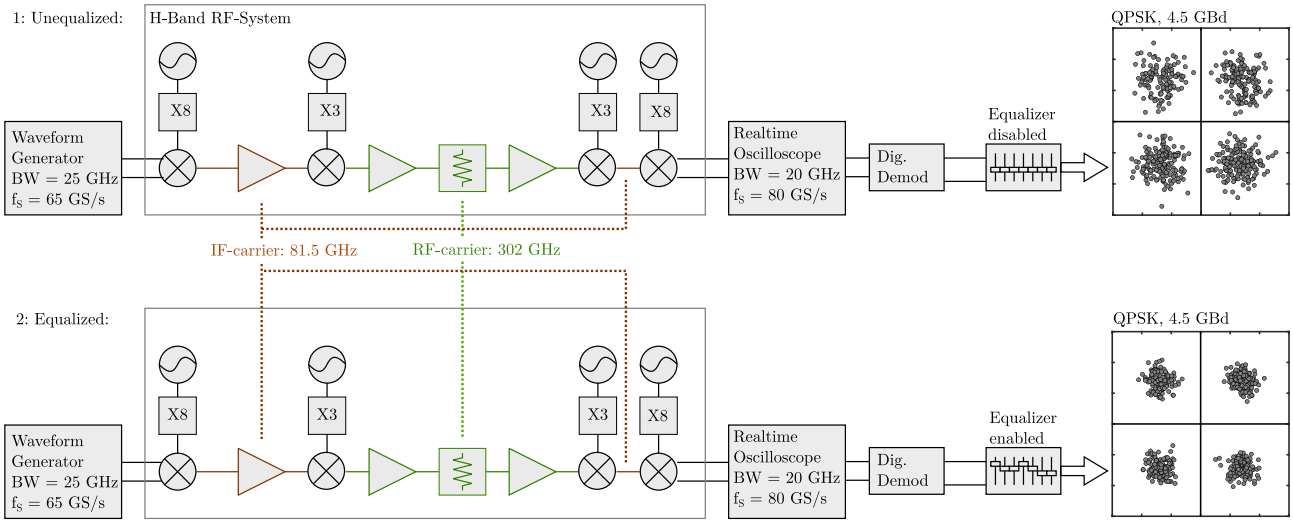

Figure 43: Measurement setup for extraction of the H-band front ends frequency response by applying broadband modulated signals and an equalization filter in the receiver.

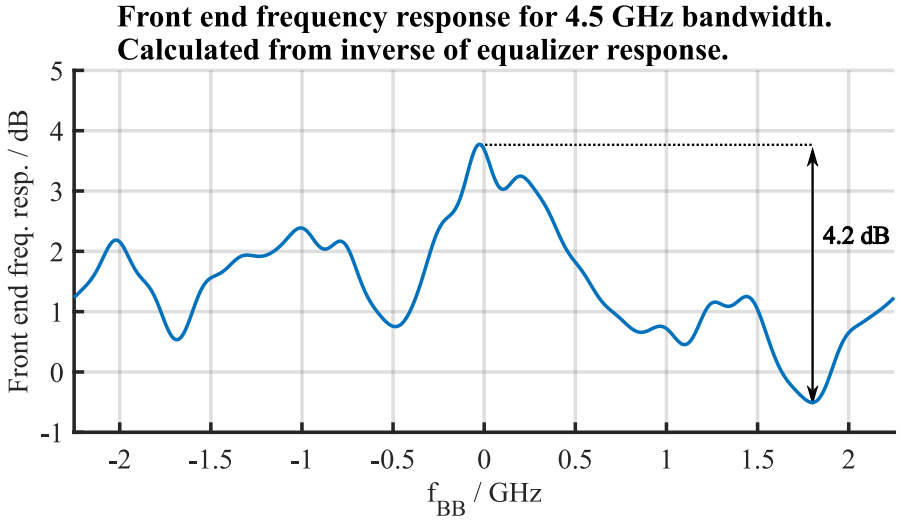

Figure 44: Measured front ends frequency response, based on inverse frequency response of equalization filter.

gain maybe written in the following form [50] (and references therein)

$$g\left(\frac{f}{f_c}\sin(\theta)-\sin(\phi)\right)=\frac{\sin(N0.5\pi(\frac{f}{f_c}\sin(\theta)-\sin(\phi)))}{\sqrt{N}\sin(0.5\pi(\frac{f}{f_c}\sin(\theta)-\sin(\phi)))}e^{j\frac{(N-1)\pi(\frac{f}{f_c}\sin(\theta)-\sin(\phi))}{2}}, \quad (89)$$

where N is the number of antenna elements at the ULA.

To show the effect of the number of antenna elements on beam-squinting, Fig. 45 shows the array gain as a function of the frequency of operation for different number of antenna elements N, where $N \in \{32, 256, 1024\}$. In this specific results, the bandwidth was fixed to 2.16 GHz as per channel IDs 1 to 32 in IEEE 802.15.3d [49], and $\theta = \phi = 50°$. It is clear that as N increases, the beam-squinting effect becomes more pronounced. For

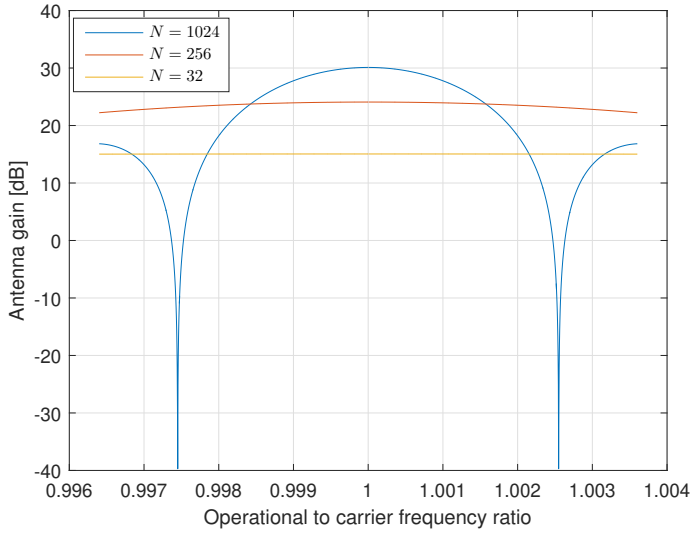

Figure 45: Comparison of different antenna gains with different number of ULA antenna elements. $f_c = 300$ GHz.

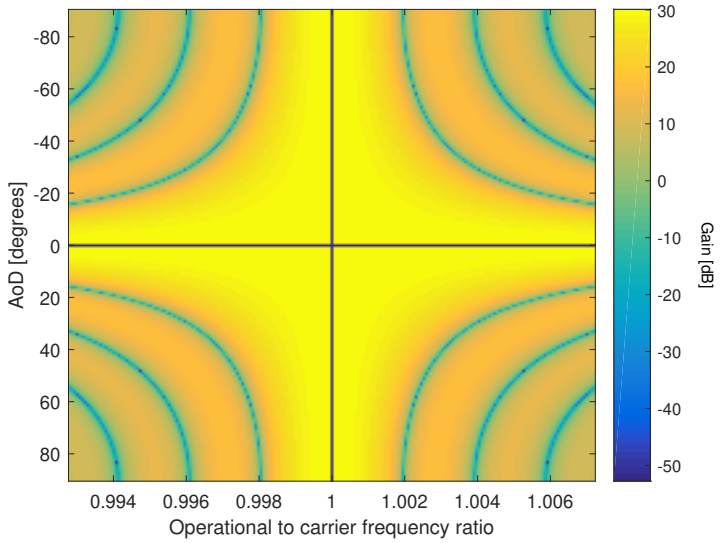

Figure 46: Comparison of different antenna gains with for different AoDs, $N = 1024$, $f_c = 300$ GHz.

instance, for $N = 32$, there is no apparent effect of beam-squinting on the antenna gain response, while for $N = 1024$, two gain dips are shown, which makes retrieving any data on the frequency support where such dips occur almost impossible if left untreated.

To highlight the effect that the AoD has on beam-squinting, Fig. 46 depicts a heatmap plot of the antenna gain as a function of the operational-to-carrier frequency ratio and AoD. In this specific setup, the bandwidth is 2×2.16 GHz, which corresponds to channel IDs 33 to 48 in the IEEE 802.15.3d standard [49], and $N = 1024$ elements. The figure shows that the antenna gain is dependent on the operating AoD, with an increased dependency of beam-squinting on the AoDs that are further away from 0 degrees and closer to $\pm\frac{\pi}{2}$.

A possible solution to mitigate the effect of beam-squinting is utilizing a TTD approach, where phase shifters are replaced with TTD lines [13]. When a TTD line is deployed, phase shifts can vary across the whole bandwidth with the cost of a higher design complexity and power consumption, thus rendering such solution to be less attractive especially for the case of very large number of antenna elements with corresponding phase shifters. Other approaches to mitigate the effect of beam squinting are presented in [13, 50–52], where different schemes and codebook designs for (hybrid) beamforming are investigated. These solutions lead to a communication system that is less affected by beam squinting, however, the spectral efficiency resulting from these approaches are less than methods that adopt TTD.

4.8 Analysis and Mitigation of Time-Frequency Synchronization Errors

In this section, we present a preliminary analysis that we carried out to quantify the impact of impairments in a OFDM communication system operating at THz frequencies. We mainly focus on the effects of time and frequency synchronization errors as these were shown to have significant impact on the performance of THz communications systems [53]. Such errors stem from the compound effect of hardware impairments and other physical phenomena. For example, frequency synchronization errors can originate from local oscillator phase noise, I/Q imbalances or Doppler effect caused by mobility of wireless terminals, etc. Similarly, the analog-to-digital conversion process can generate time synchronization errors due to slight variations of the sampling time, which is prevalent in scenarios with very large bandwidths.

To make our analysis as general as possible, we model errors in time and frequency as random variables with known distributions rather than describing their exact behavior. We evaluate their impact on the system performance by making use of the Error Vector Magnitude (EVM), a metric that is commonly used to assess the resilience of devices to errors. In particular, we compute the expected EVM as a function of errors' distributions and relate it with the achievable data rate. On the one hand, this approach represents a simple and convenient way to understand the impact of hardware impairments without the need of modeling all the non-idealities. On the other hand, it does not enable to distinguish the contributions of each individual non-ideality as their effect is jointly considered.

Moreover, we propose a novel scheme based on carrier aggregation and adaptive OFDM numerology to combat these errors and maximize the achievable data rate. Our solution selects the numerology configuration that minimizes the expected EVM and aggregates multiple carrier components in such a way to occupy all the available bandwidth while avoiding operations in highly-dispersive regions of the spectrum.

The work presented in this section was published in [54], we refer the reader to the original paper for additional details.

4.8.1 System Model

We model a received OFDM symbol impaired by Time Synchronization Error (TSE) and Carrier Frequency Offset (CFO). The rationale behind this modeling is to shed some light on the challenges faced when deploying OFDM receivers that are known for their sensitivity to time and frequency synchronization errors, which despite its widespread adoption in previous standards and the simplicity of its implementation, is often disregarded as a possible candidate to deployed at THz frequencies due to such synchronization limitations [55].

The transmitted OFDM symbol can be written as

$$s(t) = \frac{1}{N} \sum_{k=-N/2}^{N/2-1} X(k) e^{j\frac{2\pi k}{NT_s}(t-vT_s)}, \tag{90}$$

where $X(k)\ \forall\ k \in \{-N/2, \dots, N/2-1\}$ are drawn from a space of available data symbols modulated using M-Quadrature Amplitude Modulation (QAM), N is the Fast Fourier Transform (FFT) size, T_s is the sampling time at the transmitter and v is the Cyclic Prefix (CP) length.

The resulting symbol $s(t)$ then passes through a multi-path fading channel and faces frequency and time synchronization errors at the receiver. Hence, the time domain received signal after the removal of the CP can be written as [56]

$$\begin{aligned} r_n = \frac{1}{N} e^{j\frac{2\pi}{N}(v+n)(1+\eta)\varepsilon} \sum_{k=-N/2}^{N/2-1} X(k)H(k) \\ \times e^{j\frac{2\pi k}{N}n(1+\eta)} e^{j\frac{2\pi k}{N}v\eta} + w(n), \end{aligned} \tag{91}$$

where $n \in \{0, \dots, N-1\}$, $w(n)$ is the complex-valued Gaussian AWGN sample with zero mean and variance σ^2. $H(k) = \frac{1}{\sqrt{N}} \sum_{l=0}^{L-1} h_l e^{-j(2\pi k/N)l}$ is the channel response at the k^{th} sub-carrier, where $h_l\ \forall l \in \{0, \dots, L-1\}$ is the time domain l^{th} channel tap. Moreover, $\varepsilon = \Delta f N T_s$, where Δf is the CFO, and $\eta = \frac{\Delta T_s}{T_s}$, $\Delta T_s = T_s - T_s'$, where T_s' is the sampling time at the receiver.

Note that we model each multipath tap denoted by $|h_l|e^{j\phi_l}$, where $|h_l|$ follows a Nakagami-m distribution, and $\phi_l\ \forall l \in \{0, \dots, L-1\}$ follows a uniform distribution ranging from 0 to 2π [57]. The PDF of $|h_l|$ is defined as [58]

$$f_{|h_l|}(w) = \frac{2m_l^{m_l} w^{2m_l-1}}{\Gamma(m_l)\Omega_l^{m_l}} e^{-\frac{m_l w^2}{\Omega_l}}, \tag{92}$$

where $m_l = \frac{(\mathbb{E}\{w^2\})^2}{\mathrm{var}\{w^2\}}$, $m_l \geq \frac{1}{2}$, $\Omega_l = \mathbb{E}\{w^2\}$, and $\Gamma(.)$ is the Gamma function [59], Section 8.310, Eq. 1. Moreover, Ω_l can be calculated by adopting THz propagation loss model approximated in [60] and used by previous works on THz communications [61, 62].

We note that we choose a Nakagami-m distribution for the l^{th} channel tap to allow for a more flexible modeling of the statistical behavior of the tap's envelope when highly directive communications is applied, which is a common approach used when operating at the THz band to combat the propagation loss. For instance, in case of highly directive communications, a higher m factor is used, implying less fading, while a lower m factor implies the converse.

Lemma 1. *The random variable $|H(i)|\ \forall i \in \{0, \dots, N-1\}$ may be approximated as a Nakagami-m random variable with fading parameter $\tilde{m}$, where*

$$\tilde{m} = \frac{\left(\sum_{k=0}^{L-1} \Omega_k\right)^2}{\sum_{k=0}^{L-1} \left(\frac{\Omega_k^2}{m_k}\right) + \sum_{k=0}^{L-1} \sum_{l=0, l\neq k}^{L-1} \Omega_k \Omega_l} \tag{93}$$

and $\tilde{\Omega} = \mathbb{E}\{|H(i)|^2\} = \frac{1}{N} \sum_{k=0}^{L-1} \Omega_k$, and its PDF is given by

$$p_{|H(i)|}(x) = \frac{2}{\Gamma(\tilde{m})} \left(\frac{\tilde{m}}{\tilde{\Omega}}\right)^{\tilde{m}} x^{2\tilde{m}-1} \exp\left(-\frac{\tilde{m}}{\tilde{\Omega}} x^2\right). \tag{94}$$

Proof. See [63], page 25, and [64], Section II.B. □

To nullify any Inter-Symbol Interference (ISI), the CP length is chosen such that it is longer than the channel spread, L. The random residual time synchronization error is embedded in η that is modeled as a random variable. Moreover, ε includes the effect of the random residual CFO also modeled as a random variable. More on the statistical behavior of η and ε is discussed in Section III.A. Note that the performance of OFDM receivers subject to random residual synchronization errors was carried out in [65], where the authors have derived an analytical expression of the spectral efficiency metric for OFDM waveforms when random residual CFO of arbitrary distribution was considered. Such assumption is practical as receivers can never attain the Cramer-Rao lower bound of the estimator, as this would require an asymtotically large training sequence (see [65] and references therein).

Applying FFT to r_n, we get

$$Y(k) = \sum_{n=0}^{N-1} r_n e^{-j(2\pi/N)nk}, \tag{95}$$

and hence, we write

$$\begin{aligned} Y(k) = \frac{1}{N} \sum_{i=-N/2}^{N/2-1} \sum_{n=0}^{N-1} X(i)H(i) \\ \times \exp\left\{ j\frac{2\pi}{N} \left[v\left(\left(i\eta + (1+\eta)\,\varepsilon \right) \right) \right.\right. \\ \left.\left. + n\left(\left(i\eta + (1+\eta)\,\varepsilon \right) + i - k \right) \right] \right\} + W(k), \end{aligned} \tag{96}$$

where $W(k) = \sum_{i=0}^{N-1} w(i) e^{\frac{-j2\pi ik}{N}}$. Let $\eta = 0$ and $\varepsilon = 0$, i.e., time-frequency synchronization is ideal, $Y(k)$ reduces to

$$Y(k) = \frac{1}{N} \sum_{i=-N/2}^{N/2-1} X(i)H(i) \sum_{n=0}^{N-1} e^{j\frac{2\pi}{N} n(i-k)} + W(k),$$

and then

$$Y(k) = \begin{cases} X(k)H(k) + W(k), & \text{if } i = k \\ 0, & \text{otherwise.} \end{cases} \tag{97}$$

A vector representation of (96) is

$$\mathbf{y} = \mathbf{\Lambda H x} + \mathbf{w}, \tag{98}$$

where

$$\mathbf{\Lambda}_{k,i} = \frac{1}{N} \sum_{n=0}^{N-1} e^{j\frac{2\pi}{N}((i\eta+(1+\eta)\varepsilon)(n+v)+i-k)}, \tag{99}$$

$$\mathbf{H} = \text{diag}\left\{ H(-N/2+1), \ldots, H(N/2) \right\}, \tag{100}$$

$$\mathbf{x} = \left[x(-N/2+1), \ldots, x(N/2) \right]^T, \tag{101}$$

$$\mathbf{w} = \left[w(-N/2+1), \ldots, w(N/2) \right]^T. \tag{102}$$

A single-tap equalizer is deployed at the receiver to invert the channel's effect. The equalizer is defined by applying

$$\mathbf{P} = \text{diag}\left\{ \frac{H^*(-N/2)}{|H(-N/2)|^2}, \ldots, \frac{H^*(N/2-1)}{|H(N/2-1)|^2} \right\}. \tag{103}$$

Single-tap equalization is an attractive feature of OFDM due to its simplicity and effectiveness in reconstructing the data vector $\mathbf{x}$. Moreover, although $\mathbf{P}$ reveals that Inter-carrier Interference (ICI) is not accounted for in the equalization process, its simple realization makes it an efficient method to detect the transmitted symbol with the penalty of increasing the error floor brought by time (TSE) and frequency (CFO) synchronization errors.

4.8.2 Performance Analysis and Proposed Solution

In this section, we start by analyzing the performance of the OFDM waveform. The metric of choice in this work is the Component Carrier Data Rate (CCDR) which depends on the expected EVM that is probed after channel equalization. Note that the EVM assessment is carried out considering time-frequency synchronization errors in accordance with 3GPP specifications as detailed in [53, Annex F].

ADR Calculation As the simple structure of the equalizer $\mathbf{P}$ implies, CFO and TSE effects will not be compensated for, and thus the error floor is higher than the case where no synchronization errors are present, i.e., $\mathbf{\Lambda} = \mathbf{I}_N$. Hence, EVM probing is performed after the application of the equalizer resulting in $\hat{\mathbf{x}}$, where we write

$$\begin{aligned}\mathbf{e} &= \hat{\mathbf{x}} - \mathbf{x}, \\ &= (\mathbf{P\Lambda H} - \mathbf{I}_N)\,\mathbf{x} + \mathbf{Pw}.\end{aligned}$$

To quantify the severity of the error, we apply the following

$$\epsilon_i = \mathbb{E}_\eta \left\{ \mathbb{E}_{\varepsilon|\eta} \left\{ \mathbb{E}_{\mathbf{h}|\eta,\varepsilon} \left\{ |e_i|^2 \right\} \right\} \right\},$$

where

$$\begin{aligned}e_i = &\left(\delta_{ii} e^{\frac{j2\pi\nu}{N}(i\eta+(1+\eta)\varepsilon)} - 1 \right) x(i) + \frac{H^*(i)}{|H(i)|^2} \\ &\times \sum_{\substack{k=-N/2 \\ k\neq i}}^{N/2-1} \delta_{ik} e^{\frac{j2\pi\nu}{N}(i\eta+(1+\eta)\varepsilon)} X(k)H(k) + \frac{H^*(i)}{|H(i)|^2} w(i).\end{aligned} \tag{104}$$

The law of total expectation is applied in (104) assuming $\varepsilon \perp \eta \perp H(i)$, where $\perp$ denotes statistical independence, which is a practical assumption.

Moreover, using the linearity of the expectation operator and statistical independence between the data, the channel coefficients and the AWGN realizations, and dropping the subscripts of the expectation for tractability, we have

$$\begin{aligned}\mathbb{E}\left\{|e_i|^2\right\} = &\underbrace{\mathbb{E}\left\{ \left| \left(\delta_{i,i} e^{\frac{j2\pi\nu}{N}(i\eta+(1+\eta)\varepsilon)} - 1 \right) x(i) \right|^2 \right\}}_{\triangleq t_1} \\ &+ \underbrace{\mathbb{E}\left\{ \left| \frac{H^*(i)}{|H(i)|^2} \sum_{\substack{k=-N/2 \\ k\neq i}}^{N/2-1} \delta_{i,k} e^{\frac{j2\pi\nu}{N}(i\eta+(1+\eta)\varepsilon)} X(k)H(k) \right|^2 \right\}}_{\triangleq t_2} \\ &+ \underbrace{\mathbb{E}\left\{ \left| \frac{H^*(i)}{|H(i)|^2} w(i) \right|^2 \right\}}_{\triangleq t_3},\end{aligned} \tag{105}$$

where

$$\delta_{i,m} = \frac{1}{N}\sum_{n=0}^{N-1} e^{j\frac{2\pi}{N}n(m\eta+(1+\eta)\varepsilon+m-i)}. \tag{106}$$

Theorem 1. *Assuming that $\varepsilon \sim \mathcal{N}(0,\sigma_\varepsilon^2)$, $\eta \sim \mathcal{N}(0,\sigma_\eta^2)$, the expected EVM ($\epsilon$) may be approximately evaluated by applying (107).*

Proof. Please refer to [54, Appendix A]. □

$$\begin{aligned}\epsilon_i \approx \sigma_x^2\left(\frac{1}{N}+\frac{1}{N^2}\sum_{n=1}^{N-1}2(N-n)e^{-\frac{2\pi^2 n}{N^2}(\sigma_\eta^2+i^2\sigma_\varepsilon^2)}-2\sum_{n=0}^{N-1}\cos\left(\frac{2\pi^2}{N^2}(\nu+n)^2(i^2\sigma_\eta^2+\sigma_\varepsilon^2)\right)+1\right)\\ +\frac{\Gamma(\tilde{m}-1)\,\tilde{m}}{\Gamma(\tilde{m})\tilde{\Omega}}\tilde{\Omega}\sigma_x^2\sum_{\substack{k=-N/2\\k\neq i}}^{N/2-1}\sum_{n=0}^{N-1}\sum_{n'=0}^{N-1}e^{-\frac{2\pi^2}{N^2}(n-n')^2(\sigma_\eta^2+k^2\sigma_\varepsilon^2)}e^{j\frac{2\pi}{N}(k-i)(n-n')}+\frac{\Gamma(\tilde{m}-1)\,\tilde{m}}{\Gamma(\tilde{m})\tilde{\Omega}}\sigma_w^2.\end{aligned} \tag{107}$$

Although we note that **Theorem 1** provides the expected EVM result of specific statistical characteristics of the CFO and TSE, the methodology used to compute the expected EVM is still valid irrespective of the statistics of the errors of concern. As an example, in **Theorem 1** we assume ε and η normally distributed, and compute the expected EVM (ϵ_i) using the law of the unconscious statistician. Normally distributed synchronization errors is a reasonable assumption to adopt considering the deployment of a maximum likelihood estimator to estimate both quantities. Hence, this estimation process yields residual errors distributed normally with zero mean and variances proportional to the performance of the estimator, as explained in [65].

While the expected EVM (ϵ_i) calculated in (107) might not provide an insight into the instantaneous performance of the receiver, it reveals information on its expected performance. Hence, by solely knowing the statistical behavior of the channel, in this case $\tilde{m}$ and $\tilde{\Omega}$, and the variances of TSE and CFO, our approach can make a selection of a numerology that adapts to the receiver characteristics. Moreover, this strategy allows for a reduction of the control signaling overhead when selecting the numerology.

Next, we leverage the calculated expected EVM expression to derive the Aggregate Data Rate (ADR) as we present in the following theorem.

Theorem 2. *The ADR calculated using ϵ_i is approximately equal to*

$$\bar{R} \approx \frac{B}{N}\sum_{j=0}^{N_{f_c-1}}\sum_{i=-N/2}^{N/2-1}\log_2(\sigma_{x,j}^2+\epsilon_{i,j})-\log_2(\epsilon_{i,j}), \tag{108}$$

where N_{f_c} is the number of CCs.

Proof. Please refer to [54, Appendix B]. □

The next subsection provides the details behind the use of the results of **Theorem 1** and **Theorem 2** in the formulation of the solution to the ADR maximization scheme.

Proposed Solution The proposed solution is detailed in **Algorithm 1**, which takes as input $\mathbb{M}$ and $\mathbb{T}_s$, which denote the set of available FFT sizes N and the available sampling time values T_s, respectively, the channel statistics including the delay spread τ_d, $\mathbf{m}$, and $\mathbf{\Omega}$, which all depend on the carrier frequency of the Component Carrier (CC) in the available frequency spectrum and the statistics of the receiver performance, including variances of time and frequency synchronization errors σ_ε^2, σ_η^2, and the AWGN variance σ_w^2, the

Algorithm 1: ADR Maximization

Input: $\mathbb{M}$, $\mathbf{m}$, $\mathbf{\Omega}$, σ_{ε}^2, σ_{w}^2, σ_{η}^2, τ_d, $\mathbb{T}_s$, f_c, d, G, $\mathbb{T}_s$, $\bar{N}_{f_c}$

Output: $\mathbb{F}_o$

Calculate ΔB

for $ii \leftarrow 1$ **to** $length\{\mathbb{T}_s\}$ **by** 1 **do**

  $N_{f_c} \leftarrow \lfloor \frac{\Delta B}{\frac{1}{\mathbb{T}_s(ii)} + G(ii)} \rfloor$

  for $i \leftarrow 1$ **to** $\min\{\bar{N}_{f_c}, N_{f_c}\}$ **by** 1 **do**

    Determine $\mathbb{F}_{cc}(i)$

    $m \leftarrow \mathbf{m}(\mathbb{F}_{cc}(i))$

    $\Omega \leftarrow \mathbf{\Omega}(\mathbb{F}_{cc}(i))$

    $\mathbf{v}(i) \leftarrow \lceil \frac{\tau_d(\mathbb{F}_{cc}(i))}{\mathbb{T}_s(ii)} \rceil$

    for $iii \leftarrow 1$ **to** $length\{\mathbb{M}\}$ **by** 1 **do**

      if $\frac{\mathbf{v}(i)}{\mathbb{M}(iii)} \leq \gamma$ **then**

        $\mathbf{N}(i) \leftarrow \mathbb{M}(iii)$

      else

        $\mathbf{N}(i) \leftarrow \max\{\mathbb{M}\}$

      end

    end

    Solve $\mathbb{D}(\mathbb{F}_{cc}(i)) = \frac{[\mathbb{T}_s(i)]^{-1}}{N} \sum_{n=-N/2}^{N/2-1} \log_2\left(\sigma_x^2 + \epsilon_n\right) - \log_2\left(\epsilon_n\right)$

  end

  Compute $\mathbf{r}(ii) = \sum_{n=0}^{N_{f_c}-1} \mathbb{D}(\mathbb{F}_{cc}(n))$

end

Compute $\bar{R} = \max_{j \in \{1,\ldots,length(\mathbf{r})\}} \mathbf{r}(j)$

Extract $\mathbb{T}_s$, $\mathbf{N}$, $\mathbf{v}$, N_{f_c} and $\mathbb{F}_{cc}$ corresponding to $\bar{R}$

$\mathbb{F}_o \leftarrow \{\dot{\mathbb{T}}_s, \dot{\mathbf{N}}, \dot{\mathbf{v}}, \dot{N}_{f_c}, \dot{\mathbb{F}}_{cc}\}$

return $\mathbb{F}_o$

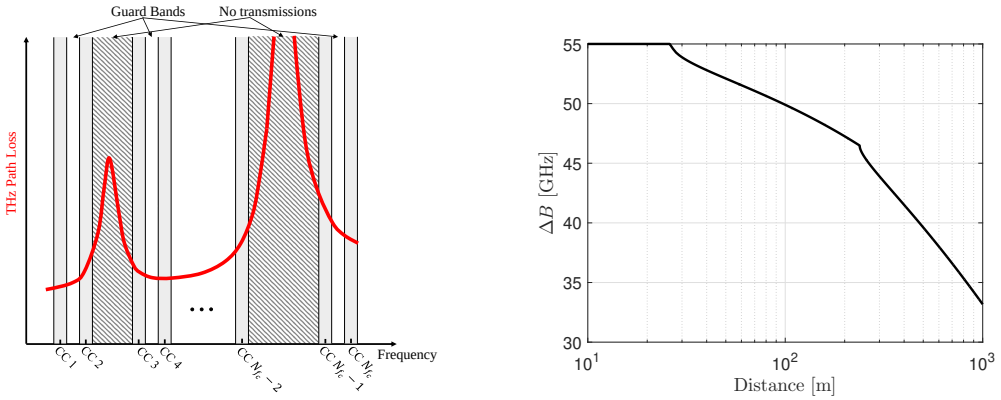

(a) *(b)*

Figure 47: Rough sketch of the proposed resource allocation scheme (left), available bandwidth as per the method in [60] (right).

separation distance (d) between the transmitter and the receiver, the guard-band bandwidth G which defines the separation between adjacent CCs in order to avoid interference, the carrier frequency f_c where the CCs are planned to be distributed, and the maximum number of CCs $\bar{N}_{f_c}$ that can be supported. Concerning the availability and utilization of channel statistics, as already done in [66], it is reasonable to assume the knowledge of the statistics of the channel to solve wireless communication problems. Regarding the separation distance d, the UE could determine its location through the assistance of the network, or, if necessary, such quantity could be extracted by adopting the procedure specified in 3GPP TS 38.305, namely the up-link/down-link AoA UE positioning procedure [67], and then extract the distance information from this estimate and use it as an input to **Algorithm 1**. It is worth noting that a proposal to consider communication devices that support different bandwidth configurations were the matter of discussion in the TS document [68]. From an implementation perspective, one of the methods discussed in [69] could be adopted at the transceiver to support the accommodation of variable sampling rate capabilities.

Using the defined inputs, **Algorithm 1** starts by calculating the available bandwidth ΔB as an initial step to distribute the CCs while being aware of the distance dependent molecular absorption loss peaks (as roughly sketched in Fig. 47a). Then, for each Component Carrier Bandwidth (CCB), the number of CCs is computed as per the calculation performed in line 3. In line 5, the individual CC center frequency $\mathbb{F}_{cc}(i)$ is determined. Subsequently, the channel statistics that are necessary for the calculation of the EVM are extracted depending on $\mathbb{F}_{cc}(i)$, and the CP length is calculated based on the delay spread identified at each $\mathbb{F}_{cc}(i)$. To regulate the overall OFDM symbol efficiency, the loop starting from line 10 adjusts the FFT size (N) for each CC while insuring that the ratio between the CP length at each CC ($\mathbf{v}(i)$) to the FFT size ($\mathbb{M}(iii)$) is less than γ, where γ is a threshold on the OFDM symbol efficiency. A necessary exit condition in line 13 is set to ensure that the scheme is not blocked by the condition in line 10, while noting that if this case is reached, efficiency is compromised. After selecting the appropriate FFT size, the CCDRs are calculated for each CC using the expected EVM result from **Theorem 1** for each CCB, and then returns a set $\mathbb{D}$ corresponding to the CCDRs at each CC. Through carrier aggregation, the CCDR is then used to calculate the ADR as indicated in line 18 for each CCB setup. In line 20, the maximum ADR is found, and the CCB, set of FFT sizes for each CC ($\dot{\mathbf{N}}$), set containing the CP length for each CC ($\dot{\mathbf{v}}$), the number of CCs and their locations ($\dot{N}_{f_c}$ and $\dot{\mathbb{F}}_{cc}$, respectively), and the best sampling time ($\dot{\mathbb{T}}_s$) corresponding to the maximum ADR are identified.

4.8.3 Numerical Examples

In this section, we present the results we obtained by means of numerical simulations, which demonstrate the performance of the proposed solution. We considered $N = 128$ and $v = 24$. Moreover, the delay spread was set to 5 ns based on the channel modeling results reported in [70], where the authors reported statistical

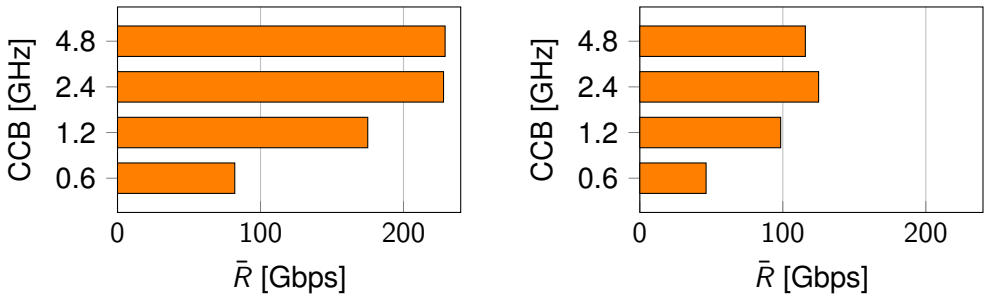

(a) Setup 1, selected CCB: 4.8 GHz. *(b) Setup 2, selected CCB: 2.4 GHz.*

Figure 48: Data rate for different CCB configurations, $d = 50$ m.

results of LoS THz channel's delay spread. Therefore, in our simulation setup, the channel model resembles an integrated access and backhaul use case [71]. Furthermore, the maximum bandwidth for a single CC was set to 4.8 GHz. $v = 24$ was kept constant for all bandwidths corresponding to the set $\mathbb{T}_s$, where the sampling time varies between 1/600 to 1/4800 μs. Based on the sampling frequency, the number of channel taps varies depending on the sampling time (higher sampling frequency results in a higher number of taps), while ensuring $\forall T_s,\ v \geq L$. For the highest sampling frequency, six active channel taps are simulated for a channel impulse response of length 24, each envelope of the taps is distributed according to the Nakagami-m distribution. For the first tap, we choose a higher m factor with $m_0 = 4$ therefore implying a dominance of a LoS component in order to model the dominant LoS component, while for the non-LoS taps we selected $m_l = 1\ \forall l\ \in \{1, \dots, L-1\}$, i.e., each tap's envelope is Rayleigh distributed. Regarding the parameter Ω, for the first tap, we modeled it based on THz path loss values extracted from the model detailed in [60], where we operate within standard atomespheric conditions in terms of pressure (101325 Pascales), a temperature of 296 Kelvins and a relative humidity of 50%. For the rest of the taps, we selected the power delay profile to be uniform with 6 dB higher propagation loss with respect to the LoS tap. We further assumed a transmitter antenna gain of 25 dBi and a receiver antenna gain of 15 dBi, typical values used in THz communication systems [72]. The transmission power is fixed throughout all the simulations and set to be 30 dBm. The guard-band interval between adjacent CCs was set to $1/T_s\ \forall T_s \in \mathbb{T}_s$. Such a large guard-band is selected to reduce any chances of interference between the to-be-aggregated carriers. Furthermore, following the 5G NR specifications, we set $N_{f_c} = 16$, as a practical transceiver could only use a limited number of CCs as specified in the 3GPP TS [73]. The AWGN variance σ_w^2 is calculated according to the kT/T_s, where k is Boltzmann's constant and T is the temperature. Although the approach in **Algorithm 1** implies a change of channel statistics per CC, we assume in this work the same channel statistics for each CC, except for $\boldsymbol{\Omega}$, where it is the most evident quantity to be affected as path loss changes per CC. Hence, one consequence of this assumption implies that the CP and FFT sizes are fixed for all CCs, thus resulting in a fixed subcarrier spacing. This fixed subcarrier spacing allows for the evaluation of per CCB setup to test the effects of TSE and CFO on the performance of the system.

In the proposed **Algorithm 1**, the calculation of the available bandwidth ΔB (line 1) and the CC frequency allocation, i.e. determining the vector $\mathbb{F}_{cc}$ (line 5), are performed in this work by implementing the following: The available bandwidth is calculated based on the method defined in [60], which yields an available bandwidth figure while operating in the frequency range between two molecular absorption loss peaks located at the frequencies $f_c^l = 325$ GHz and $f_c^h = 380$ GHz. Note that the proposed adaptive communication scheme is applicable regardless of the available bandwidth determination method. Hereafter, we merely state the details of the available bandwidth determination method proposed in [60]. The available bandwidth is calculated by applying

$$\Delta B = f_c^h - \Delta f_h - \left(f_c^l + \Delta f_l\right), \tag{109}$$

Distance (d)	CCB	N_{f_c}
50 m	0.6 GHz	16
50 m	1.2 GHz	16
50 m	2.4 GHz	10
50 m	4.8 GHz	5

Table 4: Aggregated number of CCs for different CCB configurations.

where

$$\Delta f_l = \frac{c}{100}\left[\left(\left[\left(\frac{100 f_c}{c} - 10.842\right)^2 + 0.0098\right]^{-1} + \frac{4.49\times 10^3 \pi \ln(\kappa)}{d\mu_{H_2O}}\right)^{-1} - 0.0098\right]^{0.5},$$
$$\Delta f_h = \frac{c}{100}\left[\left(\left[\left(\frac{100 f_c}{c} - 12.679\right)^2 + 0.0107\right]^{-1} + \frac{4.7\times 10^2 \pi \ln(\kappa)}{d\mu_{H_2O}}\right)^{-1} - 0.0107\right]^{0.5},$$

f_c is the overall carrier frequency where the CCs will operate, c is the speed of light in meters per seconds, κ is the tolerance of the deviation of absorption loss, μ_{H_2O} is the volume mixing ratio of water vapor, which is given by

$$\mu_{H_2O} = \frac{\phi}{100}\frac{p_w^*(T,p)}{p}, \tag{110}$$

ϕ is the relative humidity, $\phi p_w^*(T,p)/100$ represents the partial pressure of water vapor, where the saturated water vapor partial pressure p_w^* under pressure p and temperature T can be estimated by applying

$$p_w^* = 6.1121\left(1.0007 + 3.46\times 10^{-6} p\right)\exp\left(\frac{17.502\,T}{240.97 + T}\right). \tag{111}$$

In this example, the frequency allocation scheme is implemented by replacing line 5 with the following

$$\mathbb{F}_{cc}(i) = f_l^h + \Delta f_l + \frac{[\mathbb{T}_s(ii)]^{-1}}{2} + (i-1)\times(G(ii) + \mathbb{T}_s(ii)),$$
$$\forall i \in \{1,\dots,\min\{\bar{N}_{f_c}, N_{f_c}\}\}, \forall ii \in \{1,\dots,\text{length}(\mathbb{T}_s)\}.$$

In Fig. 47b, we depict the available bandwidth vs. the separation distance between the transmitter and the receiver by applying Eq. (109) with $\kappa = 0.1$dB. Note that this approach that is highlighting the interdependence between the distance and the usable bandwidth at THz frequencies was adopted in other works, such as [62].

In our evaluations, we considered two error model setups, namely *setup 1*, with $\Delta f = 1$ kHz and $\Delta T_s = 1\times 10^{-18}$ s, which represents a high-end device with relatively good time-frequency synchronization capabilities, and *setup 2*, with $\Delta f = 20$ kHz and $\Delta T_s = 2\times 10^{-16}$ s, which represents a low-end device with worse time-frequency synchronization capabilities.

Fig. 48a depicts the data rates for each possible CCB configuration, with $d = 50$ m and *setup 1*. In this specific setup, our proposed solution selects the bandwidth of CCB configuration corresponding to a bandwidth of 4.8 GHz per CC, as it yields the highest ADR of around 222 Gbps out of all possible configurations.

For *setup 2*, where the CFO and TSE are both higher, lower data rates are observed, as depicted in Fig. 48b. In this case, the optimal configuration corresponds to a CCB of 2.4 GHz per CC, yielding an ADR of around 123 Gbps.

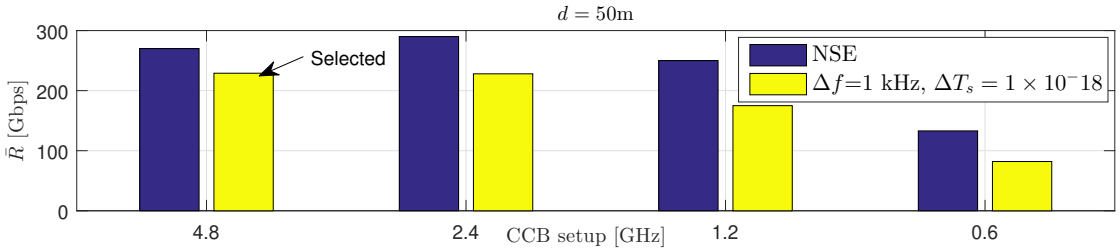

Figure 49: ADR vs. different CCB setups.

We note that for all error model setups, adopting a bandwidth of 0.6 GHz per CC always yields relatively lower ADR. This is due to the fact that in our evaluation we limited the maximum number of CCs that can be activated to N_{f_c}=16. Therefore, even aggregating the maximum number of CCs will not result in the exploitation of the total available bandwidth to get a higher ADR. To highlight this behaviour, Table II presents the selected number of CCs for different distances and different bandwidth configurations. It can be noticed that increasing the CCB generally reduces the number of aggregated CCs, as the available bandwidth is limited. This is however not observed when the CCB is relatively low, where the proposed approach chooses to exploit all available CCs to increase the ADR.

Fig. 49 depicts the ADR for each CCB setup and fixed error parameters, namely *setup* 1. Moreover, each ADR is compared to the case where no TSE and CFO are present in the system to highlight the maximum possible achievable rate if synchronization errors were not present. This scheme is named No Synchronization Error (NSE). As expected, NSE always yields the maximum achievable ADR. The configuration corresponding to CCB=4.8 GHz with $N_{f_c} = 5$ CCs is selected, as it achieves the highest ADR.

5 Conclusions

In this deliverable, we presented intermediate findings on physical layer procedures for enabling highly efficient and reliable THz links supporting sensing and communication functionalities, and discussed estimation mechanisms to predict the evolution of THz channels.

In Section 2, we studied how near field propagation phenomena can be leveraged to improve the beamforming and multiplexing gains by means of proper PHY layer processing. We analyzed the achievable performance in terms of throughput and spectral efficiency, considering different scenarios and system configurations. Based on our results, we showed that spatial multiplexing is necessary to achieve the data rate requirements envisioned by the project. We motivated the need for replacing traditional beamforming solutions (i.e., based on the assumption of planar wavefronts) with novel beamfocusing schemes able to exploit the curvature of the wavefronts over the array aperture. Moreover, we introduced fully-digital and hybrid beamforming architectures, investigated State-of-the-Art solutions for estimating the evolution of THz channels, and motivated the adoption of an hybrid approach. Finally, we discussed a low-complexity approach to perform beam steering using frequency-scanning antennas.

In Section 3, we introduced a novel PHY-layer waveform tailored for THz ISAC systems. We evaluated the performance of the proposed solution in both communication and sensing domains. Preliminary results reveal that our design outperforms common baselines and is flexible enough to accommodate the requirements in both domains. Furthermore, we proposed a new approach for the tracking of moving targets that is suitable for operating in the near-field, which can be exploited to improve safety and to predict the evolution of wireless links.

In Section 4, we introduced the transceiver architecture adopted in this project and identified potential impairments that may influence its behavior. We described each contributing impairment and quantified their effect by means of measurements on preliminary RF hardware components. We analyzed the impact of these impairments on the performance of an OFDM system operating at THz frequencies and proposed possible mitigation techniques.

As part of future work, we will continue the design and evaluation of physical layer procedures for enabling efficient and reliable THz links supporting sensing and communication functionalities, and the development of channel estimation schemes. In particular, we will enrich our analysis considering technical inputs from other WPs. We will make use of more accurate channel models that will be provided by WP 3 and use them to evaluate the performance of the proposed designs in the scenarios targeted by the project. We will carry out additional measurement campaigns to assess the impact of hardware impairments on the final transceiver designs that will be provided by WP 5. We will define more precise impairments models and use them to evaluate the behavior of the proposed solutions when subject to realistic operating conditions. Based on this analysis, we will develop more advanced schemes able to mitigate the effect of hardware imperfections. The final outcomes of this activity will be presented in a report that will be completed in month 24.

References

[1] David Tse and Pramod Viswanath. *Fundamentals of wireless communication*. Cambridge university press, 2005.

[2] Giacomo Bacci, Luca Sanguinetti, and Emil Björnson. Spherical wavefronts improve MU-MIMO spectral efficiency when using electrically large arrays. *IEEE Wireless Communications Letters*, 2023.

[3] Heedong Do, Namyoon Lee, and Angel Lozano. Parabolic wavefront model for line-of-sight mimo channels. *IEEE Transactions on Wireless Communications*, 2023.

[4] Constantine A Balanis. *Antenna theory: analysis and design*. Wiley-Interscience, 2005.

[5] Emil Björnson and Luca Sanguinetti. Power scaling laws and near-field behaviors of massive mimo and intelligent reflecting surfaces. *IEEE Open Journal of the Communications Society*, 1:1306–1324, 2020.

[6] TIMES. Deliverable 3.1 - state-of-art channel models in industrial environments at sub-thz frequencies. Technical report, TIMES, 2023.

[7] TIMES. Deliverable 2.2 - definition of scenarios for software simulation. Technical report, TIMES, 2023.

[8] Hua Wang, Fei Wang, Huy Thong Nguyen, Sensen Li, Tzu-Yuan Huang, Amr S Ahmed, Michael Edward Duffy Smith, Naga Sasikanth Mannem, and Jeongseok Lee. Power amplifiers performance survey 2000-present. *PA_survey. html*, 2020.

[9] Parisa Ramezani and Emil Björnson. Near-field beamforming and multiplexing using extremely large aperture arrays. *arXiv preprint arXiv:2209.03082*, 2022.

[10] Sebastian Priebe and Thomas Kurner. Stochastic modeling of thz indoor radio channels. *IEEE Transactions on Wireless Communications*, 12(9):4445–4455, 2013.

[11] Yuanwei Liu, Zhaolin Wang, Jiaqi Xu, Chongjun Ouyang, Xidong Mu, and Robert Schober. Near-field communications: A tutorial review. *arXiv preprint arXiv:2305.17751*, 2023.

[12] Foad Sohrabi and Wei Yu. Hybrid digital and analog beamforming design for large-scale antenna arrays. *IEEE Journal of Selected Topics in Signal Processing*, 10(3):501–513, 2016.

[13] Feifei Gao, Bolei Wang, Chengwen Xing, Jianping An, and Geoffrey Ye Li. Wideband Beamforming for Hybrid Massive MIMO Terahertz Communications. *IEEE Journal on Selected Areas in Communications*, 39(6):1725–1740, 2021.

[14] Mingyao Cui and Linglong Dai. Channel estimation for extremely large-scale MIMO: Far-field or near-field? *IEEE Transactions on Communications*, 70(4):2663–2677, 2022.

[15] Enoc Roselló Castillo, Parisa Harati, Ingmar Kallfass, Philipp Hügler, Christian Waldschmidt, and Shoichi Shiba. Spatial-frequency-scanning data transmission for mmw multi-user wireless communication systems. In *2017 47th European Microwave Conference (EuMC)*, pages 220–223, 2017.

[16] Kamal Sarabandi, Armin Jam, Mehrnoosh Vahidpour, and Jack East. A novel frequency beam-steering antenna array for submillimeter-wave applications. *IEEE Transactions on Terahertz Science and Technology*, 8(6):654–665, 2018.

[17] Thomas Kürner, Keitarou Kondou, and Fumihiro Nishiyama. IEEE 802.15-21-0131-02-03ma-proposal_rifs_extension, March 2022.

[18] Thomas Kürner. IEEE 802.15-22-0353-00-0thz-inter-carrier interference for IEEE 802.15.3d multiband transmission, July 2022.

[19] Emil Björnson, Jakob Hoydis, Luca Sanguinetti, et al. Massive mimo networks: Spectral, energy, and hardware efficiency. *Foundations and Trends® in Signal Processing*, 11(3-4):154–655, 2017.

[20] Ian F Akyildiz, Chong Han, Zhifeng Hu, Shuai Nie, and Josep Miquel Jornet. Terahertz band communication: An old problem revisited and research directions for the next decade. *IEEE Transactions on Communications*, 70(6):4250–4285, 2022.

[21] Theodore S Rappaport, Robert W Heath Jr, Robert C Daniels, and James N Murdock. *Millimeter wave wireless communications*. Pearson Education, 2015.

[22] Robert W Heath, Nuria Gonzalez-Prelcic, Sundeep Rangan, Wonil Roh, and Akbar M Sayeed. An overview of signal processing techniques for millimeter wave mimo systems. *IEEE journal of selected topics in signal processing*, 10(3):436–453, 2016.

[23] Ming Xiao, Shahid Mumtaz, Yongming Huang, Linglong Dai, Yonghui Li, Michail Matthaiou, George K Karagiannidis, Emil Björnson, Kai Yang, I Chih-Lin, et al. Millimeter wave communications for future mobile networks. *IEEE Journal on Selected Areas in Communications*, 35(9):1909–1935, 2017.

[24] Ahmed Alkhateeb, Omar El Ayach, Geert Leus, and Robert W Heath. Hybrid precoding for millimeter wave cellular systems with partial channel knowledge. In *2013 Information Theory and Applications Workshop (ITA)*, pages 1–5. IEEE, 2013.

[25] Jianhua Mo and Robert W Heath. High snr capacity of millimeter wave mimo systems with one-bit quantization. In *2014 Information Theory and Applications Workshop (ITA)*, pages 1–5. IEEE, 2014.

[26] Martin Braun, Christian Sturm, and Friedrich K. Jondral. On the single-target accuracy of ofdm radar algorithms. In *2011 IEEE 22nd International Symposium on Personal, Indoor and Mobile Radio Communications*, pages 794–798, 2011.

[27] S. Lee, H. Kim, Y. Park, H. Lee, and J. Lee. Downlink OFDMA with DFT-precoding for tera-hertz communications. In *Proc. of IEEE Global Communications Conference (GLOBECOM)*, 2020.

[28] Lu Chen, Jianxiong Pan, Jing Zhang, Junfeng Cheng, Luyan Xu, and Neng Ye. FDSS-based DFT-s-OFDM for 6G wireless sensing. *Sensors*, 23(3), 2023.

[29] Alphan Şahin, Nozhan Hosseini, Hosseinali Jamal, Safi Shams Muhtasimul Hoque, and David W. Matolak. DFT-spread-OFDM-based chirp transmission. *IEEE Communications Letters*, 25(3):902–906, 2021.

[30] C. Han et al. Multi-ray channel modeling and wideband characterization for wireless communications in the terahertz band. *IEEE Transactions on Wireless Communications*, 14(5):2402–2412, May 2015.

[31] Mark A Richards. *Fundamentals of radar signal processing*. McGraw-Hill Education, 2014.

[32] Kevin Gilholm and David Salmond. Spatial distribution model for tracking extended objects. *IEE Proceedings - Radar, Sonar and Navigation*, 152:364–371(7), 2005.

[33] Saeid K. Dehkordi, Lorenzo Pucci, Peter Jung, Andrea Giorgetti, Enrico Paolini, and Giuseppe Caire. Multi-static parameter estimation in the near/far field beam space for integrated sensing and communication applications, 2023.

[34] Won Namgoong and Payam Rabiei. CRLB-Achieving I/Q Mismatch Estimator for Low-IF Receiver Using Repetitive Training Sequence in the Presence of CFO. *IEEE Transactions on Communications*, 60(3):706–713, 2012.

[35] Parisa Harati, Benjamin Schoch, Axel Tessmann, Dirk Schwantuschke, Ralf Henneberger, Harald Czekala, Thomas Zwick, and Ingmar Kallfass. Is e-band satellite communication viable?: Advances in modern solid-state technology open up the next frequency band for satcom. *IEEE Microwave Magazine*, 18(7):64–76, 2017.

[36] Benjamin Schoch, Dominik Wrana, Laura Manoliu, Michael Kuri, Sandrine Wagner, Axel Tessmann, and Ingmar Kallfass. E-band active upconverter module with tunable lo feedthrough. In *2023 IEEE Radio and Wireless Symposium (RWS)*, pages 80–83, 2023.

[37] Iulia Dan, Christopher Grötsch, Laurenz John, Sandrine Wagner, Axel Tessmann, and Ingmar Kallfass. A superheterodyne 300ghz transmit receive chipset for beyond 5g network integration. In *2021 16th European Microwave Integrated Circuits Conference (EuMIC)*, pages 117–120, 2022.

[38] G. Ducournau and P. Szriftgiser. Deliverable d4.1 - photonic lo performance report. ThoR Deliverable D4.1, University of Lille, november 2019.

[39] DRO10500A data sheet.

[40] Open6GHub Signal Source v2 data sheet (internal).

[41] W. Bosch and G. Gatti. Measurement and simulation of memory effects in predistortion linearizers. *IEEE Transactions on Microwave Theory and Techniques*, 37(12):1885–1890, 1989.

[42] Nokia. Realistic power amplifier model for the New Radio evaluation. *3rd Generation Partnership Project (3GPP)*, R4-163314(TSG-RAN WG4 Meeting Number 79), 2016.

[43] Christoph Rapp. Effects of hpa-nonlinearity on a 4-dpsk/ofdm-signal for a digital sound broadcasting signal. *ESA Special Publication*, 332:179–184, 1991.

[44] Alexander Maltsev, Alexander Shikov, Andrey Pudeev, Seonwook Kim, and Suckchel Yang. A method for power amplifier distortions compensation at the rx side for the 5g nr communication systems. *Proceedings of CECNet*, 363:119–129, 2022.

[45] Laurenz John, Axel Tessmann, Arnulf Leuther, Philipp Neininger, Thomas Merkle, and Thomas Zwick. Broadband 300-ghz power amplifier mmics in ingaas mhemt technology. *IEEE Transactions on Terahertz Science and Technology*, 10(3):309–320, 2020.

[46] I Kallfass, SM Dilek, and I Dan. Signal quality impairments by analog frontend non-idealities in a 300 GHz wireless link. In *2017 11th European Conference on Antennas and Propagation (EUCAP)*, pages 1618–1621. IEEE, 2017.

[47] Wei-Chi Lai, Yuan-Te Liao, and Terng-Yin Hsu. A cost-effective preamble-assisted engine with skew calibrator for frequency-dependent i/q imbalance in 4x4 mimo-ofdm modem. *IEEE Transactions on Circuits and Systems I: Regular Papers*, 60(8):2199–2212, 2013.

[48] Dominik Wrana, Simon Haussmann, Benjamin Schoch, Laurenz John, Axel Tessmann, and Ingmar Kallfass. Effects of harmonics from frequency-multiplicative carrier generation in a superheterodyne 300 ghz transmit frontend. In *2023 53rd European Microwave Conference (EuMC)*, pages 138–141, 2023.

[49] Vitaly Petrov, Thomas Kurner, and Iwao Hosako. IEEE 802.15. 3d: First standardization efforts for subterahertz band communications toward 6G. *IEEE Communications Magazine*, 58(11):28–33, 2020.

[50] Ignas Laurinavicius, Huiling Zhu, Jiangzhou Wang, and Yijin Pan. Beam Squint Exploitation for Linear Phased Arrays in a mmWave Multi-Carrier System. In *2019 IEEE Global Communications Conference (GLOBECOM)*, pages 1–6, 2019.

[51] Mengyuan Ma, Nhan Thanh Nguyen, and Markku Juntti. Beam squint analysis and mitigation via hybrid beamforming design in thz communications. In *ICC 2023 - IEEE International Conference on Communications*, pages 6486–6491, 2023.

[52] Mingming Cai, J. Nicholas Laneman, and Bertrand Hochwald. Beamforming codebook compensation for beam squint with channel capacity constraint. In *2017 IEEE International Symposium on Information Theory (ISIT)*, pages 76–80, 2017.

[53] 3GPP. Ts 38.101-1, nr; user equipment (ue) radio transmission and reception; part 1: Range 1 standalone, v16.4.0. Technical report, 3GPP, 2022.

[54] Lutfi Samara, Tommaso Zugno, Mate Boban, Malte Schellmann, and Thomas Kürner. Adapt and aggregate: Adaptive ofdm numerology and carrier aggregation for high data rate terahertz communications. *IEEE Journal of Selected Topics in Signal Processing*, 17(4):794–805, 2023.

[55] Chong Han and Ian F Akyildiz. Distance-aware bandwidth-adaptive resource allocation for wireless systems in the terahertz band. *IEEE Transactions on Terahertz Science and Technology*, 6(4):541–553, 2016.

[56] Hung Nguyen-Le, Tho Le-Ngoc, and Chi Chung Ko. Rls-based joint estimation and tracking of channel response, sampling, and carrier frequency offsets for ofdm. *IEEE Transactions on Broadcasting*, 55(1):84–94, 2009.

[57] Zheng Du, Julian Cheng, and Norman C Beaulieu. Accurate error-rate performance analysis of ofdm on frequency-selective nakagami-m fading channels. *IEEE Transactions on Communications*, 54(2):319–328, 2006.

[58] Michel Daoud Yacoub, JE Vargas Bautista, and L Guerra de Rezende Guedes. On higher order statistics of the nakagami-m distribution. *IEEE Transactions on Vehicular Technology*, 48(3):790–794, 1999.

[59] Izrail Solomonovich Gradshteyn and Iosif Moiseevich Ryzhik. *Table of integrals, series, and products*. Academic press, 2014.

[60] Joonas Kokkoniemi, Janne Lehtomäki, and Markku Juntti. Simplified molecular absorption loss model for 275–400 gigahertz frequency band. In *12th European Conference on Antennas and Propagation (EuCAP 2018)*, pages 1–5. IET, 2018.

[61] Alexandros-Apostolos A Boulogeorgos, Evangelos N Papasotiriou, and Angeliki Alexiou. Analytical performance assessment of thz wireless systems. *IEEE Access*, 7:11436–11453, 2019.

[62] Alexandros-Apostolos A Boulogeorgos, Evangelos N Papasotiriou, and Angeliki Alexiou. A distance and bandwidth dependent adaptive modulation scheme for thz communications. In *2018 IEEE 19th International Workshop on Signal Processing Advances in Wireless Communications (SPAWC)*, pages 1–5. IEEE, 2018.

[63] Minoru Nakagami. The m-distribution-a general formula of intensity distribution of rapid fading. In *Statistical methods in radio wave propagation*, pages 3–36. Elsevier, 1960.

[64] Zhengjiu Kang, Kung Yao, and Flavio Lorenzelli. Nakagami-m fading modeling in the frequency domain for ofdm system analysis. *IEEE communications Letters*, 7(10):484–486, 2003.

[65] Ahmed Almradi and Khairi Ashour Hamdi. Spectral efficiency of ofdm systems with random residual cfo. *IEEE Transactions on Communications*, 63(7):2580–2590, 2015.

[66] Luis Blanco and Montse Nájar. Sparse multiple relay selection for network beamforming with individual power constraints using semidefinite relaxation. *IEEE Transactions on Wireless Communications*, 15(2):1206–1217, 2015.

[67] 3GPP. NG Radio Access Network (NG-RAN); Stage 2 Functional Specification of User Equipment (UE) Positioning in NG-RAN, 2020.

[68] Evolved Universal Terrestrial Radio Access. User equipment (ue) radio access capabilities. *Standard ETSI TS*, 136(306):V14, 2015.

[69] A Tkacenko. Variable sample rate conversion techniques for the advanced receiver. *Interplanetary Network (IPN) Progress Report*, 42:168, 2007.

[70] Naveed A Abbasi, Jorge Gomez-Ponce, Revanth Kondaveti, Shahid M Shaikbepari, Shreyas Rao, Shadi Abu-Surra, Gary Xu, Charlie Zhang, and Andreas F Molisch. Thz band channel measurements and statistical modeling for urban d2d environments. *IEEE Transactions on Wireless Communications*, 2022.

[71] Charitha Madapatha, Behrooz Makki, Chao Fang, Oumer Teyeb, Erik Dahlman, Mohamed-Slim Alouini, and Tommy Svensson. On integrated access and backhaul networks: Current status and potentials. *IEEE Open Journal of the Communications Society*, 1:1374–1389, 2020.

[72] Thomas Kürner. Towards future thz communications systems. *Terahertz science and technology*, 5(1):11–17, 2012.

[73] 3GPP. Ts 38.133, nr; requirements for support of radio resource management, v17.7.0. Technical report, 3GPP, 2022.